博士論文

Numerical and analytical study of wind turbine wakes considering ambient environment and operational conditions

（周辺環境と運転条件を考慮した風車後流の数値予測と解析モデルの提案）

钱 国伟

Numerical and analytical study of wind turbine wakes considering ambient environment and operational conditions

（周辺環境と運転条件を考慮した風車後流の数値予測と解析モデルの提案）

钱 国伟

Guo-Wei QIAN

Department of Civil Engineering

The University of Tokyo

A Dissertation Submitted to the University of Tokyo

in Partial Fulfillment of the Requirements for the Degree of

Doctor of Philosophy

2018.8.20

DECLARATION

This is to certify that the work presented in this thesis has been carried out at the University of Tokyo and has not been previously submitted to any other university or technical institution for a degree or award. The thesis comprises only my original work, except where the due acknowledgement is made in the text.

Guo-Wei QIAN

ABSTRACT

Wind turbines in a wind farm operating in the downwind wake flow are subjected to two main problems: decreased energy production due to the velocity deficit and increased fatigue loading due to the added turbulence intensity generated by the upwind turbine. In addition, the different ambient environment and turbine operation conditions make the wind farm aerodynamics quite complicated. Therefore, an accurate and efficient evaluation of the wake effect is essential in the wind farm layout design and maintenance in order to improve the power efficiency and the lifetime of the turbine. This research focus on numerical study and analytical study of wind turbine wakes considering the ambient environment and turbine operational conditions. Wind turbine wakes under various conditions are simulated at first to investigate the behavior of wake flow and its interaction with atmospheric boundary layer. Then a new analytical wake model with high accuracy and efficiency is proposed based on the numerical study and theoretical analysis. Finally, application of the developed numerical and analytical model in real wind farm over the complex terrain are examined and validated.

In Chapter 1, the general background of this study, review of previous researches, objectives and outline of this thesis are presented.

In Chapter 2, the mathematical model utilized in this thesis for the numerical study of wind turbine wakes are illustrated. The fundamental concepts and governing equations for the Computational Fluid Dynamics (CFD) with Reynolds Stress Model (RSM), the Large Eddy Simulation (LES) and Delayed Detached Eddy Simulation (DDES) are firstly introduced. The Actuator Disk Model with Rotation (ADM-R) model based on the local disk wind

speed is also presented, which is used to parameterize the wind turbine induced aerodynamic forces on the fluid. Finally, the method of simulating the ground roughness and vegetations by using wall functions and canopy models are briefly described.

In Chapter 3, the systematic numerical simulations are conducted to study the wind turbine characteristics under various conditions. Firstly, two kinds of operating condition with different thrust coefficients under two types of inflow with different ambient turbulence intensity are simulated for a model and a utility-scale wind turbine. The predicted mean velocity and turbulence intensity in the wakes of two wind turbines are compared with those obtained from the wind tunnel tests to validate numerical models. Subsequently, eight simulations by the Reynolds Stress Model are conducted for different thrust coefficients, yaw angles and ambient turbulence intensities. The wake deflection, mean velocity and turbulence intensity in the wakes are systematically investigated.

In Chapter 4, a new Gaussian-based analytical wake model for wind turbines considering ambient turbulence intensities and thrust coefficient effects is developed. Firstly, the predictions of wake deficit and added turbulence intensity are modelled, which is derived based on the axial symmetry and self-similarity assumption. In addition, a new wake deflection model is then proposed to analytically predict the wake center trajectory in the yawed condition. The wake deflection model is then incorporated in the proposed Gaussian-based analytical model to consider the yaw angle effects. All the parameters of the proposed model are determined as the function of ambient turbulence intensity and thrust coefficient. The validation of new proposed analytical wake model is conducted under various conditions by comparison with numerical simulations and wind tunnel tests.

In Chapter 5, the procedure of application in real wind farm is presented based on the developed numerical and analytical models. A comprehensive wind farm field measurement conducted in the test site are firstly introduced. The wind field and turbine wake flow over the real terrain are simulated by a modified DDES for different wind directions and the accuracy is assessed by comparing with those measured by a LIDAR in the real wind farm. Subsequently, the escarpment induced terrain effects on the wind turbine wakes are systematically investigated. Finally, a hybrid framework for wake

prediction in real wind farm is developed and verified by the numerical simulation, in which the local wind filed including terrain effects are predicted by a full CFD simulation and the turbine wake effects are presented by the new proposed analytical model.

Chapter 6 summarizes the conclusions of this study. A coupled BEM-CFD model is validated for wake prediction and the effects of ambient turbulence intensity, thrust coefficient and yaw angle are systematically investigated by using numerical simulations. A new analytical wake model is proposed and shows good performance for prediction of mean velocity and turbulence intensity under various ambient turbulence intensity, thrust coefficient and yawed conditions. The terrain effects on the wind turbine wake flow are investigated and the applicability of the new proposed analytical wake model in complex terrain is verified.

ACKNOWLEDGEMENTS

First of all, I would like to express my sincere gratitude and appreciation to my supervisor, Prof. Takeshi Ishihara, for his continuous support, guidance and personal encouragement throughout the period of my doctoral research. His perpetual energy and enthusiasm in research left a deep impression on me and has always been motivating me to improve my academic maturity.

Warm and sincere thanks to Doctoral Committee members, Prof. Ryozo Ooka, Assoc. Prof. Takeyoshi Chibana, Assoc. Prof. Takenori Shimozono and Assoc. Prof. Atsushi Yamaguchi not only for their constructive criticism and valuable comments on the dissertation but also for their kind support throughout this doctoral research.

Sincere gratitude is also expressed to Asst. Prof. Yuka Kikuchi, the researchers Mr. Yutaka Yoshimura, Mr. Haru Namba, Mr. Yoshiteru Tokuyama and secretaries Ms. Chihiro Wada, Ms. Keiko Otaka, for their kind help during my study in the wind tunnel of The University of Tokyo. Special thanks are expressed to Asst. Prof. Jay Prakash Goit, with whom I discussed many academic problems on the topic of wind turbine wakes and wind farm controls, and I learned very much from him. Also thanks to my seniors Dr. Yihong Qi who taught me much about CFD knowledge and detailed techniques, Dr. Shining Zhang who shared lots of academic and life experience with me, and other labmates for their unserved help, encouragement suggestions and friendly approach over the last three years. I am also grateful to all the friends in China and Japan for personally helping me in most difficult times and sharing happiness in daily life.

I am truly indebted and thankful for China Scholarship Council who granted me with the financial support and this incredible opportunity to study in Japan, where I had the chance not only to increase my knowledge but to fulfill my life with amazing experiences. Also, I am most grateful to the Japan-

China Friendship Center for providing me a convenient apartment in the first two years of my study.

I owe everything to my parents who provided never-ending support and love over my entire personal life and educational career. Finally, but most importantly thanks to my dear wife for her love, support and trust in my abilities and personalities; without her encouragement I would not have finished this dissertation.

Guo-Wei Qian

Tokyo, August 20, 2018

CONTENTS

LIST OF PUBLICATION

▪ Papers

[1] 石原孟, 钱 国伟：風車後流の数値予測と解析モデルの提案，第 24 回風工学シンポジウム論文集, p151-156, 2016.

[2] T. Ishihara, G.W. Qian, A new Gaussian-based analytical wake model for wind turbines considering ambient turbulence intensities and thrust coefficient effects. J. of Wind Eng. Indus. Aerodyn, 177, (2018), p275-292, 2018

[3] G.W. Qian, T. Ishihara, (2018) A new analytical wake model for yawed wind turbines. Energies, 11(3), 665, p1-24, 2018

[4] G.W. Qian, T. Ishihara, Numerical study of wind turbine wakes over complex terrain by a modified delayed detached eddy simulation, Proc. of CWE2018, p1-8, 2018.

▪Presentation & Poster in International Conferences

[1] G.W. Qian, T. Ishihara, A Numerical study of wind turbine wake by large eddy simulation and proposal of a new analytical wake model, Offshore Wind Energy 2017, London, UK, 6-8, June 2017.

[2] T. Ishihara, G.W. Qian, Numerical and analytical study of wind turbine wakes in yawed condition, GRE2018, Yokohama, Japan, 17-22, June 2018.

LIST OF FIGURES

LIST OF TABLES

Chapter1. INTRODUCTION

1.1 Background and Motivation

1.1.1 Wind Power Development

Climate change and energy crisis are the most imminent threat to humanity in the 21st century. The traditional energy supply dominated by petroleum, natural gas and coal have put intense pressure on limited resources and the environment. Only by switching to renewable and clean energy could mankind be weaned from the dirty burning fossil fuel for the ever-increasing energy demands to power development and modern living. Wind energy, the most developed and commercialized renewable resource, has been increasingly drawing attention and seeing its marvelous potential. The general, robust increase of wind power around the world which is developing with further geographic diversification is very encouraging (WWEA, 2018). According to the statistics published by Global Wind Energy Council (GWEC, 2018), the overall capacity of all wind turbines installed worldwide by the end of 2017 reached 539,291 MW (see Figure 1-1). In addition, as the most competitively priced technology in many if not most markets worldwide, wind power is extensively utilized in more than 90 countries. There are now 30 countries with more than 1 GW installed and 9 countries with more than 10 GW installed.

Japan's wind power generation started in 1980 but began in full-force with the introduction of 1 MW generating systems in 1999 (Komatsubara, 2012). Many wind turbines have been installed in Hokkaido, Tohoku and Kyushu where the wind conditions are desirable. Recently, Japan accelerates wind power development as the increasing energy needs and

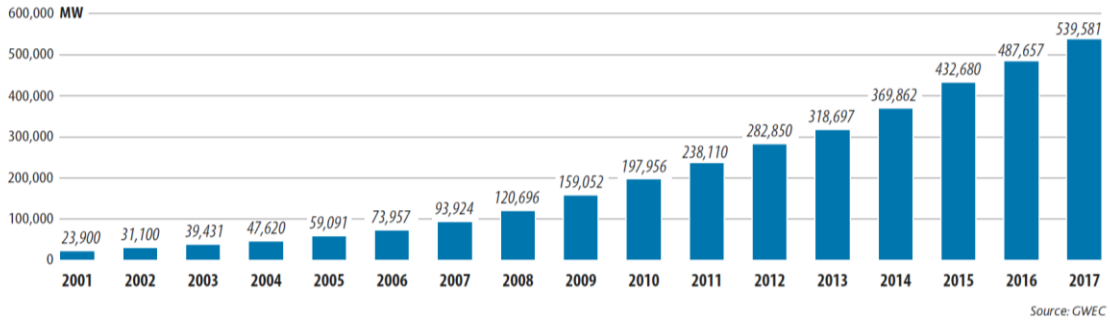

Figure 1-1 Global wind power capacity (WWEA,2018)

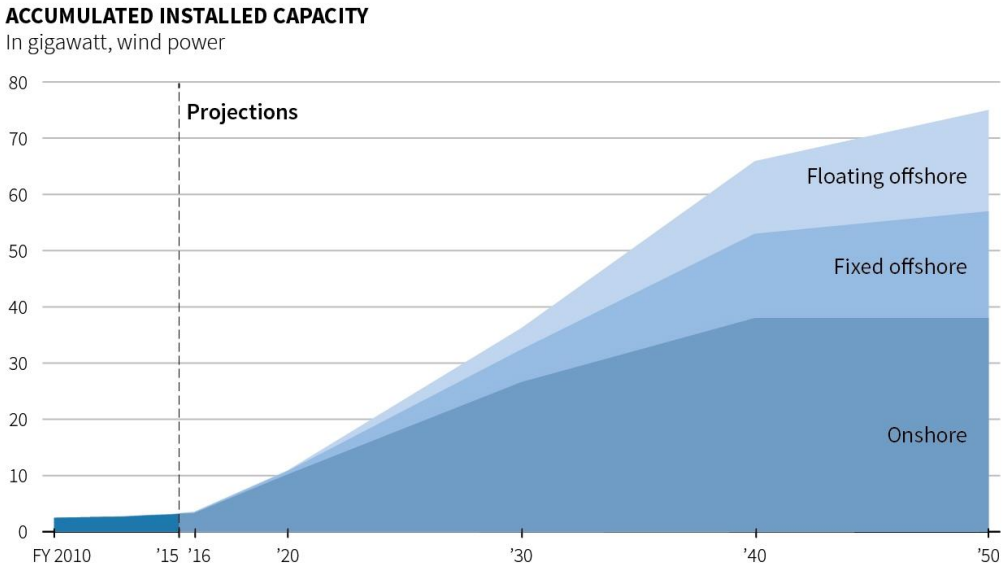

Figure 1-2 Roadmap for Japan's wind power development (JWPA, 2017)

government support. Japan's newly installed wind power capacity in 2016-2017 is set to come in almost double that in 2015, promoted by higher tariffs guaranteed by the government and a rising number of offshore wind farms (Tsukimori, 2017). According to Japan's Wind Power Association (JWPA, 2017), Japan's wind power capacity is set to exceed 35 GW by 2030, more than tenfold the current level, as shown in the roadmap by the industry association (Figure 1-2).

After more than 120 years of development, the modern industry-level wind turbines are more advanced with increasing size, as shown in Figure 1-3. In general, the wind power

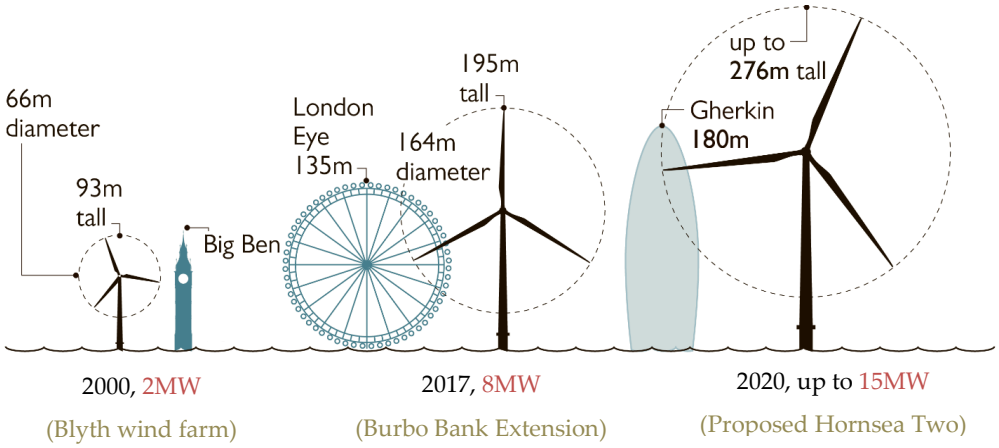

Figure 1-3 Upscaling of wind turbine size (EWEA, 2017)

generation efficiency increases with the upscaling wind turbine size. Firstly, larger size of rotor and blades with wider sweeping areas can extract more energy at a given height, which directly increases the capacity of the turbine. Secondly, as the wind speed normally increases and turbulence intensity decreases with the height in the atmospheric boundary layer, the higher hub height enables the power production factor to be increased and the fluctuating fatigue loads to be decreased. This means that the cost of energy (CoE) can be reduced together with a higher safety factor.

1.1.2 Challenges in Wind Farm

Wind Farm Aerodynamics

One of the challenges facing the wind energy industry is the design of the wind farm layout. A wind farm is a cluster of wind turbines distributed in the same location covering an extended area with the goal of producing electricity obtained for a given investment. For a specified wind farm design, maximizing the power density is the principal goal, and a direct response is that the turbines should be placed as close together as possible. However, it is known that turbines with too close distance tend to interact with the wakes, which results in a significantly decreased power production for the whole wind farm placed. In real situation, the wind farm layout issue is far from this, which involves a wide range of

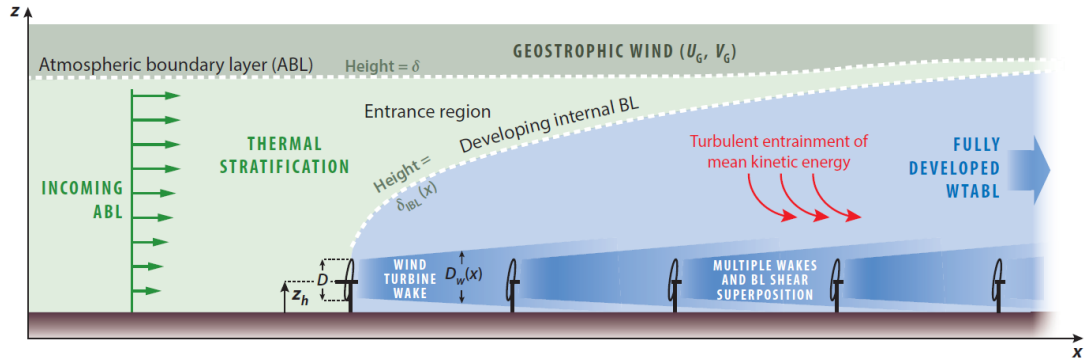

Figure 1-4 Various fluid mechanical flow phenomena in wind farm (Stevens and Meneveau, 2017)

scales spanned by the relevant fluid dynamical flow phenomena, as illustrated in Figure 1-4. Firstly, commercial wind farms have multiple wind turbines operating relatively close to each other. Owing to their proximity, the wakes of the upstream turbines interact with the downstream turbines, leading to significant aerodynamic interference. Such interference between the turbines is referred to as turbine-wake interaction, which is directly related with each single wind turbine performance and the operational conditions. On the other hand, as shown in Figure 1-5, plentiful wind resources exist in various regions on the earth, where the wind farms are operated under different ambient environment, including oceans, coastal regions and mountainous areas.

Offshore Wind Farm

In the offshore wind farm, where the ambient turbulence intensity is lower than that in the terrestrial boundary layer, the wakes recover more slowly and bring severer effects (Ishihara et al., 2004; Wu and Porté-Agel, 2012). Figure 1-5 (a) shows the turbine-wake interaction in Horns-Rev wind farm, Denmark. This is the world first stunning image of wind turbine wakes in real wind farm, in which, it can clearly to identify wind turbine wake regions visualized by the low lying fog (Hasager et al., 2013). In the offshore sites winds are known to be strong and turbulence levels low. However, the cost of installing and maintenance wind farms offshore is still much higher than onshore, due to higher costs for both foundations and connections to the electric grid.

Wind Farm in Coast

Concerns over land utilization, acoustic pollution, and visual impact are forcing the onshore wind farms to move to complex uninhabited terrains. The areas near the coastline are usually the optimal locations for the onshore wind power plant because of the high wind speed and low turbulence levels, especially in the ocean side. However, the cost areas in Japan are also often accompanied with complex terrains in the land side, where the ambient turbulence varies considerably depending on wind direction (Ishihara et al., 2004).

Wind Farm in Mountainous Areas

A complex terrain typically has features like hills, forests, etc., and the effect of such topographical features on the wind turbines is referred to as turbine-terrain interaction. Interference from the terrain adds to the complexity of the wind field. In Japan, 1516 wind turbine accidents have been recorded between the year 2004 and 2012, and 84% of them were for turbines in complex terrains (Watanabe and Uchida, 2015). In the design of a modern wind farm, there is an increased emphasis to understanding the effects of the turbine-wake interaction and terrain-wake interaction.

As we illustrated before, the different ambient environment and turbine operation conditions make the wind farm aerodynamics quite complicated. The most essential two target of wind farm layout design is the power production and turbine safety issue, both of which are affected by the wind turbine wake.

(a) Offshore wind farm, Horns Rev2, Denmark

(b) Wind farm in coast, Tomamae, Japan

(C) Wind farm in mountainous areas, Taikoyama, Japan

Figure 1-5 Wind farms in various ambient environment

1.2 Wind Turbine Wake Effects

When the wind flow passes through a wind turbine with rotating blades, the consequence of the reaction torque is to cause the air to rotate in a direction opposite to that of the rotor. The air gains angular momentum and thus in the wake of the rotor disc the air particles have a velocity component in a tangential direction as well as an axial component (Burton et al., 2011). Figure 1-6 shows the main features of the wake flow visualized by LES simulation under uniform inflow conditions (Chatelain et al., 2014). Tip vortices and flow separations generated by the blade are shed and interact with each other, leading to oscillation, reconnections, and further transition to a turbulent flow field.

Considering the complexity of wind turbine wake flow, a distinct division was made by (Vermeer et al., 2003) to describe the basic features for near and far wake, respectively. The near wake region typically has a length less than three diameters downwind the turbine (Crespo and Hernández, 1996), in which the flow structure essentially depends on the aerodynamics of blades, stalled flow, tip vortices, nacelle and tower. The far wake is the region beyond the near wake, where the rotor features is less important. The research for near wake aerodynamics is mainly focused on the wind turbine performance and the physical process of power extraction, while more research payed attention on the far wake field which is related with the mutual turbine-wake interactions in the wind farm.

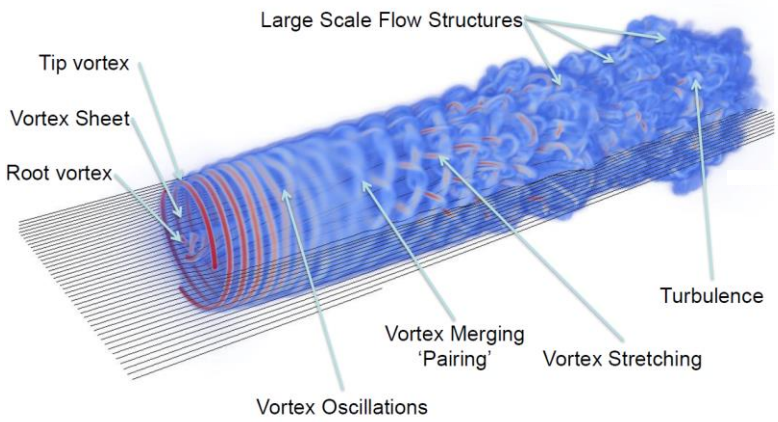

Figure 1-6 Flow structures in the wind turbine wake (Chatelain et al., 2014)

Figure 1-7 furtherly illustrated the wake flow behavior in the atmosphere boundary layer. As the flow approaches the rotor, the stream wind speed decreases and the pressure rises. However, as soon as it goes through the rotor, the pressure drops significantly and reaches the lowest level. As it moves downstream, the influence of the wake expands radially, the velocity on the wake decreases and the local pressure increases sharply until reaching the ambient pressure, which marks the end of the near wake and the beginning of the far wake (Manwell et al., 2010; Vermeer et al., 2003). The difference in wind speed between the flow inside and outside the wake region generates a shear layer, which grows thicker when moving downstream. After this position, the impact of the rotor is no longer predominant and the ambient as well as the mechanically generated turbulence acts as an efficient mixer, dominating the physical wake progression. As a result of this process, far downstream of the rotor, the velocity deficit follows approximately a Gaussian distribution and the streamwise wind speed recovers gradually approaching the non-disturbed values (Sanderse, 2009; Vermeer et al., 2003).

As illustrated in Figure 1-8, wind turbines in a wind farm operating in the downwind wake flow are subjected to two main problems: decreased energy production due to the velocity deficit and increased fatigue loading due to the added turbulence intensity generated by the upwind turbine (Barthelmie et al., 2009; Vermeer et al., 2003). For example, Neustadter and Spera (1985) found a reduction of 10% in power output for three turbines separated by 7 rotor diameters. For full wake conditions, power losses of downstream turbines can be 30-40% (Barthelmie et al., 2009). On the other hand, the wake added turbulence intensity

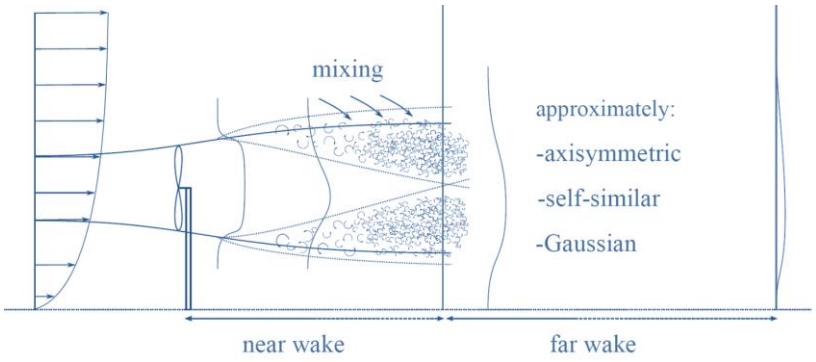

Figure 1-7 Schematic representation of the turbine wake (Sanderse, 2009).

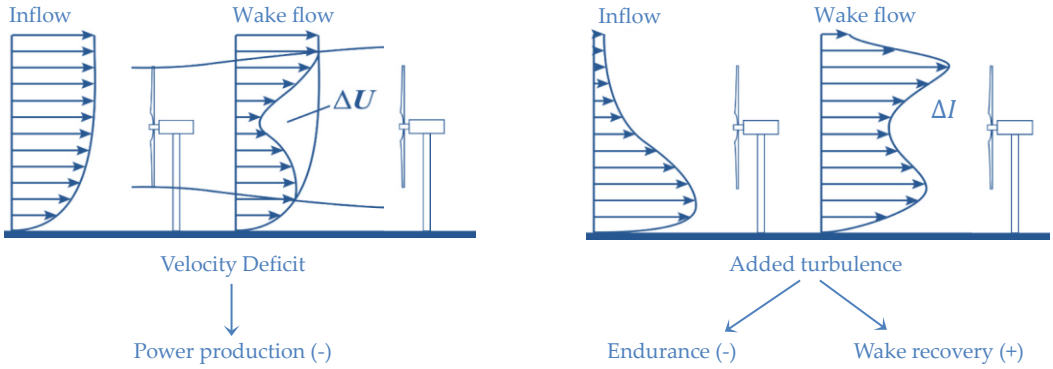

(a) Momentum Change (b) Turbulence Change

Figure 1-8 Wind turbine wake effects

will also increase the turbulence level in the atmosphere for large wind farms, accelerating the wake recovery hence increasing the efficiency of wind farm (Goit and Meyers, 2015).

In order to reduce power losses and to improve the lifetime of the wind turbine, three scopes can be defined for the wake modelling in real engineering application, as illustrated in Figure 1-9.

1. Power production prediction considering wake effects: this requires the time-averaged velocity profile behind a turbine.

2. Wind turbine load evaluation: in order to calculate the fatigue/dynamic load of turbines operating in the wake, the turbulence intensity should be estimated carefully.

3. Control strategies: the turbine operational conditions including the pitch angle, yaw angle, rotational speed etc. directly have impacts on the wake behavior; on the other hand, as shown in Appendix A, the wind turbine control system should work based on the wind condition at the local site, which is also affected by the wake itself.

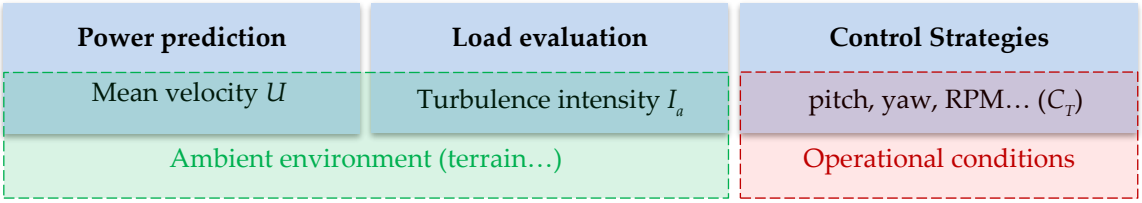

Figure 1-9 Scopes in needs of wake modelling

1.3 Literature Review

Wind turbines wakes have been an active area of research in the past three decades. A diverse range of literature, focusing on different aspects of the current problem of interest is available. For present purposes, they are classified into numerical simulation, analytical modeling, and application in real wind farms.

1.3.1 Numerical Studies

Prediction of wake effect requires a detailed understanding of the behavior of wake flow and its interaction with atmospheric boundary layer. In previous studies, the wake characteristics in the atmospheric boundary layer have been investigated by wind tunnel tests (Chamorro and Porte-Agel, 2009; Ishihara et al., 2004), however, it is difficult to capture the detailed turbulence structure due to the constraint of measurement.

Wind Turbine Modelling

In recent years, computational fluid dynamics (CFD) has been used to study wind turbine wake flow and to optimize wind farm layout (Sanderse et al., 2011). In these studies, the large-eddy simulation (LES) was popularly used for the study of wind turbine wake characteristics, and the wind turbine induced forces were modelled using either of the two approaches, the generalized actuator disk model (ADM) or actuator line model (ALM). The ALM is used to reproduce detailed three-dimensional rotational effects, like tip vortices. However, it is noted that finer mesh and smaller time steps are required for ALM, thus this method is costly for LES simulation of a large wind farm. According to the study in reference (Witha et al., 2014), the CPU time of ALM simulation is greatly enhanced compared to the ADM simulation by a factor of 4~12 depending on the grid resolution. The earliest version of ADM is the actuator disk model without rotation (ADM-NR), in which the turbine induced force is parameterized as an overall thrust force uniformly acting on the rotor disk (Calaf et al., 2010; Goit and Meyers, 2015; Jiménez et al., 2007). Another extended ADM uses the blade element momentum (BEM) theory (Burton et al., 2011) to calculate the lift and drag forces and then unevenly distribute them on the actuator disk.

This modified approach is referred to as the actuator disk model with rotation (ADM-R). The ADM-R has been employed in LES simulation and validated by the wind tunnel tests for the wind turbine wakes in turbulent boundary layers (Wu and Porté-Agel, 2012, 2011).

Although the detailed characteristics of mean velocity and turbulence in the turbine wake have been examined in these studies (Wu and Porté-Agel, 2011; Xie and Archer, 2014; Yoshizawa and Ishihara, 2015), the effect of ambient turbulence intensity and thrust coefficient require further systematic investigation. On the other hand, it should be noted that the ADM-R model applied in the above research utilized the known incoming wind speed as the constant input to update the rotor force. However, this approach is not applicable in real wind farm simulations, which will be discussed in detail in section 2.3.1

Yaw Conditions

In an attempt to address the power losses induced by the wake for downstream wind turbines, there have been extensive studies considering adjusting tip speed ratios, blade pitch controls and varying yaw angle (Adaramola M.S. and Krogstad P.-Å., 2011; Mikkelsen et al., 2013; Wagenaar et al., 2012). Yaw control is one of the promising methods for wind farm power optimization, and it is implemented by an intentional yaw misalignment of the turbine to the wind direction (Gebraad et al., 2014; Medici, D., & Dahlberg, 2003). This approach relies on an induction of a lateral momentum by actively yawing the upwind turbine to deflect the wake away from the downwind turbines, so that the latter can extract more energy from unwaked flow. Optimization procedures are necessary to maximize the power production of the whole wind farm since there is also a power reduction for the yawed turbine itself. Therefore, accurate evaluations of the deflected wake trajectory and the wake characteristics of a yawed wind turbine are essential for applying yaw control strategies in actual wind farms.

Similarly, prediction of the wake characteristics under various yawed conditions requires a detailed understanding of the behavior of wake flow and its interaction with the atmospheric boundary layer. Parkin et al. (2001) obtained the detailed velocity field from one to five rotor diameters downstream of a two-bladed wind turbine model under various yaw angles by using PIV and showed the initial skew angle of wakes. Medici and

Alfredsson (2006) and later Howland et al. (2016) performed the hot-wire measurement for a two-bladed and a porous disk model turbine, respectively, and quantified the velocity deficit and deflections in various yawed conditions. Note that these wind tunnel tests were carried out in a uniform flow. Recently, Bastankhah and Porté-Agel (2016) systematically studied the wake of a yawed turbine under various thrust coefficients and yaw angles by the detailed wind tunnel measurements in a neutral stratified boundary layer. CFD has also been widely used to study wind turbine wake flows and power production optimization in a wind farm (Sanderse et al., 2011). Jiménez et al. (2009) used large-eddy simulation (LES) to characterize the wake deflections under a range of yaw angles and thrust coefficients for a turbine modeled with a uniformly distributed actuator disk model without rotation (ADM-NR). Later, Fleming et al. (2014) applied LES with actuator line model (ALM) to investigate several methods for improving wind plant overall performance, and the yaw control proved to be effective with wake-redirection. Luo et al. (2014) conducted the single turbine skew analysis by using LES and showed that the wake deflection was almost linear in the near wake region for moderate yaw angles. However, in those above prior research works, the effects of thrust coefficients, ambient turbulence and yaw angle have not been investigated systematically for the wake deflection for yawed wind turbines.

1.3.2 Analytical Wake Model

In comparison to wind tunnel tests and numerical simulations, wake models have advantages in designing and optimizing wind farm layout because of its simplicity and high efficiency (Crespo et al., 1999). The wake can be generally divided into near wake region and far wake region (Vermeer et al., 2003). The near wake region typically has a length less than three diameters downwind the turbine (Crespo and Hernández, 1996), which is complicated to cope with due to the fact that it is significantly affected by the blade aerodynamics, stalled flow, tip vortices as well as nacelle and tower (Vermeer et al., 2003; Xie and Archer, 2014). Thus, most wake modelings mainly focus on the far wake region, where the wake is fully developed and the velocity deficit and the added turbulence intensity can be assumed axisymmetric and have self-similar distributions in the wake

cross-sections (Vermeer et al., 2003).

Velocity Deficit

Prediction of the velocity deficit is the primary objective of wake models. One of the classical and widely used wake model for velocity deficit was proposed by Jensen (1983), and was developed further by Katic et al. (1986), which assumes a linearly expanding wake with a uniform profile, termed "a top-hat shape", for the velocity deficit. The Katic et al.'s model only considers the mass conservation. More recently Frandsen (2006) proposed a model that applied the balance of momentum in addition to the mass conservation. It still took a top-hat assumption for the velocity deficit. In comparison with the top-hat assumption, Gaussian distribution is more reasonable for the velocity deficit profile in wake cross section, which was derived by Ishihara et al. (2004) and observed in the experimental data (Chamorro and Porte-Agel, 2009; Ishihara et al., 2004) and numerical simulations (Xie and Archer, 2014). It was also employed in several wake models (Ainslie, 1988; Bastankhah and Porté-Agel, 2014; Gao et al., 2016; Ishihara et al., 2004). However, there are still problems of robustness and universality for these models.

Added Turbulence Intensity

Modelling the turbulence in wind turbine wake flows is also important since the wake induced turbulence increases the fatigue loading of the downwind turbine. Considering the complex nature of turbulence, it is common to model the maximum added turbulence intensity $\Delta I_{1\max}$, which normally occurs at the top tip height level. Based on the measurement data, Quarton (1989) proposed a widely used empirical expression for $\Delta I_{1\max}$, which is proportional to thrust coefficient and, ambient turbulence intensity. The distance from wind turbine was normalized by the estimated near wake length x_N defined by Vermeulen (1980). The parameters in Quarton's model were modified by Hassan (1990) based on wind tunnel measurements. Crespo and Hernández (1996) proposed a similar model for $\Delta I_{1\max}$, which is related to the induction factor and ambient turbulence intensity. These three wake models are quite similar and show overestimation in the near wake region. In addition, the distribution of added turbulence intensity in the wake cross section

is also important in the wind farm layout design and has not been investigated yet.

Wake deflection

The wake model for non-yawed turbines and the application in wind farm have been extensively studied (Stevens et al., 2015; Yang and Sotiropoulos, 2016). By contrast, the analytical studies for the wake under a yawed condition have not received much attention. Jiménez et al. (2009) presented a preliminary analysis of wakes on the leeward of a yawed turbine for the first time. He proposed a simple formula to predict the wake skew angle based on the momentum conservation and top-hat model suggested by Jensen (1983) for the velocity deficit. However, experimental validation was not sufficient as the author mentioned. Gebraad et al. (2014) and Howland et al. (2016) derived the formula of yaw induced wake center trajectory by integrating the skew angle proposed by Jiménez et al. (2009). However, the model of Jiménez et al. (2009) overestimates the wake deflection since the assumption of top-hat for the velocity deficit is not accurate as pointed out by Ishihara et al. (2004). Based on the theoretical analysis of the governing equations, Bastankhah and Porté-Agel (2016) developed an analytical model to predict the wake deflection and the far wake velocity distributions for the yawed turbines. The model showed good agreement with the experimental data. However, some parameters in this model have not been specified. In addition, the turbulence characteristic in the wake of the yawed turbine is also of great importance as it has a significant impact on the wake development. The investigation of turbulence characteristic and the corresponding analytical model are not included in existing studies.

1.3.3 Application in Real Wind Farm over Complex Terrain

Wind turbine wakes in real wind farm involve different aspects of studies, including wind prediction over terrain, wind turbine wake characteristics over complex terrain and wind turbine wake modelling considering terrain effects. Prior works are summarized based on the above mentioned scopes as follows.

Wind prediction over complex terrain

According to previous researches, it can be concluded that turbulent flow over steep terrain with rough surface can be well predicted by both RANS model (Ishihara and Hibi, 2002) and LES model (Iizuka and Kondo, 2006, 2004; Tamura et al., 2007). However, RANS model cannot predict well both mean wind velocity and turbulence at the wake region of steep terrain with smooth surface. When LES model is used for steep smooth hill, the mean velocity can be well predicted, but there is still some discrepancy between predicted turbulence intensity and experimental data such as overestimation of turbulence intensity at wake region and unreasonable peak of turbulence intensity at the crest (Liu et al., 2016; Tamura et al., 2007). This discrepancy arises mainly due to inaccurate modelling of thin surface roughness in the simulation with LES model. In the case following wind tunnel experiment, it might acceptable to apply non-slip boundary condition in the simulation. But the ground surface in the real situation can never be smooth enough to allow the application of non-slip boundary condition. One choice to modelling surface roughness correctly is applying canopy model, however, the requirement on horizontal grid resolution corresponding to the canopy height makes the simulation with LES very expensive. Alternatively, it is reasonable to consider a combination of RANS model with LES model. The former can provide accurate boundary condition, which is validated in flat terrain condition, and the latter can be used to capture important turbulence structures in the wake region. Bechmann and Sørensen (2010a) attacked this purpose by combining model and LES model on the investigation of turbulent flow over the Askervein hill, which is a relatively isolated low hill of 116m height and is essentially elliptical in plan form with a 1km minor axis and a 2km major axis. The roughness length was measured during the field investigation and found to range from 0.01m to 0.05m (Taylor and Teunissen, 1987). The hybrid model is able to capture the high turbulence level well but underestimated the mean velocity. Recently, a modified DDES model is proposed by Ishihara and Qi (2018), which limited the region where the realizable $k-\varepsilon$ model is applied. The modified DDES model is then validated all four steep terrains, steep 2D ridge and 3D hill with smooth and rough surface. However, the performance of this modified DDES model for predicting the wake flow over complex terrain in real farm has not been examined.

Wind Turbine Wakes Over Complex Terrain

Extensively numerical studies by using CFD have been performed in the research field of wind turbine wakes over complex terrain. In the early stage, the wake and terrain effects were superposed by linear models (Crespo et al., 1993). These linearized models were found to be able to provide acceptable results only for moderate complex terrain with attached flows (Migoya et al., 2007). Later on, most of the numerical investigation of the wake flow over the ideal and realistic terrains are conducted based on the Reynolds-Averaged Navier-Stokes (RANS) Equations with $k-\varepsilon$, $k-\omega$ and RSM turbulence closures (Barthelmie et al., 2012; Daaou Nedjari et al., 2017; Makridis and Chick, 2013; Murali and Rajagopalan, 2017). However, these RANS-based models still have some limitations of wind prediction over complex terrain with smooth surface as pointed by Ishihara and Qi (2018). Alternatively, Large Eddy Simulation (LES) was employed to study the terrain effects of an ideal 3D hill (Yang et al., 2015) and 2D ridge (Shamsoddin and Porté-Agel, 2017) for the model wind turbine wakes. Yang et al. (2014) and Berg et al. (2017) performed the LES to simulate the flow through a hypothetical wind farm situated downwind of complex terrain and the wake flow over a real complex terrain, respectively. Whereas, very limited literatures focus on the application of hybrid RANS/LES model in this field. The only work that evaluated the terrain effects on the wind turbine regards to power and loads by using the Delayed Detached Eddy Simulation (DDES), to our knowledge, was carried out by Schulz et al. (2016). However, one notes, these numerical simulations for the real complex terrain wind farm are lack of measurement validation.

Wake model application in complex terrain

To reduce the cost of optimizing wind farm layouts and turbine operations, a low time cost wake modelling which can consider the terrain effects simultaneously is essential in real application. Han et al. (2012) utilized a simple model proposed by Lissaman (1979) to describe the wake effect of a complex terrain and to optimize the layout of wind turbines on hilly terrains. However, the accuracy of the wake effects evaluation is not validated by any field experiment data. Feng and Shen (2014) utilized an analytical wake model to approximate the wake effects, which is then super-positioned onto a 2D Gaussian hill terrain with the assumption that the center of the wake travel along the terrain at hub height. It should be noted that this simple assumption may work for local moderate

terrains, but cannot be universally applicable to more complex topography conditions. In order to reduce the computational cost of wake modeling while remaining accurate in wake predictions, Kuo et al. (2018) developed a numerical wake model for simulating wakes on complex terrains. The model solves a simplified variation of the Navier-Stokes equations with simplifications and assumptions to reduce computational cost while maintaining accuracy. This approach requires an initial CFD simulation of a wind farm domain without turbines in order to obtain the uninterrupted flow field. The information from full CFD simulation in regards to the flow and turbulent viscosity is extracted and interpolated for the proposed model. These interpolated values are then used as initial conditions in the model. Finally, the internal velocity boundary condition based on the actuator disk theory is used to describe the wake expansion and velocity deficit approximately 2 rotor diameters downstream of the turbine. However, before application in complex terrains, the model parameters must be properly fitted with CFD data of wake simulation. Another point is that the terrain induced wind direction changes in the turbine local site were not considered in those approaches, which limits its accuracy of wake effects evaluation for wind farm in complex terrain.

1.4 Objectives and Structure of the Thesis

According to the previous researches and remaining problems, three main objectives are set in this study as follows.

(1) Update the ADM-R model by using the local velocity for wake simulation and then to study the effects of ambient turbulence intensity, thrust coefficient and yaw angle on the single turbine wakes.

(2) Propose an analytical wake model applicable to various ambient turbulence intensity, thrust coefficient and yawed conditions.

(3) Apply the updated numerical approach and analytical model for wake prediction in real wind farm considering terrain effects.

After an introduction in Chapter 1, the governing equations, turbulence models, wind

turbine models and roughness model used in the present study will be presented in Chapter 2. In Chapter 3, the systematic numerical simulations are conducted and compared with the experimental data. Firstly, two kinds of operating condition with different thrust coefficients under two types of inflow with different ambient turbulence intensity are simulated for a model and a utility-scale wind turbine. The predicted mean velocity and turbulence intensity in the wakes of two wind turbines are compared with those obtained from the wind tunnel tests to validate numerical models. Subsequently, eight simulations by the Reynolds Stress Model are conducted for different thrust coefficients, yaw angles and ambient turbulence intensities. The wake deflection, mean velocity and turbulence intensity in the wakes are systematically investigated. In Chapter 4, a new analytical wake model for wind turbine with Gaussian distribution for the velocity deficit and added turbulence intensity is developed. The new wake model is proposed to predict the mean velocity and turbulence intensity distribution in the wake regions of wind turbines. The model is derived based on the axial symmetry and self-similarity assumption for wake deficit and added turbulence intensity. All the parameters of the proposed model are determined as the function of ambient turbulence intensity and thrust coefficient identified based on the various large eddy simulations. In addition, a new wake deflection model is then proposed to analytically predict the wake center trajectory in the yawed condition. Finally, the effects of yaw angle are incorporated in the Gaussian-based wake model. In Chapter 5, the procedure of application in real wind farm is presented based on the developed numerical and analytical models. The wake of wind turbine in a complex terrain site is investigated by a modified DDES. The turbulent flows over the real terrain are simulated for different directions and the accuracy is assessed by comparing those measured by a LIDAR in the real wind farm. Based on the local wind prediction by numerical simulation, the terrain effects are incorporated in the new proposed wake model for the wake prediction in real wind farm. Finally, Chapter 6 summarizes the conclusions of this study.

The roadmap of this thesis is summarized in Figure 1-10.

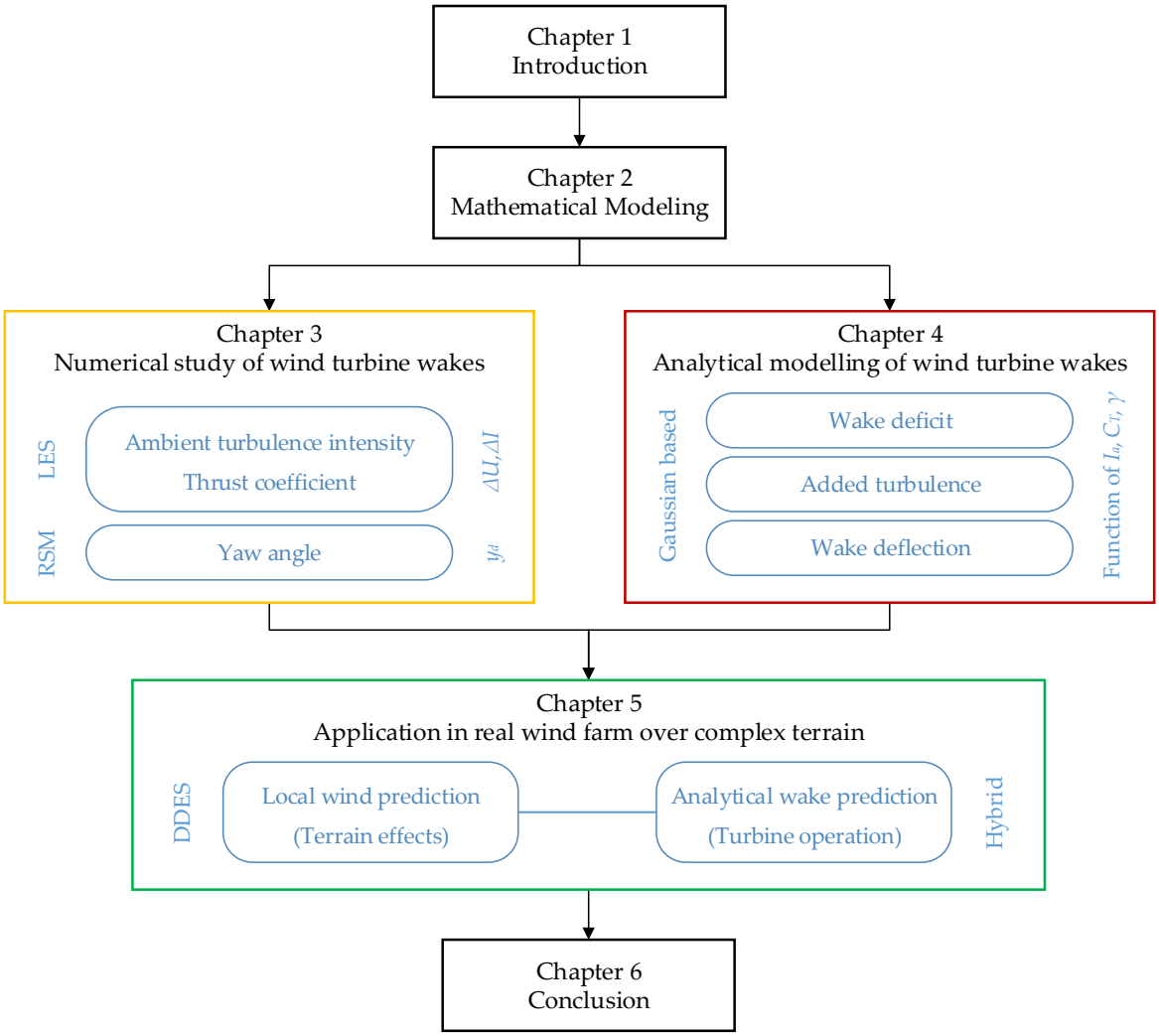

Figure 1-10 Roadmap of the thesis

Chapter2. MATHEMATICAL MODELING

2.1 Introduction

The present chapter is used to establish the mathematical conventions adopted in the numerical studies. Firstly, the Finite Volume Method (FVM) is applied for the discretization of the partial differential equations arising from the mathematical modeling of the fluid dynamics investigated. Several turbulence models to close the governing equations are introduced, which are used to simulate the wind turbine wake flows. An updated wind turbine model to parameterize the rotor induced forces on the wind flow are introduced subsequently. Finally, the roughness model including wall functions and canopy model, are explained.

2.2 Turbulence Model

Generally, two different approaches were used for the analysis of the flow field with obstacles inside. The first one constructed the governing equations for the fluid part only, in which the solid wall conditions are applied for the obstacles. The second approach constructed the governing equations for the whole computational domain, where the obstacles effects are normally represented by a momentum sink in the flow field. In this study, the latter approach is utilized to simulate the wind turbine wake flow and also the turbulent flow over canopy layers. For a complete reference on this subject, the interested reader could refer to the textbook by (Ferziger and Perić, 2002).

It is noted that the physical filtered Navier-Stokes equations for Large Eddy Simulation

(LES) have the almost same format as the Reynolds-Averaged Navier-Stokes (RANS) equations. Accordingly, the subsequent discussion for governing equations would be carried out simultaneously for these two categories of turbulence model. The averaged/filtered continuity and momentum equations can, for incompressible flow with external force, be written in tensor notation and Cartesian coordinates as shown in Equation (2-1) and Equation (2-2).

$$\frac{\partial \rho \tilde{u}_i}{\partial x_i} = 0 \tag{2-1}$$

$$\frac{\partial}{\partial t}(\rho \tilde{u}_i) + \frac{\partial}{\partial x_j}(\rho \tilde{u}_i \tilde{u}_j) = \frac{\partial}{\partial x_j}\left(\mu\left(\frac{\partial \tilde{u}_i}{\partial x_j} + \frac{\partial \tilde{u}_j}{\partial x_i}\right)\right) - \frac{\partial \tilde{p}}{\partial x_i} - \frac{\partial \tau_{ij}}{\partial x_j} + f_{\tilde{u},i} \tag{2-2}$$

where the Einstein summation notation is used. $\tilde{u}_i$ (i=1, 2 and 3) denote the velocity component in ith direction. $\tilde{p}$ is the pressure respectively, ρ is the air density, and μ is the dynamic viscosity. The terms in Equation (2-2), in order from left to right, are unsteady, advection by the mean flow, diffusion, pressure gradient force, turbulent diffusion and source term. The momentum source term $f_{\tilde{u},i}$ represents the external force per unit grid volume on the flow. Further description for the body forces induced by wind turbine and canopy are introduced in section 2.3 and 2.4.

From a numerical point of view, velocity component, pressure and external force can be decomposed is the way as the following equation:

$$u_i = \tilde{u}_i + u'_i \tag{2-3}$$

Formally, in the sense of LES model, the tilde $(\tilde{\cdot})$ denotes the resolved component and the prime $(\cdot')$ denotes sub-grid scale component. On the other hand, for RANS model, the Equation (2-3) is interpreted as the Reynolds decomposition, in which any variable is decomposed into its temporary mean $(\tilde{\cdot})$ and a fluctuating $(\cdot')$ component.

τ_{ij} is introduced to consider the difference between $\widetilde{u_i u_j}$ and $\tilde{u}_i \tilde{u}_j$ as shown in the following equation and should be modeled by turbulence model.

$$\tau_{ij} = -\rho\left(\widetilde{u_i u_j} - \tilde{u}_i \tilde{u}_j\right) \tag{2-4}$$

The continuity and momentum equations for simulation with RANS, LES and Hybrid model are identical in form. The difference in applying different turbulence model is only

represented in how τ_{ij} is modeled to close Equation (2-2). For LES, τ_{ij} are called subgrid-scale Reynolds stresses, which modeling the contribution from subgrid-scale vortex (unresolved) to large vortex (resolved). On the other hand, for RANS, τ_{ij} are called Reynolds stresses ($-\rho\widetilde{u'_\iota u'_\jmath}$), which modeling the effect of fluctuating wind component to the mean wind component.

2.2.1 Reynolds Stress Model

The Reynolds Stress Model (RSM) accounts for the anisotropic turbulence stresses to give accurate predictions for complex flows, which is an important advantage compared to the common one-Equation and two-Equation models with isotropic eddy-viscosity hypothesis. Additionally, as pointed out by Cabezón et al. (2011), the common two-Equation RANS model like the standard k-ε model could not provide good prediction for the wind turbine wakes, while RSM shows better performance. Some of the modified two-Equation model may improve the accuracy but they are still very dependent on how their parameters are tuned for different cases.

In this study, the RSM with Linear Pressure-Strain model in ANSYS (Ansys, Inc., Canonsburg, PA, USA) Fluent (Ansys Inc., 2011) is used to express the Reynolds stress tensor ($-\rho\widetilde{u'_\iota u'_\jmath}$) to close the momentum equation. In RSM, a set of Reynolds stress Equations for the turbulence closure are introduced as follows:

$$\frac{\partial\left(\rho\widetilde{u'_\iota u'_\jmath}\right)}{\partial t}+\frac{\partial\left(\rho\widetilde{u_k}\widetilde{u'_\iota u'_\jmath}\right)}{\partial x_k}=\frac{\partial}{\partial x_k}\left[\left(\frac{\mu_t}{\sigma_k}+\mu\right)\frac{\partial\widetilde{u'_\iota u'_\jmath}}{\partial x_k}\right]+P_{ij}+\phi_{ij}-\varepsilon_{ij} \tag{2-5}$$

where σ_k is a model constant with the value of 0.82 according to Lien and Leschziner (1994). μ_t is the turbulence viscosity and calculated in the same way as in the k-ε model by using the following Equation:

$$\mu_t=C_\mu\rho\frac{\tilde{k}^2}{\tilde{\varepsilon}} \tag{2-6}$$

where $C_\mu=0.09$. P_{ij} is the term for stress production calculated as

$$P_{ij} = -\rho\left(\widetilde{u'_i u'_j}\frac{\partial \tilde{u}_j}{\partial x_k} + \widetilde{u'_j u'_k}\frac{\partial \tilde{u}_i}{\partial x_k}\right) \tag{2-7}$$

ϕ_{ij} is the pressure strain term, modelled according to the proposals by Gibson and Launder (1978), Fu et al. (1987), and Launder (1989), as shown in the following Equation

$$\phi_{ij} = -C_1\rho\frac{\varepsilon}{k}\left(\widetilde{u'_j u'_k} - \frac{2}{3}\delta_{ij}k\right) - C_2\left(P_{ij} - C_{ij} + \frac{1}{3}\delta_{ij}C_{kk}\right) \tag{2-8}$$

where the model constants C_1 and C_2 are 1.8 and 0.6, respectively. C_{ij} is the convective term in Equation (2-7) and calculated by

$$C_{ij} = \frac{\partial\left(\rho\tilde{u}_k\widetilde{u'_i u'_j}\right)}{\partial x_k} \tag{2-9}$$

ε_{ij} is the dissipation term modelled as

$$\varepsilon_{ij} = \frac{2}{3}\delta_{ij}\rho\tilde{\varepsilon} \tag{2-10}$$

Equation (2-7) is solved for each of the different Reynolds stresses. Similar to k-ε model, additional Equations are necessary to calculate turbulent kinetic energy k and its dissipation rate ε:

$$\frac{\partial\left(\rho\tilde{k}\right)}{\partial t} + \frac{\partial(\rho\tilde{u}_i\tilde{k})}{\partial x_i} = \frac{\partial}{\partial x_j}\left[\left(\mu + \frac{\mu_t}{\sigma_k}\right)\frac{\partial\tilde{k}}{\partial x_j}\right] + \frac{1}{2}P_{ii} - \rho\tilde{\varepsilon} \tag{2-11}$$

$$\frac{\partial\tilde{\varepsilon}}{\partial t} + \frac{\partial(\rho\tilde{u}_i\tilde{\varepsilon})}{\partial x_i} = \frac{\partial}{\partial x_j}\left[\left(\mu + \frac{\mu_t}{\sigma_\varepsilon}\right)\frac{\partial\tilde{\varepsilon}}{\partial x_j}\right] + C_{\varepsilon 1}\frac{1}{2}P_{ii}\frac{\tilde{\varepsilon}}{\tilde{k}} - C_{\varepsilon 2}\frac{\rho\tilde{\varepsilon}^2}{\tilde{k}} \tag{2-12}$$

where $\sigma_\varepsilon = 1.0$, $C_{\varepsilon 1} = 1.44$, $C_{\varepsilon 2} = 1.92$.

2.2.2 LES Model

In the LES, large eddies are directly computed, while the influences of eddies smaller than grid spacing are parameterized. The subgrid-scale (SGS) Reynolds stresses τ_{ij} is also need models to estimate it, which have been historically called as subgrid models. In general, subgrid models commonly used in LES can be broadly divided into two groups: eddy-viscosity models, and scale-similarity mdoels. The eddy viscosity models assume a direct

correlation between the subgrid-scale stress and the large-scale strain rate tensors. In this thesis, one of the eddy viscosity models, Smagorinsky-Lill model (Smagorinsky, 1963) is used to calculate the SGS Reynolds stress as follows.

Firstly, based on the eddy viscosity hypothesis by Bounssinesq (1877), τ_{ij} are assumed as product of the fluid strain and an eddy viscosity:

$$\tau_{ij} = -2\mu_t \tilde{S}_{ij} + \frac{1}{3}\tau_{kk}\delta_{ij} \tag{2-13}$$

where $\tilde{S}_{ij}$ is the rate-of-strain tensor defined as follows:

$$\tilde{S}_{ij} \equiv \frac{1}{2}\left(\frac{\partial \tilde{u}_i}{\partial x_j} + \frac{\partial \tilde{u}_j}{\partial x_i}\right) \tag{2-14}$$

δ_{ij} is the Kronecker delta and the term $(\delta_{ij}/3)\cdot\tau_{kk}$ is absorbed into the pressure term following standard practice (Bechmann and Sørensen, 2010b) .

μ_t denotes the eddy viscosity, which is modelled as:

$$\mu_t = \rho L_S^2 |\tilde{S}| = \rho L_S^2 \sqrt{2\tilde{S}_{ij}\tilde{S}_{ij}} \tag{2-15}$$

where L_S denotes the mixing length for subgrid-scales and it is calculated by:

$$L_S = min(\kappa\delta, C_S V^{1/3}) \tag{2-16}$$

κ is the von Karman constant, 0.42, δ is the distance to the closet wall and V is the volume of a computational cell. C_S is Smagorinsky constant and assumed from the Kolmogorov constant C_K, i.e.

$$C_s = \frac{1}{\pi^2}\left(\frac{3C_K}{2}\right)^{3/2} \tag{2-17}$$

Which for $C_K \approx 1.4$ gives a value $C_s \approx 0.033$. As have been pointed out by (Ferziger and Perić, 2002) that C_s is not constant and may be a function of Reynolds Number and/or other non-dimensional parameters and may take different values in different flows. In this study, based on the research by Oka and Ishihara (2009), smagorinsky constant, C_s, is determined as 0.032.

2.2.3 DDES Model

In many previous researches, LES model has shown obvious better performance than RANS models. However, high computational cost and difficulty on predicting wall-bounded flows in high Reynolds number flow make this model less attractive. It's natural to consider combining LES model with RANS model, which is less grid dependency and therefore can help to reduce the total computational cost. On the other hand, near-wall eddies are modeled by RANS model makes it suitable for high Reynolds number flows.

A comprehensive review on hybrid RANS/LES model was provided by Fröhlich and von Terzi (2008). In this review, hybrid RANS/LES models are classified into two large categories, segregated RANS/LES and unified RANS/LES models. The first one, segregated modeling, applying LES and RANS model separately in different subdomains and then coupled via appropriate boundary conditions. The resolved quantities with segregated modeling are not continuous at the interface except for laminar flows. On the contrary, unified modeling blend RANS and LES model based on the identity of governing equations. In the light of how RANS and LES model blended, unified modeling can be further classified into three categories, hard interface, soft interface and blending.

The detached eddy simulation (DES) model blends the RANS and LES model according to the idea of switching length scale in partial differential Equations. It was first proposed by Shur et al. (1999) with one-Equation RANS model, the Spalart-Allmaras model. Then, it was developed to blend with other RANS models like $k-\varepsilon$ model and $k-\omega$ model.

In this study, the Delayed Detached Eddy Simulation (DDES) is utilized for the wind turbine wake in complex terrain, in which the realizable $k-\varepsilon$ model and two equations LES model are used. The transportation Equations for $\tilde{k}$ and $\tilde{\varepsilon}$ are:

$$\frac{\partial(\rho\tilde{k})}{\partial t}+\frac{\partial(\rho\tilde{k}\tilde{u}_i)}{\partial x_i}=\frac{\partial}{\partial x_j}\left[\left(\mu+\frac{\mu_t}{\sigma_k}\right)\frac{\partial\tilde{k}}{\partial x_j}\right]+G_k+Y_k \tag{2-18}$$

$$\frac{\partial(\rho\tilde{\varepsilon})}{\partial t}+\frac{\partial(\rho\tilde{\varepsilon}\tilde{u}_i)}{\partial x_i}=\frac{\partial}{\partial x_j}\left[\left(\mu+\frac{\mu_t}{\sigma_\varepsilon}\right)\frac{\partial\tilde{\varepsilon}}{\partial x_j}\right]+C_{\varepsilon1}G_k\frac{\tilde{\varepsilon}}{\tilde{k}}-C_{\varepsilon2}\rho\frac{\tilde{\varepsilon}^2}{\tilde{k}} \tag{2-19}$$

where G_k represents the generation of turbulent kinetic energy due to the mean velocity

gradients. In a manner consistent with the Boussinesq hypothesis, G_k is calculated by Equation (2-20). The term Y_k represents the dissipation of turbulent kinetic energy and is calculated by Equation (2-21). Parameters $C_{1\varepsilon}$ =1.44, $C_{2\varepsilon}$ =1.92, σ_k =1.0 and σ_ε =1.3 are the constants (Ansys Inc., 2011).

$$G_k = \mu_t |\tilde{S}|^2, \qquad |\bar{S}| = \sqrt{2\tilde{S}_{ij}\tilde{S}_{ij}} \tag{2-20}$$

$$Y_k = -\frac{\rho \tilde{k}^{\frac{3}{2}}}{l} \tag{2-21}$$

l in Equation (2-21) is the turbulence length scale. In the DDES model, it is given by

$$l = l_{RANS} - f_d max(0, l_{RANS} - l_{LES}) \tag{2-22}$$

where l_{RANS} and l_{LES} are the turbulence length scales of the RANS and LES models, respectively. f_d is a control function to select the regions applying the RANS and LES models. l_{RANS}, l_{LES} and f_d are written as

$$l_{RANS} = \frac{\tilde{k}^{\frac{3}{2}}}{\bar{\varepsilon}} \tag{2-23}$$

$$l_{LES} = C_{des}\Delta_{max} \tag{2-24}$$

$$f_d = 1 - tanh[(A_1\gamma_d)^{A_2}] \tag{2-25}$$

where the constant C_{des} =0.032 shown by Oka and Ishihara (2009) is adopted and Δ_{max}= max$(\Delta x, \Delta y, \Delta z)$ is used as described in Fluent Theory Guide (Ansys Inc., 2011).

$$\gamma_d = \frac{\upsilon_t + \upsilon}{\kappa^2 d^2 \sqrt{U_{ij}U_{ij}}}, \quad U_{ij} = \frac{\partial \tilde{u}_i}{\partial x_j} \tag{2-26}$$

where υ_t is the kinematic eddy viscosity, υ is the molecular viscosity, $\kappa = 0.41$ is the von Kaman constant, d is the distance to the closest wall and h_{sl} is the surface layer height described below. U_{ij} is the velocity gradient. In Fluent Theory Guide (Ansys Inc., 2011), A_1 =20 proposed by Gritskevich et al. (2012) and A_2 =3 are used for the realizable $k-\varepsilon$ and SST $k-\varepsilon$ based DDES models, while A_1 =8 proposed by Spalart et al. (2006) and A_2 =3 are used for the Spalart-Allmaras based DDES model. However, the constants of A_1 in Gritskevich et al. (2012) and Spalart et al. (2006) are optimised to simulate the flow

fields around an obstacle with a thin boundary layer and it has not been validated for simulating the flow over an obstacle or a terrain immersed in a thick boundary layer, such as the atmospheric boundary layer.

In this study, the modified DDES model proposed by Ishihara and Qi (2018) is used, which introduced a piecewise function of A_1 to limit the application of RANS model in the region below the surface layer height $h_{sl} = 1m$ in real scale. As shown in the following stratification function, $A_1 = 0.2$ is used when the distance to the closest wall d is larger than h_{sl}, and the default value of $A_1 = 20$ is used if the distance d is smaller than h_{sl}.

$$A_1 = \begin{cases} 20, & d < h_s \\ 0.25, & d \geq h_s \end{cases} \tag{2-27}$$

2.3 Wind Turbine Model

2.3.1 A Coupled BEM-CFD Approach

In this study, the ADM-R model is adopted to determine the rotor-induced forces, in which the lift and drag forces acting on the turbine blades are calculated by using the blade-element theory. The relation between wind velocity and forces acting on a blade element of length dr located at radius r is shown in the Figure 2-1, where n and θ denote the axial and tangential directions respectively, α is the angle of attack, β is the local pitch angle and ψ is the angle between the relative velocity and rotor plane. dF_L and dF_D are the lift and drag forces acting on the blade element and are given by:

$$dF_L = \frac{1}{2}\rho W^2 c C_L dr \tag{2-28}$$

$$dF_D = \frac{1}{2}\rho W^2 c C_D dr \tag{2-29}$$

where c is the chord length, C_D and C_L are the lift and drag coefficients, respectively. W is the local relative velocity with respect to the blade element and is defined as

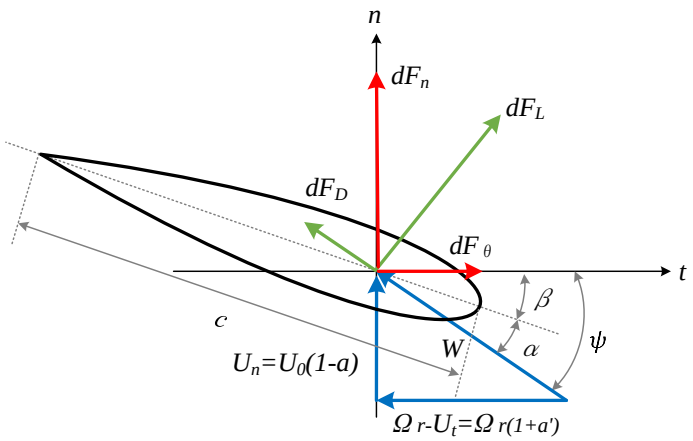

Figure 2-1 Cross-sectional blade element showing velocity and forces

$$W = \sqrt{U_n^2 + (\Omega r - U_t)^2} \tag{2-30}$$

where U_n and U_t are the axial and tangential velocities of the incident flow at the local blade element position. The resulting axial force dF_n and tangential force dF_t on blade element can be expressed as:

$$dF_n = dF_L cos\psi + dF_D sin\psi \tag{2-31}$$

$$dF_t = dF_L sin\psi - dF_D cos\psi \tag{2-32}$$

In the blade element momentum (BEM) theory (Burton et al., 2011), the axial and tangential components of the incident flow velocity at blades are assumed as $U_n = U_0(1-a)$ and $U_\theta = -\Omega r a'$ where U_0 is the free upstream wind speed, Ω is the turbine rotational speed, a and a' are the induction factors in the axial and tangential directions, respectively. They are unknown and solved based on the axial and angular momentum conservations.

In the wind farm simulation, the free upstream wind speed U_0 for a turbine in the farm is not known. Thus, the axial velocity at the rotor disk U_n and a' are selected as the unknown parameters instead of a and a' (Calaf et al., 2010; Goit and Meyers, 2015). In this study for the wake simulation in non-yawed condition, a coupled BEM-CFD method is adopted, in which U_n is directly obtained from the CFD simulation result and the local relative velocity is given as:

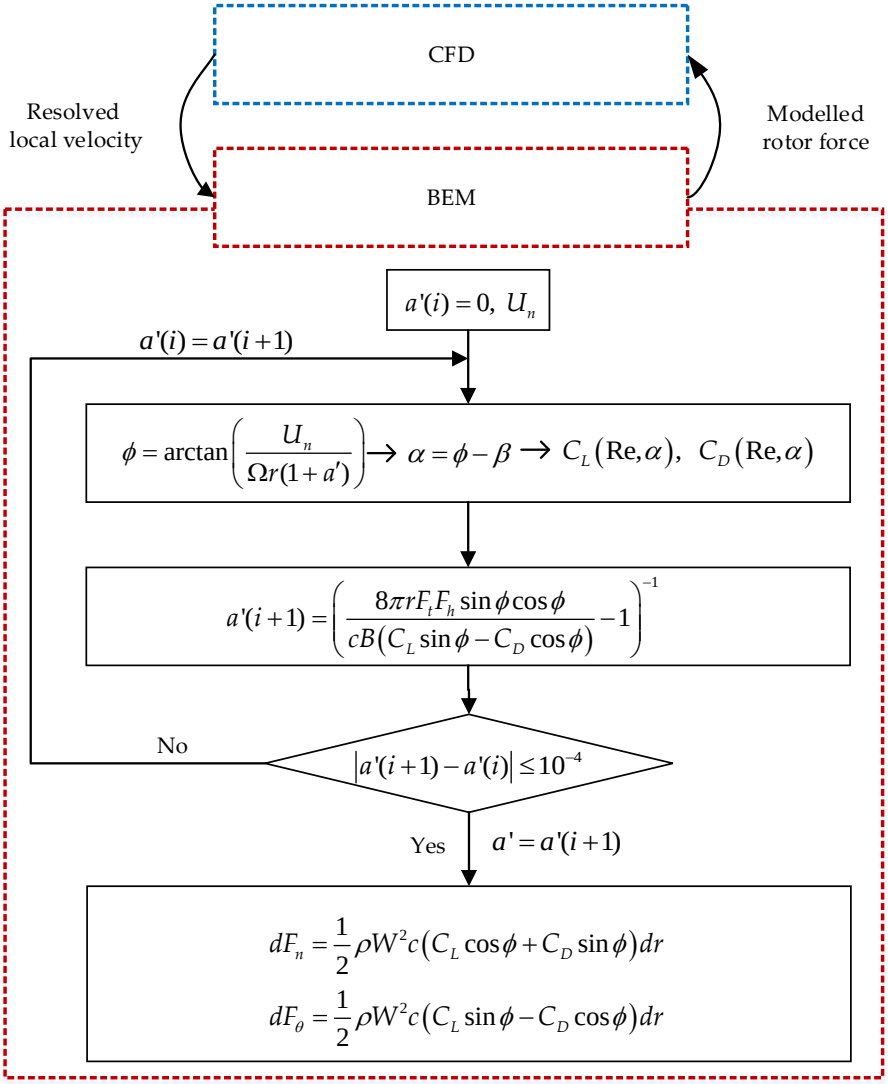

Figure 2-2 Flow chart of the coupled BEM-CFD approach

$$W=\sqrt{U_n^2+(\Omega r)^2(1+a')^2} \tag{2-33}$$

where a' is solved based on the angular momentum conservation as shown in the BEM theory:

$$a'=g_2/(1-g_2),\ g_2=\frac{Bc}{2\pi r}\frac{(C_L sin\phi-C_D cos\phi)}{4F_t F_h sin\phi cos\phi} \tag{2-34}$$

where F_t and F_h are the tip loss factor and hub loss factor and calculated by the following equations

$$F_t = \frac{2}{\pi} arccos\left[exp\left(-\frac{B}{2}\left(\frac{R}{r}-1\right)\sqrt{1+(\Omega r/U_n)^2}\right)\right] \tag{2-35}$$

$$F_h = 1.0 \tag{2-36}$$

An iterative process is used to calculate the tangential induction factors a', in which the initial value for a' is set to 0 and the convergence tolerance is specified as 1×10^{-4}. The detailed procedure of the coupled BEM-CFD approach is shown in Figure 2-2.

2.3.2 ADM-R for Yawed Wind Turbines

Figure 2-3 shows the schematic of ADM-R model in a yawed condition, where x is streamwise direction aligned with the incoming wind speed U_0 and x' is normal to the rotor plane. The yaw angle γ denotes the angle between incoming velocity U_0 and the rotor normal axial direction x'. The azimuthal angle Φ shows the position of the blade in the tangential direction and it is 0 at the top position. γ and Φ are defined positive using the right-hand rule. For the yawed rotor, the velocities and forces need some coordinate transformation when the ADM-R model is applied. The relation between wind velocity and forces acting on a blade element of length dr located at the radius r is shown in Figure 2-3. dF_L and dF_D are the lift and drag forces acting on the blade element, which is calculated by the same formula as Equation (2-28) and (2-29).

The force per unit volume in each annular with an area of $\delta A = 2\pi r\delta r$ and a thickness of $\Delta x'$ is expressed by:

$$f_n = -\frac{B}{2\pi r}\frac{dF_n}{\Delta x'\delta r} \tag{2-37}$$

$$f_t = -\frac{B}{2\pi r}\frac{dF_t}{\Delta x'\delta r} \tag{2-38}$$

where B is the number of blades.

Based on the Glauert's (Glauert, 1926) moment theory for a yawed rotor, only the normal wind flow component $U_0 cos\gamma$ is assumed to be affected by the presence of the rotor and the flow component $U_0 sin\gamma$ is left unperturbed by the rotor. The blade element

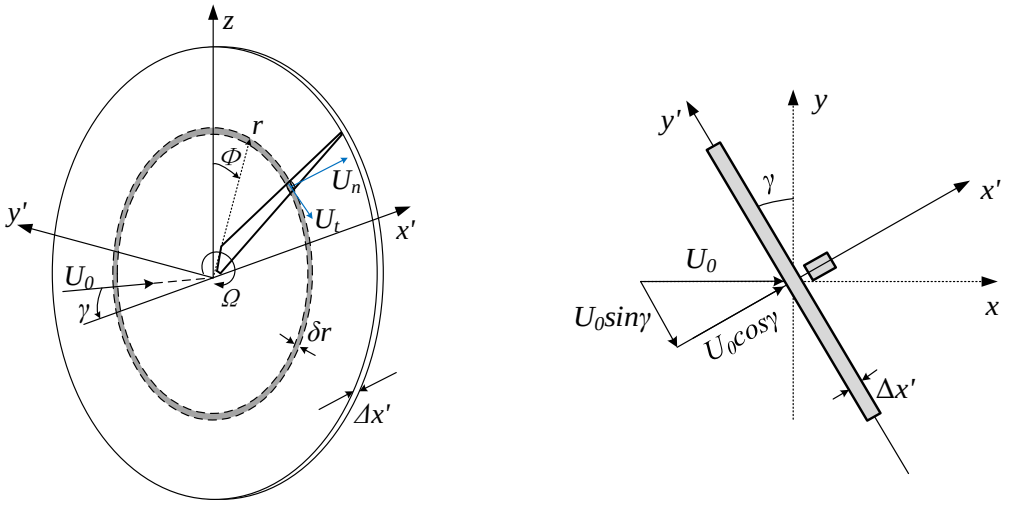

(a) isometric view (b) top view

Figure 2-3 Schematic of the ADM-R model for the yawed rotor

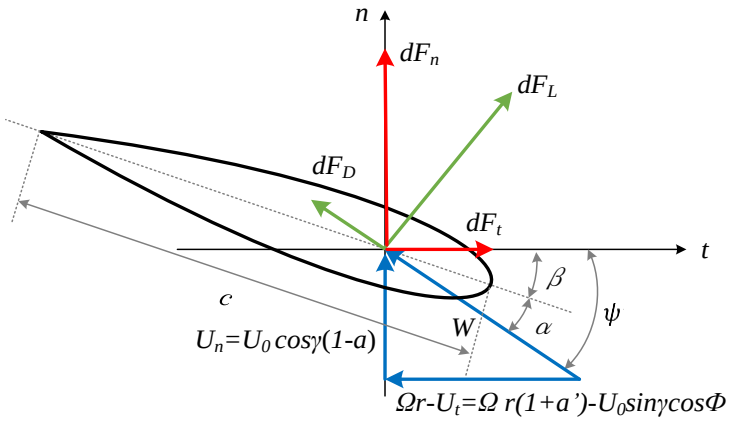

Figure 2-4 Velocities and forces acting on a cross-sectional blade element in yawed conditions

momentum (BEM) theory is still used for the yawed rotor by including the induced velocity nonuniformity correction (Burton et al., 2011; Haans, 2011). The axial and tangential components of the incident flow velocity at blades are assumed as $U_n = U_0 cos\gamma(1-a)$ and $U_t = -\Omega r a' - U_0 sin\gamma cos\Phi$, where Ω is the turbine rotational speed, a and a' are the induction factors in the axial and tangential directions, respectively. The induction factors are unknown and solved based on the axial and angular momentum conservations.

In the wind farm simulation, the free upstream wind speed U_0 for a turbine in the wake

region is not known. Thus, the axial and tangential velocity at the rotor disk U_n and U_t are selected as the unknown parameters instead of a and a' (Dörenkämper et al., 2015; Vollmer et al., 2016; Wu and Porté-Agel, 2015). In this study, a coupled approach is adopted for the ADM-R model in the yawed condition, in which U_n and U_t are directly obtained from the CFD simulation result of local velocities on the rotor disk (U_x, U_y, U_z) by using the following transformation:

$$\begin{Bmatrix} U_n \\ U_t \end{Bmatrix} = \begin{bmatrix} cos\gamma & sin\gamma & 0 \\ sin\gamma cos\Phi & -cos\gamma sin\Phi & -sin\Phi \end{bmatrix} \begin{Bmatrix} U_x \\ U_y \\ U_z \end{Bmatrix} \tag{2-39}$$

The axial and tangential forces (f_n, f_t) are calculated by using the above local velocities on the rotor disk (U_n, U_t) and then distributed through the following transformation.

$$\begin{Bmatrix} f_x \\ f_y \\ f_z \end{Bmatrix} = \begin{bmatrix} cos\gamma & sin\gamma cos\Phi \\ sin\gamma & -cos\gamma cos\Phi \\ 0 & -sin\Phi \end{bmatrix} \begin{Bmatrix} f_n \\ f_t \end{Bmatrix} \tag{2-40}$$

where, (f_x, f_y, f_z) is the source term in Equation (2-2) for each direction to present the effects of the turbine rotor on the momentum. The rotor can be rotated around the z axis enabling the yaw angle configuration.

2.3.3 Nacell and tower modelling

In general, for a utility-scale wind turbine, the nacelle and tower effects are quite small compared with the rotor, which can be neglectable if one focus on the far wake regions. In some of the prior study (Wu and Porté-Agel, 2011; Xie and Archer, 2014), the effects of nacelle and tower are also simplified as a permeable disk, in which the nacelle-induced drag force acting upon the incoming flow is parameterized using a formulation similar to the ADM-NR:

$$f_x = -\frac{1}{2}\rho C_{D,na} U_0^2 \tag{2-41}$$

where $C_{D,nac}$ is the drag efficient of the nacelle. While for a downscale wind turbine model in the wind tunnel test, due to some limitations of fabrication process, the relative size of

nacelle and tower regards to the rotor are normally larger than that in real situation. Thus, the above simplified model may underestimate the nacelle and tower effects. In this thesis, the nacelle and tower are modelled as porous media with 99.9% packing density. The forces induced by the nacelle and tower are calculated as follows:

$$f_{nt,i} = -\frac{1}{2}\rho C_{D,i}|u_i|u_i \tag{2-42}$$

where u_i is the local velocity inside the nacelle and tower and should be close to 0. Thus, the drag coefficient $C_{D,i}$ is set to 1×10^5 in the CFD simulation.

2.4 Roughness Model

2.4.1 Wall Function

The logarithmic law, which is shown as Equation (2-43), is widely used in the wind engineering to describe the mean wind profile in the atmospheric boundary layer (ABL) (Blocken et al., 2007; Grimmond et al., 1999; Xian et al., 2002).

$$U(z) = \frac{u_*}{\kappa} ln\left(\frac{z}{z_0}\right) \tag{2-43}$$

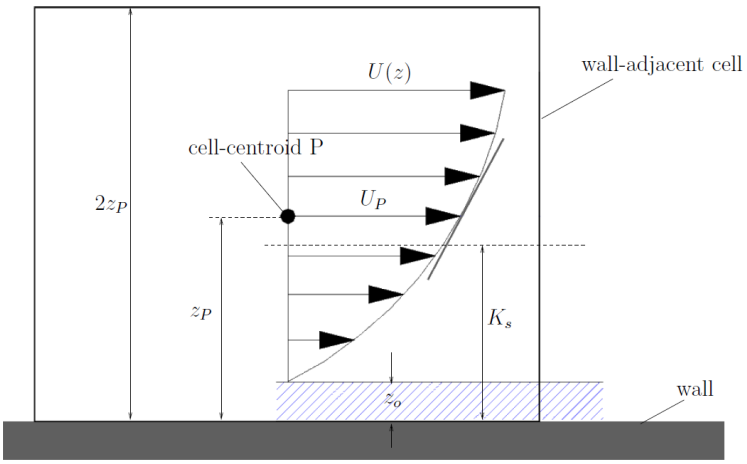

Figure 2-5 Wall-adjacent cell requirements (Ansys Inc., 2011)

where the u_* is known as the shear velocity or friction velocity. κ is the Karman constant. z is the height above the surface. z_0 is roughness length and defined as the height above the surface at which the mean wind velocity assumes a zero value. Wind profiles should be different if site conditions changes, therefore appropriate z_0 should be specified to account for different roughness surface. Table 2-1 lists land-use categories and roughness length provided by the Ministry of Land, Infrastructure, Transport and Tourism of Japan (MLIT).

In the computation fluid computation, wall function is used to describe near wall boundary layer, as shown in the following equations:

$$\begin{cases} U^* = y* & y* < 11.225, laminar flow \\ U^* = \frac{1}{\kappa} ln(y*) + B - \Delta B & y* > 11.225, turbulent\ flow \end{cases} \quad (2\text{-}44)$$

where $U^* = U/u_*$ is normalized velocity and $y^* = \rho u_* z/\mu$ is normalized distance from the wall. $B = 1/\kappa \cdot \ln E$ is an empirical constant corresponding to smooth flat plate. E=9.793 is an empirical constant. ΔB accounts for displacement of normalized wind velocity profile caused by rough wall and should be modeled. There are two models are widely used, roughness length model and sand-grain roughness model, and Figure 2-5 shows the schematic of the roughness model application in the wall-adjacent cell.

Table 2-1 Land-use categories and corresponding roughness length Z_0

Category	z_0 (m)	Category	z_0 (m)
Rice Field	0.03	Transportation Area	0.1
Field	0.1	Other Area	0.03
Orchard	0.2	Lakes and Ponds	0.0002
Other Wood Field	0.1	River A	0.001
Forest	0.8	River B	0.001
Wasteland	0.03	Beach	0.03
High Buildings	1.0	Sea	0.0002
Low Buildings	0.4		

The roughness length model applies roughness length z_0. ΔB can be calculated by Equation (2-49). The shear stress modeled in the two horizontal momentum Equations of the wall-adjacent cell is given in Equation

$$\Delta B = \frac{1}{\kappa} ln\left(E \frac{\rho u_* z_0}{\mu}\right) \tag{2-45}$$

$$\tau_w = \rho \cdot \frac{\kappa U_P}{ln(z_P/z_0)} \cdot C_\mu^{1/4} k_P^{1/2} \tag{2-46}$$

where ρ is air density. U_P, k_P and z_P are mean wind velocity, turbulent kinetic energy and height of cell center of the wall-adjacent cell respectively (see Figure 2-5). C_μ is parameter and was discussed in section 2.1.1. The generation and dissipation rate of turbulent kinetic energy in the wall-adjacent cell are calculated by Equation (2-47) and Equation (2-48).

$$G_k = \frac{\tau_w^2}{\kappa \rho C_\mu^{1/4} k_P^{1/2} z_P} \cdot \frac{1}{2} ln\left(\frac{2z_P}{z_0}\right) \tag{2-47}$$

$$\varepsilon_P = \frac{C_\mu^{3/4} k_P^{3/2}}{\kappa z_P} \cdot \frac{1}{2} ln\left(\frac{2z_P}{z_0}\right) \tag{2-48}$$

Similarly, the sand-grain roughness model applies physical roughness height K_s. The roughness regime is subdivided into three regimes as shown in Equation (2-49) (Ansys Inc., 2011).

$$\Delta B = \begin{cases} 0 & K_s^+ \le 2.25 \\ \frac{1}{\kappa} ln\left[\frac{K_s^+ - 2.25}{87.75} + C_s K_s^+\right] \times sin\{0.4258(lnK_s^+ - 0.811)\} & 2.25 < K_s^+ \le 90 \\ \frac{1}{\kappa} ln(1 + C_s K_s^+) & K_s^+ > 90 \end{cases} \tag{2-49}$$

where $K_s^+ = \rho u_* K_s / \mu$ is the nondimensional roughness height and C_s is a roughness constant. The shear stress in the sand-grain roughness model is the same as Equation (2-46). The generation and dissipation rate of turbulent kinetic energy in the wall-adjacent cell are

calculated by Equation (2-50) and Equation (2-51).

$$G_k = \frac{\tau_w^2}{\kappa\rho C_\mu^{1/4} k_P^{1/2} z_P} \tag{2-50}$$

$$\varepsilon_P = \frac{C_\mu^{3/4} k_P^{3/2}}{\kappa z_P} \tag{2-51}$$

It's easy to see that the generation and dissipation rate of turbulent kinetic energy in the wall-adjacent cell are the same for two models if the height of wall-adjacent cell chosen as $7.4z_0$. What's more, a relationship between z_0 and K_s can be obtained by comparing Equation (2-52) and the logarithmic regime in Equation (2-49).

$$K_s = \frac{E}{C_s} z_0 \tag{2-52}$$

Where E=9.793 is an empirical constant and C_s is set as 0.5 in present study.

2.4.2 Canopy Model

The definition of canopy layer is the assemblage of obstacles near the ground like buildings and trees and spaces between them. Canopy model, in contrast of the rigid wall approach, consider the effect of obstacles as external force reacting on the air.

In the momentum Equation (2-2), source term $f_{\tilde{u},i}$ is introduced to model external force by obstacles such as buildings, tree or mixed canopy region. In this study, the canopy model proposed by (Enoki and Ishihara, 2012) is used, which can consider the effect of the vegetation and solid buildings simultaneously.

$$f_{\tilde{u},i} = -\frac{1}{2}\rho C_f \frac{\gamma_0}{l_0} |\tilde{u}| \tilde{u}_i \tag{2-53}$$

Where $f_{\tilde{u},i}$ is external force per unit volume. C_f is the equivalent drag coefficient, and γ_0 is packing density and l_0 is defined as the representative length scale of obstacles.

(Enoki and Ishihara, 2012) provide value of C_f, γ_0, l_0 as well as canopy height, H corresponding to roughness length z_0 for very rough surface such as buildings and tree.

Parameters transformation is list in Table 2-1.

In case digital map of buildings is available, detailed shape and height of buildings can be obtained. C_f, γ_0 and l_0 can be calculated by the following equations:

$$C_f = \frac{1}{(1-\gamma_0)^3} min\left[\frac{1.53}{1-\gamma_0}, 2.75(1-\gamma_0)\right] \tag{2-54}$$

$$\gamma_0 = \frac{V_u}{V_{grid}} \tag{2-55}$$

$$l_0 = \frac{V_u}{S_u/4} \tag{2-56}$$

where V_{grid} is volume of local computational cell, in which the volume of V_u is occupied by buildings. S_u is the sum of side area of total occupied buildings.

The source terms in k and ε Equations are introduced to consider the generation and dissipation of turbulence by canopy layer. (Yamaguchi, Enoki et al., 2009, Enoki and Ishihara, 2012) developed a generalized canopy model which can consider the buildings and trees simultaneously. In this generalized canopy model, equivalent drag coefficient C_f is corresponding for drag coefficient C_d. Parameters γ_0 and l_0 are introduced instead of using $A(z)$ only so that it is also capable to considering buildings. Additional parameters, β_p, β_d, $C_{p\varepsilon 1}$ and $C_{p\varepsilon 2}$, are also introduced to make this model suitable for both low and high density case. In high density case, it assumes the generation and dissipation of turbulence achieves a balanced state. The generalized canopy model in k and ε Equation are shown in the following equations:

$$S_k = \frac{1}{2}\beta_p \rho C_f \frac{\gamma_0}{l_0}|\tilde{u}|^3 - \frac{1}{2}\beta_d \rho C_f \frac{\gamma_0}{l_0}|\tilde{u}|\tilde{k} \tag{2-57}$$

$$S_\varepsilon = \frac{1}{2}C_{p\varepsilon 1}\beta_p \rho \frac{\tilde{\varepsilon}}{\tilde{k}} C_f \frac{\gamma_0}{l_0}|\tilde{u}|^3 - \frac{1}{2}C_{p\varepsilon 2}\beta_d \rho C_f \frac{\gamma_0}{l_0}|\tilde{u}|\tilde{\varepsilon} \tag{2-58}$$

where $|\tilde{u}| = \sqrt{\tilde{u}_i \tilde{u}_i}/2$ is the magnitude of wind velocity. C_f, γ_0 and l_0 are basic canopy parameters, and calculation of these parameters are given by (Enoki and Ishihara, 2012). β_p, β_d, $C_{p\varepsilon 1}$ and $C_{p\varepsilon 2}$ are additional canopy parameters, whose value are calibrated by experimental results.

Table 2-2 Canopy parameters corresponding to roughness length z_0

Category	Original z_0 (m)	Modified z_0 (m)	C_f	γ_0	l_0 (m)	H (m)
Orchard	0.2	0.03	0.4	0.001	0.01	3.3
Forest	0.8	0.03	0.4	0.001	0.01	13.3
High Buildings	1.0	0.03	3	0.155	39.4	11.4
Low Buildings	0.4	0.03	2.88	0.146	38.1	5.18

2.5 Summary

In this Chapter, the mathematical model utilized in this thesis for the numerical simulation are illustrated.

1. the three turbulence models including RSM, LES, and a modified DDES are introduced. Due to the fact that a large fraction of the turbulence is resolved, LES can obtain the instantaneous flow information and has become a popular tool for the turbulent flow simulation. In this thesis, the LES is adopted to reproduced the turbulent boundary layer generated by spires and fences in the wind tunnel, and then to investigate the wake characteristics in various conditions. Then for the wake simulation in yawed condition, a wider computational domain is necessary due to the wake deflection in horizontal direction. Hence, in order to save the computational cost, RSM is selected, where the turbulent inflow extracted from the prior LES is used as the inlet to avoid the larger number of grid for more spires and fences in wider numerical wind tunnel. Considering LES is relative expensive for the application in real wind farm over complex terrain, a modified DDES model which use RANS near the surface and LES in the higher part is preferred.

2. A coupled BEM-CFD approach to parameterize the rotor induced forces based on the local disk velocity is developed. The procedure of this approach in CFD simulation is implemented by the code written as User Defined Function (UDF) in Fluent.

3. The methodology for modelling the surface roughness are presented. The wall function is applied for the areas with low roughness length ($z0 < 0.03m$), while the very rough surface such as buildings and tree are considered by the canopy model.

Chapter3. NUMERICAL STUDY FOR WIND TURBINE WAKE

3.1 Introduction

In this Chapter, systematical numerical simulations are performed to study the wind turbine wake characteristics under various conditions. Firstly, two kinds of operating condition with different thrust coefficients under two types of inflow with different ambient turbulence intensity are simulated for a model and a utility-scale wind turbine by using large eddy simulation (LES). The predicted mean velocity and turbulence intensity in the wakes of two wind turbines are compared with those obtained from the wind tunnel tests to validate numerical models. Subsequently, eight simulations by the Reynolds Stress Model are conducted for different thrust coefficients, yaw angles and ambient turbulence intensities. The wake deflection, mean velocity and turbulence intensity in the wakes are systematically investigated. Finally, conclusions of this chapter are summarized in section 3.4.

3.2 Wake of Non-Yawed Wind Turbine

In this section, LES is employed to simulate the wind turbine wake flows under non-yawed conditions, in which the governing Equations are presented in section 2.1.2. Firstly, the accuracy of the wind turbine model is validated in section 3.2.1 by comparing the calculated thrust coefficients with the measured data of a model and a utility-scale wind turbine, respectively. Section 3.2.3 describes the set-up of the numerical simulations,

including the computational domain and the main parameters used in each case. The turbulent inflows generated in the numerical wind tunnel are validated in section 3.2.3. Finally, the characteristics of the mean velocity and turbulence intensity in the wake region under different conditions are investigated and validated by the wind tunnel test in section 3.2.4 and 3.2.5, respectively.

3.2.1 Wind Turbine Model

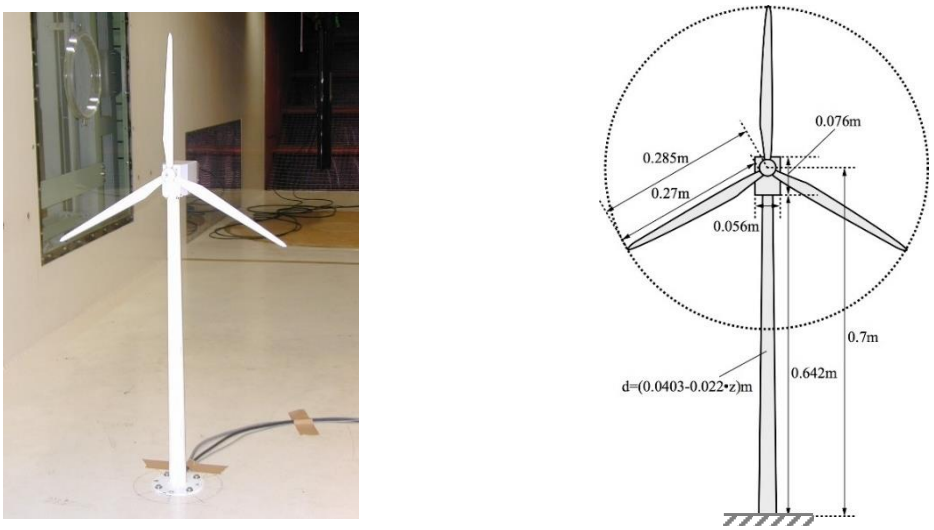

Figure 3-1 1/100 scale model wind turbine in the wind tunnel test and its dimensions

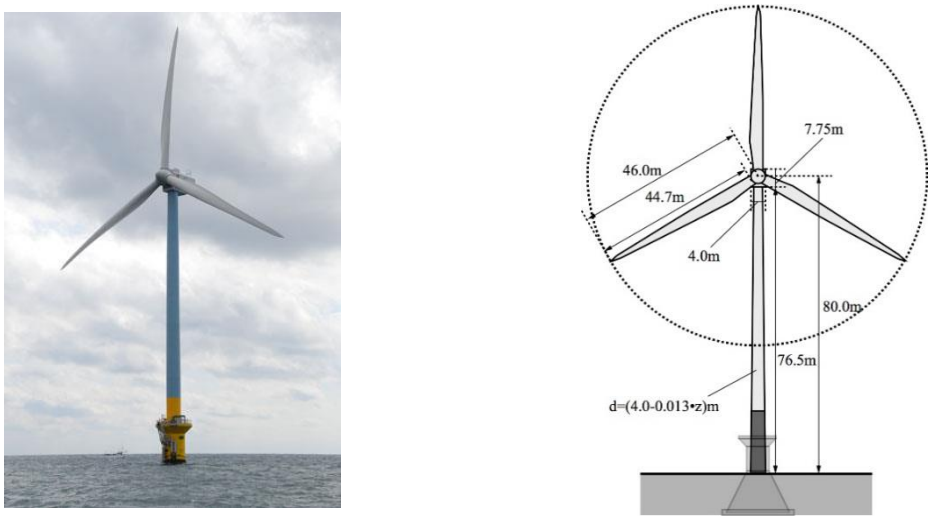

Figure 3-2 2.4MW wind turbine at Choshi demonstration site and its dimensions

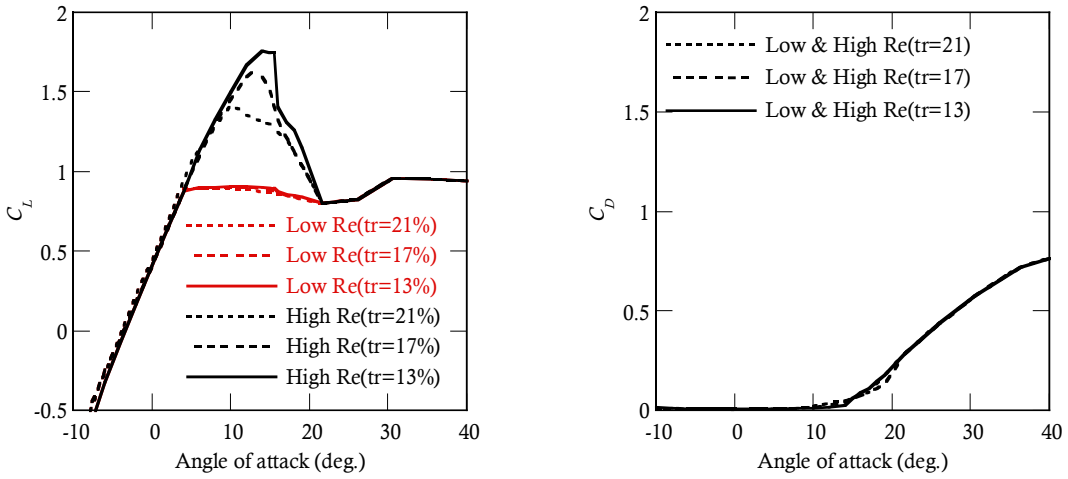

(a) Lift force coefficient (b) Drag force coefficient

Figure 3-3 Variation of airfoil aerodynamic coefficients with the attack angle

In this study, a model wind turbine in the wind tunnel test and a utility-scale wind turbine are considered. The model wind turbine is a 1/100 scale model of Mitsubishi's MWT-1000 and was used in the wind tunnel test by Ishihara et al. (Ishihara et al., 2004) (see Figure 3-1). The utility-scale wind turbine model is based on the offshore 2.4MW wind turbine at the Choshi demonstration site, Japan (see **Figure 3-2**).

The aerodynamic characteristics of the airfoils datasets of the sample 2MW offshore wind turbine model provided by GL Garrad Hassan (Bossanyi, 2003) are used for the 2.4MW utility-scale turbine, and the corresponding Reynolds number is 2×10^6. On the other hand, the Reynolds number for the airfoils of the model turbine in the wind tunnel test is around 5×10^4.Therefore, the lift force coefficients are modified based on the NACA0012 provided by Burton et al. (Burton et al., 2011) to reproduce the low Reynolds number effect. The drag force coefficients of the blade are not sensitive to the Reynolds number so the data for the sample 2MW offshore wind turbine are used. The aerodynamic force coefficients for each section of the blade are plotted for low (5×10^4) and high Reynolds number (2×10^6) in Figure 3-3, in which the '*tr*' denotes the blade thickness ratio.

The thrust coefficients of whole rotor are calculated under different tip speed ratios as shown in Figure 3-4 to validate the accuracy of the adopted aerodynamics coefficients for the blades. It can be seen that the predicted thrust coefficients show good agreement with

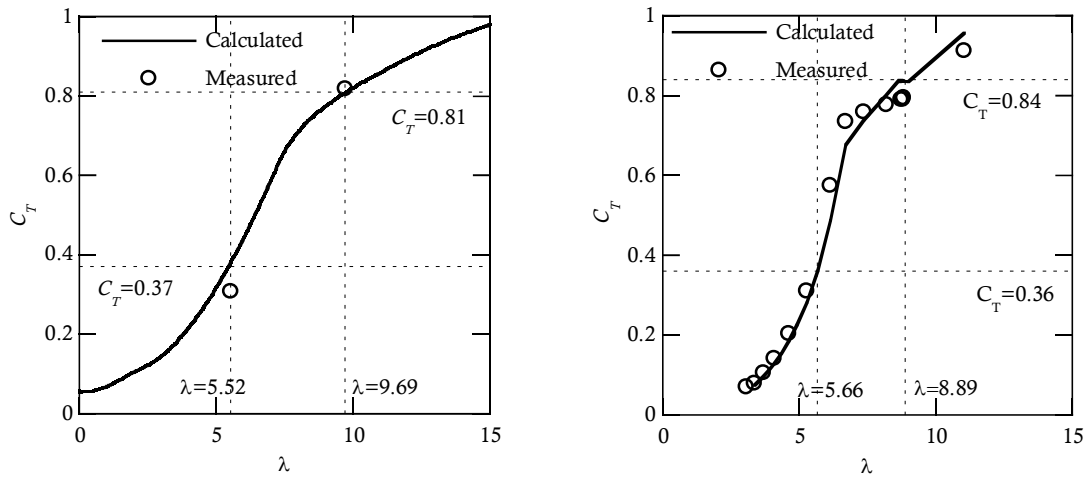

(a) Model wind turbine (b) Utility-scale wind turbine

Figure 3-4 Variation of the thrust coefficient with tip speed ratio of (a) model wind turbine and (b) utility-scale wind turbine

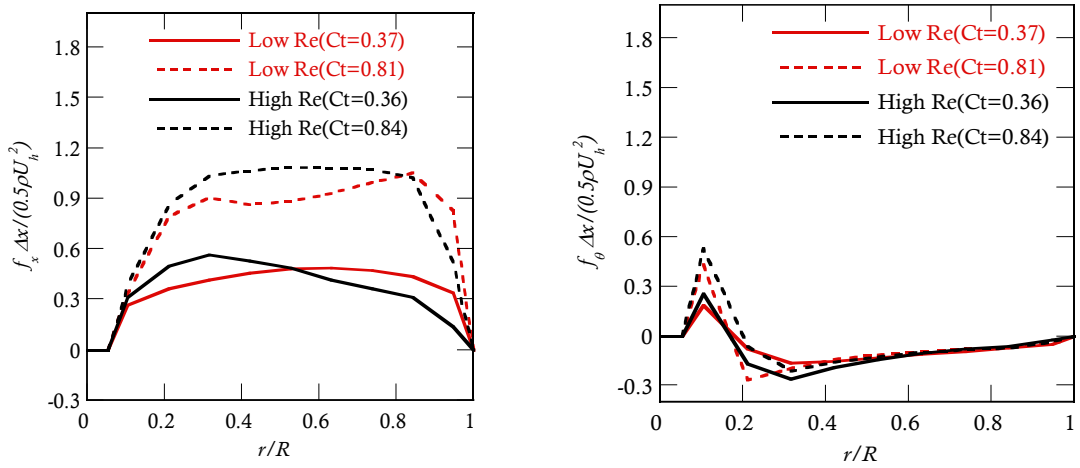

(a) Axial direction (b) Tangential direction

Figure 3-5 Radial distribution of rotor load calculated by BEM theory: (a) axial direction, (b) tangential direction

the measured data from the wind tunnel and field experiments for the model and utility scale wind turbine, respectively.

The load distributions on the blade under different thrust coefficients are presented in Figure 3-5, in which the forces on the rotor disk calculated by Equation (2-31) and Equation (2-32) are multiplied by the rotor width and normalized by $0.5\rho U_h^2$. It can be seen that when

the rotor thrust coefficient has similar values, the distribution of the resulting axial and tangential forces along the rotor is analogous. The behaviour of the wake is insensitive for the Reynolds number of a blade as mentioned by Whale et al. (2000). The small difference on the load distribution does not cause distinct effects on the wake flow. This implies that effects of Reynolds number and blade details are not obvious on the wake flows of wind turbines as shown in section 3.2.4 and 3.2.5.

3.2.2 Numerical Setup

Numerical simulations are conducted in the atmospheric boundary layer simulated by using the same spires and fence as the wind tunnel test of Ishihara et al. (2004). As shown in Figure 3-6(a), the computational domain has a streamwise length of 18.5m, a spanwise length of 1.5 m and a vertical height of 1.8 m. The wind turbine model shown in Figure 3-6(b) is placed at a distance of 5.5 m from the fence and at the center in the spanwise direction. The rotor diameter D is 0.57 m and the hub height H is 0.7 m.

Boundary conditions used in the numerical simulations are summarized in Table 3-1. A stress-free condition ($\partial u/\partial n = 0,\ \partial v/\partial n = 0,\ w = 0$) was used at the top of the domain and a symmetry condition ($\partial u/\partial n = 0,\ \partial w/\partial n = 0,\ v = 0$) at the spanwise sides. Uniform wind flow with a speed of 10m/s was set at the inlet ($p = 0,\ u = 10$ m/s, v=0, w=0), which follows the wind tunnel experiment. At the end of the tunnel, outflow condition is applied ($\partial p/\partial n = 0,\ \partial u/\partial n = 0,\ \partial v/\partial n = 0,\ \partial w/\partial n = 0$). The no-slip wall boundary condition is used for the bottom of the wind tunnel and the surface of spires and fence. For the wall-adjacent cells, the wall shear stresses are obtained from the laminar stress-strain relationship in laminar sublayer:

$$\frac{\tilde{\mu}}{\mu_\tau} = \frac{\rho \mu_\tau y}{\mu} \tag{3-1}$$

Provided that the mesh cannot resolve the laminar sublayer, the centroid of the wall-adjacent cells is assumed to fall within the logarithmic region of the boundary layer, and then the law of the wall is employed as follows:

$$\frac{\tilde{\mu}}{\mu_\tau} = \frac{1}{\kappa} lnE\left(\frac{\rho \mu_\tau y}{\mu}\right) \tag{3-2}$$

where $\tilde{\mu}$ is the filtered velocity tangential to the wall, y is the distance between the center of the cell and the wall, $\mu_\tau$is friction velocity, and the constant E is 9.793.

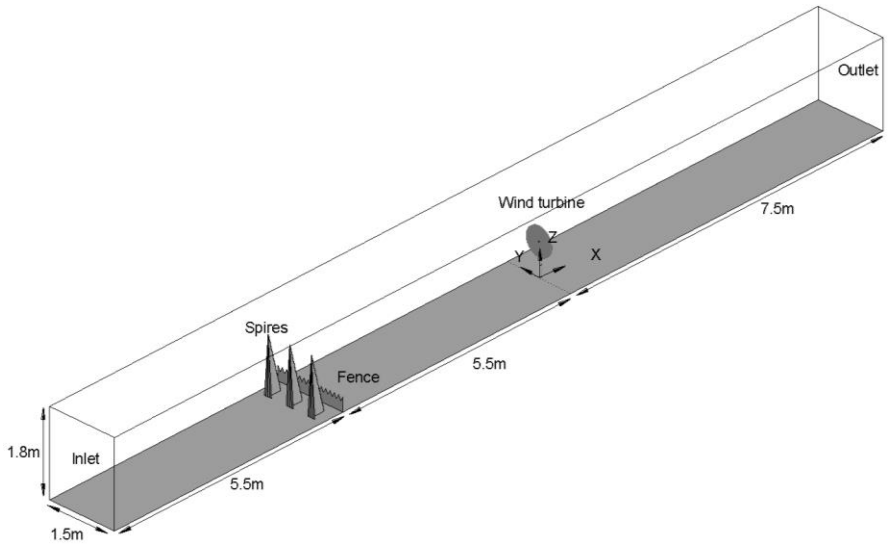

Figure 3-6 Schematic of the computational domain

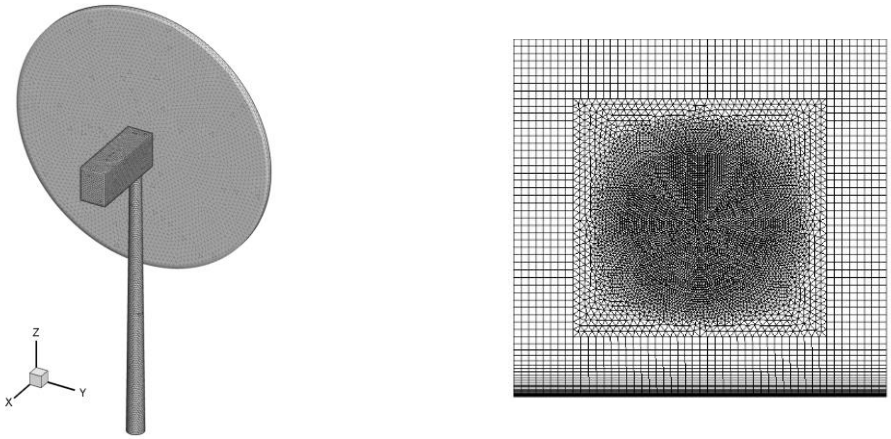

(a) Mesh of wind turbine model (b) Mesh at the rotor section

Figure 3-7 Schematic of the wind turbine model in CFD simulation

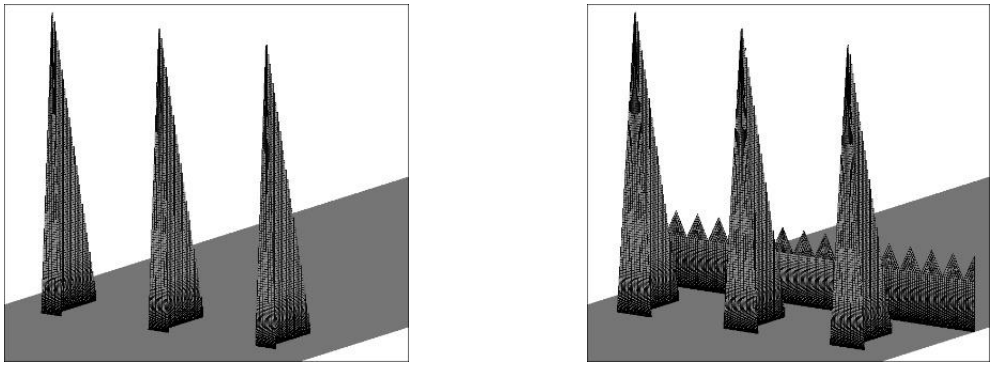

(a) Low turbulence inflow (b) High turbulence inflow

Figure 3-8 Schematic of grid used in the numerical simulation for spires and fence

Table 3-1 Boundary conditions

Boundary	Setting
Inlet Boundary	Velocity inlet
Outlet Boundary	Outflow
Side Boundary	Symmetry
Top Boundary	Stress-free
Bottom Boundary	Log law

Table 3-2 Parameters of numerical simulation

Case	WT-Type	C_T	I_a	Re	Tip speed ratio λ	Pitch Angle (deg.)
1	WT-M	0.37	0.035	5×10^4	5.52	0
2	WT-M	0.81	0.035	5×10^4	9.69	0
3	WT-M	0.37	0.137	5×10^4	5.52	0
4	WT-M	0.81	0.137	5×10^4	9.69	0
5	WT-P	0.36	0.035	2×10^6	5.66	7.4
6	WT-P	0.84	0.035	2×10^6	8.89	0
7	WT-P	0.36	0.137	2×10^6	5.66	7.4
8	WT-P	0.84	0.137	2×10^6	8.89	0

The rotor disk, nacelle and tower as shown in Figure 3-7 (a) are divided in a uniform distance of 0.01m by tetrahedral mesh. The turbine rotor is connected smoothly with the outside domain as shown in Figure 3-7 (b), where the front surface of the rotor is located at $x=0$. The low turbulence flow is generated by using the spires as shown in Figure 3-8

(a) and the high turbulence flow is generated by using the combination of wider spires and fence as shown in Figure 3-8 (b). The minimum grid size for the spires and fence in vertical and horizontal direction are set to 0.01m and 0.002m, respectively.

It should be noted that the wake simulations for utility-scale turbine are also done in the wind tunnel scale since the wake flow behavior itself is insensitive to the Reynolds number when it is larger than 1×10^3 (Sørensen et al., 1998). In actuator disc simulation, the Reynolds number effects from the blade aerodynamics are taken into account by the drag and lift coefficients as shown in Figure 3-3.

Two kinds of operating condition ($C_T \approx 0.35$ and $C_T \approx 0.8$) under two types of inflow with different ambient turbulence intensity ($I_a = 0.035$ and $I_a = 0.137$) are used for the model and utility-scale wind turbines, respectively. For the model wind turbine, the tip speed ratio is set the same as the wind tunnel test. The parameters of numerical simulation for each case are summarized in Table 3-2, in which I_a is the ambient turbulence intensity at the hub height, C_T is the thrust coefficient and is defined as:

$$C_T = \frac{T}{0.5\rho U_h^2 A_D} \tag{3-3}$$

where A_D is the area of the rotor disk, T is the thrust force acting on the rotor and U_h is the hub height mean velocity. WT-M and WT-P denote the turbine model used in the wind tunnel test and the utility-scale turbine used at the Choshi demonstration site, respectively.

Finite volume method is employed in this study and the simulations are performed with ANSYS FLUENT. The second order central difference scheme is used for the convective and viscosity term, and the second implicit scheme is adopted for the unsteady term. SIMPLE (semi-implicit pressure linked Equations) algorithm is employed for solving the discretized Equations (Ferziger and Perić, 2002)..

3.2.3 Inflow

The atmosphere boundary layers without wind turbine are generated by the spire and fence. The mean velocities at the hub height with the low and high turbulence intensity are

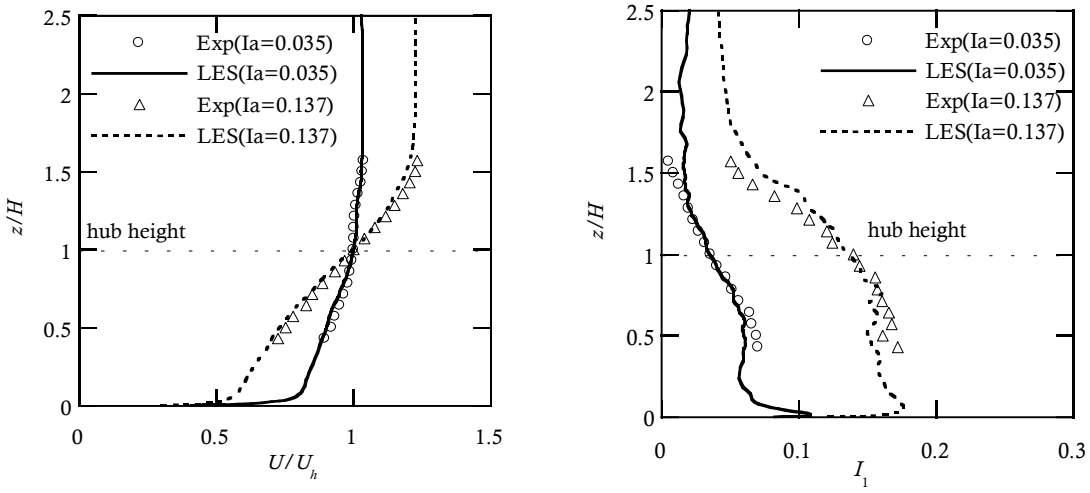

(a) Mean velocity (b) Turbulence intensity

Figure 3-9 Vertical profiles in turbulence boundary layers without wind turbine

10.22m/s and 10.24m/s, respectively, which are close to each other. All the profiles of mean velocity in this study are normalized by U_h=10.2m/s. The turbulence intensity is defined as:

$$I_1 = \frac{\sigma_u}{U_h} \tag{3-4}$$

where σ_u is turbulence standard deviation. The ambient turbulence intensities at the hub height are $I_a = 0.035$ and $I_a = 0.137$ for low and high turbulence conditions, respectively. As shown in Figure 3-9, the vertical mean velocity and turbulence intensity profiles at the location of the turbine ($x = 0, y = 0$) show good agreement with the experiment data.

3.2.4 Mean Velocity in the Wake Flow

The characteristics of mean velocity in the wake region are shown in Figure 3-10 and Figure 3-11. The two-dimensional contours from the model turbine cases (WT-M) are displayed in the vertical x-z plane through the center of the turbine ($y = 0$) as well as in the horizontal x-y plane at hub height ($z = H$). The predicted vertical and horizontal profiles at selected downwind locations of $x = 2D, 4D, 6D$ and $8D$ are also plotted to illustrate the quantitative comparison between simulation results and the experiment data. Black solid

lines and dash lines denote the results for the model wind turbine (WT-M) and the utility-scale wind turbine (WT-P), respectively. The experiment data are shown by open circles at two positions of $x = 2D, 8D$. All the velocities are normalized by the hub height mean velocity U_h. The x-axis denotes the distance from the wind turbine normalized by the rotor diameter D. The distance of $2D$ corresponds to a unit scale of normalized mean velocity U/U_h in Figure 3-10 and Figure 3-11.

As shown in Figure 3-10 (a)~(d) and Figure 3-11 (a)~(d), mean velocities in the wake region show significant differences with different ambient turbulence intensity and thrust coefficients. It can be seen that high ambient turbulence intensity (Case 1, 2, 5, 6) leads to shorter wake region than cases with the low ambient turbulence (Case 3, 4, 7, 8). The high turbulence accelerates the process of flow mixing in the wake region. In addition, the large thrust coefficient cases (Case 2, 4, 6, 8) induces stronger velocity deficit in the wake region than the cases with small thrust coefficient (Case 1, 3, 5, 7). In Figure 3-11 (a)~(d), the horizontal profiles show axial symmetric and some asymmetry in near wake region is due to the effect of torque on the rotor.

The LES simulation results of both model and utility-scale wind turbine trend towards the experimental data, even though the velocity deficits are slightly underestimated in the near wake region (x=2D) for the low turbulence cases (Case1, 2, 5 and 6). As mentioned in the introduction, the near wake flow is significantly affected by the specific blade aerodynamics when the ambient turbulence is small. The ADM-R model is difficult to consider all detailed information for the blades. On the other hand, for the high ambient turbulence cases (Case 3, 4, 7 and 8), the velocity deficits in the near wake region are well predicted, since larger ambient turbulence generates stronger flow mixing and makes the effect from the blades less obvious.

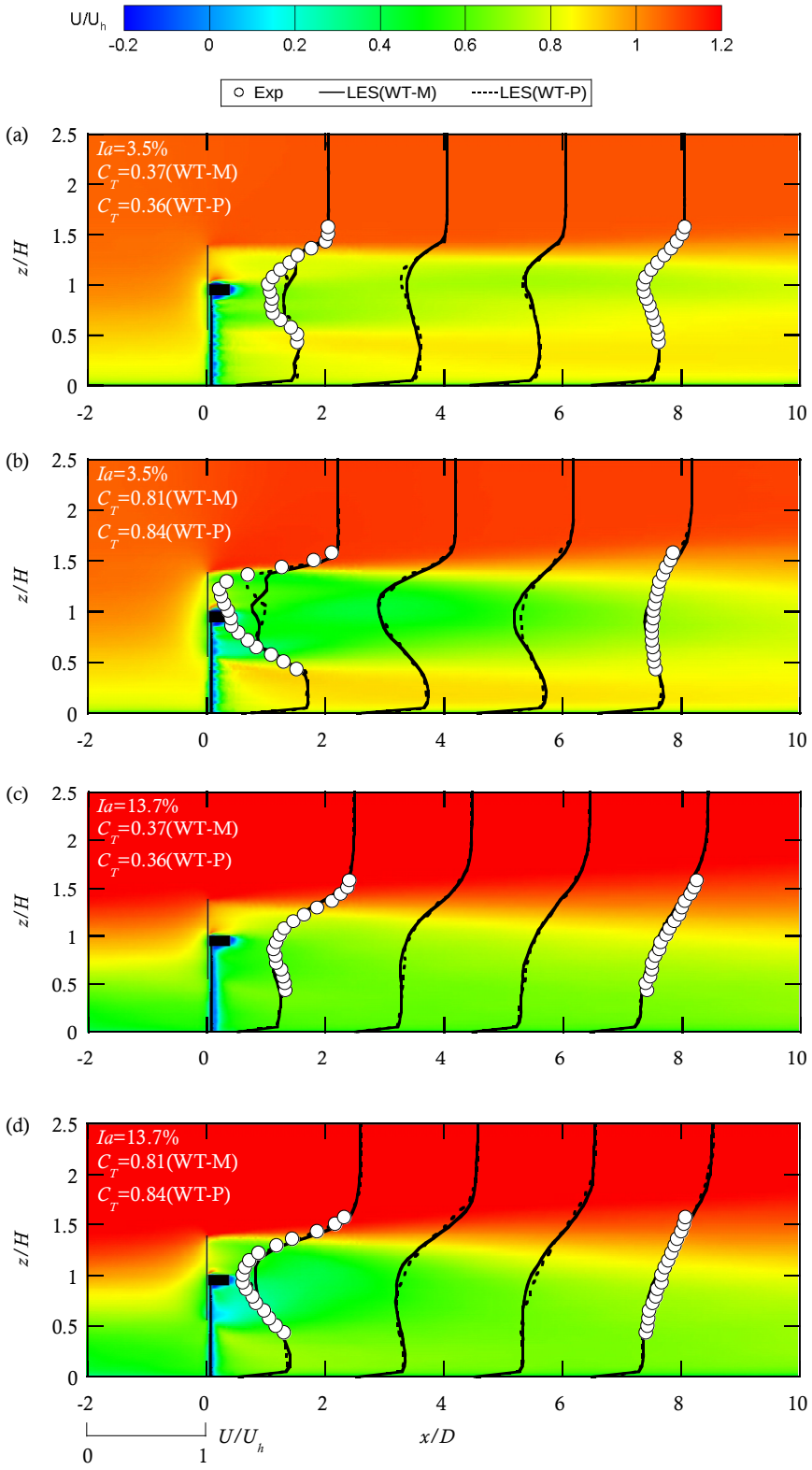

Figure 3-10 Mean velocity profiles and contours in vertical $x-z$ plane through the center of the rotor

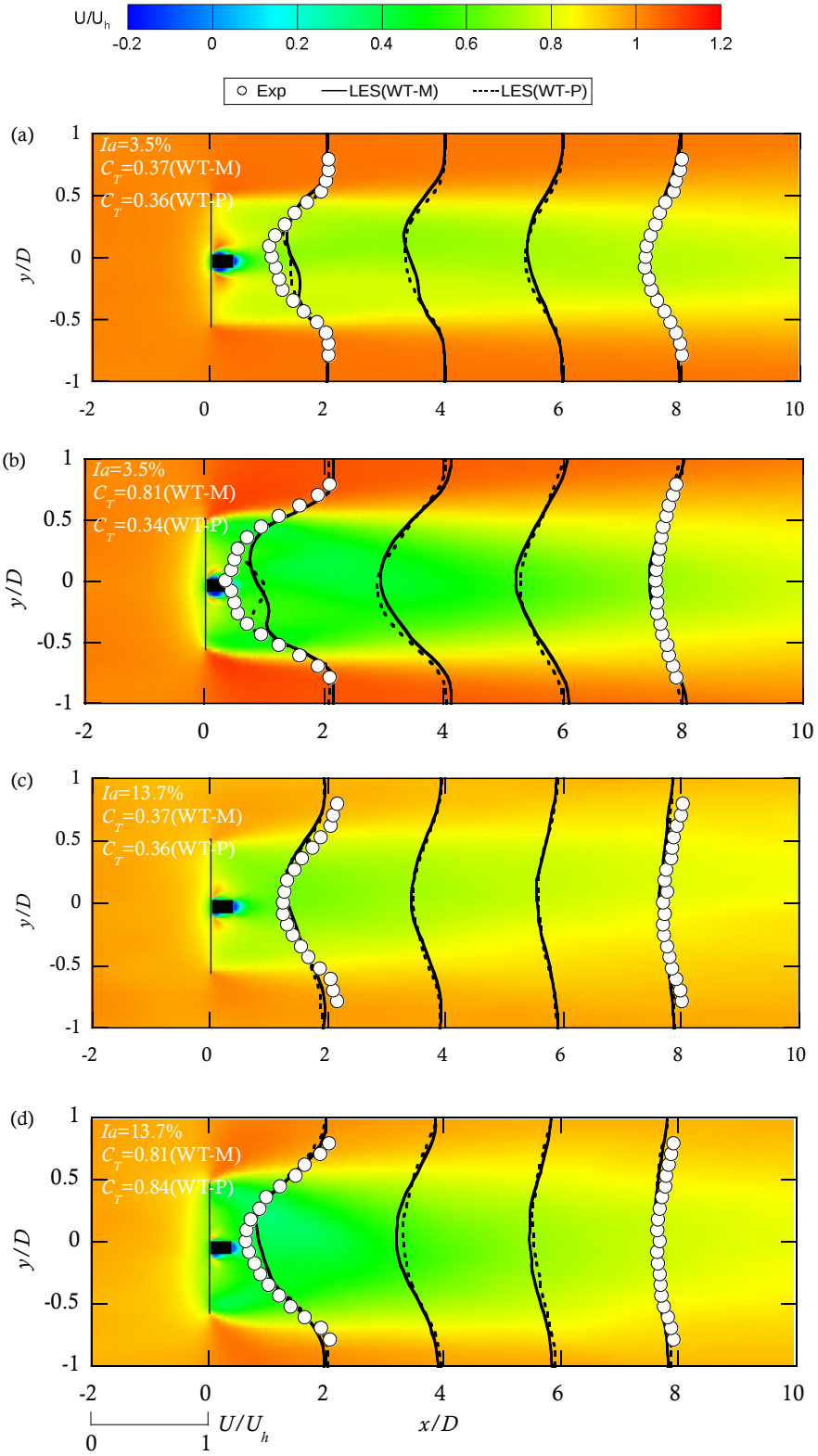

Figure 3-11 Mean velocity profiles and contours in the horizontal $x-y$ plane at the hub height.

3.2.5 Turbulence Intensity in the Wake Flow

The characteristics of and turbulence intensity in the wake region are shown in Figure 3-12 and Figure 3-13 for vertical and horizontal directions, respectively. The distance of $2D$ corresponds to a scale of turbulence intensity with the value of 0.3.

Figure 3-12 (a)~(d) reveal that an obvious enhancement of turbulence occurs in the upper half of the wake region, especially at the top tip height. This enhancement is related to the wind shear that is the sharp shape of mean velocity profile near the top tip as shown in Figure 3-10. In the lower part of the wake flow, the added turbulence intensity is weakened. It is due to the strong turbulence mixing near the ground. It can also be seen that larger thrust coefficient cases exhibit larger turbulence intensity in the wake flow and the maximum turbulence intensity occurs in the near wake region (about 2D downwind). Meanwhile, it can be clearly observed that the nacelle and tower also generate considerable turbulence but it vanishes quickly in the near wake region.

The turbulence intensities in the horizontal x-y plane at the hub height present a dual-peak and approximately axisymmetric distribution with the maximum value near the two side-tip positions as shown in the Figure 3-13 (e)~(h). They are related to the strong shear layer in the wake boundary region. Both horizontal contours and profiles display a slight asymmetry due to the effect of torque on the rotor.

Generally, the LES simulation results of mean velocity and turbulence intensity in the wake flow show good agreement with the experiment data for the model wind turbine. The emphasis is that the mean velocity and turbulence intensity in the wake region of model and utility-scale wind turbines show quite close profiles for each case. It implies that the wake flow strongly depends on the thrust coefficient C_T and ambient turbulence intensity I_a, but weakly depends on the Reynolds number and the specific blade type.

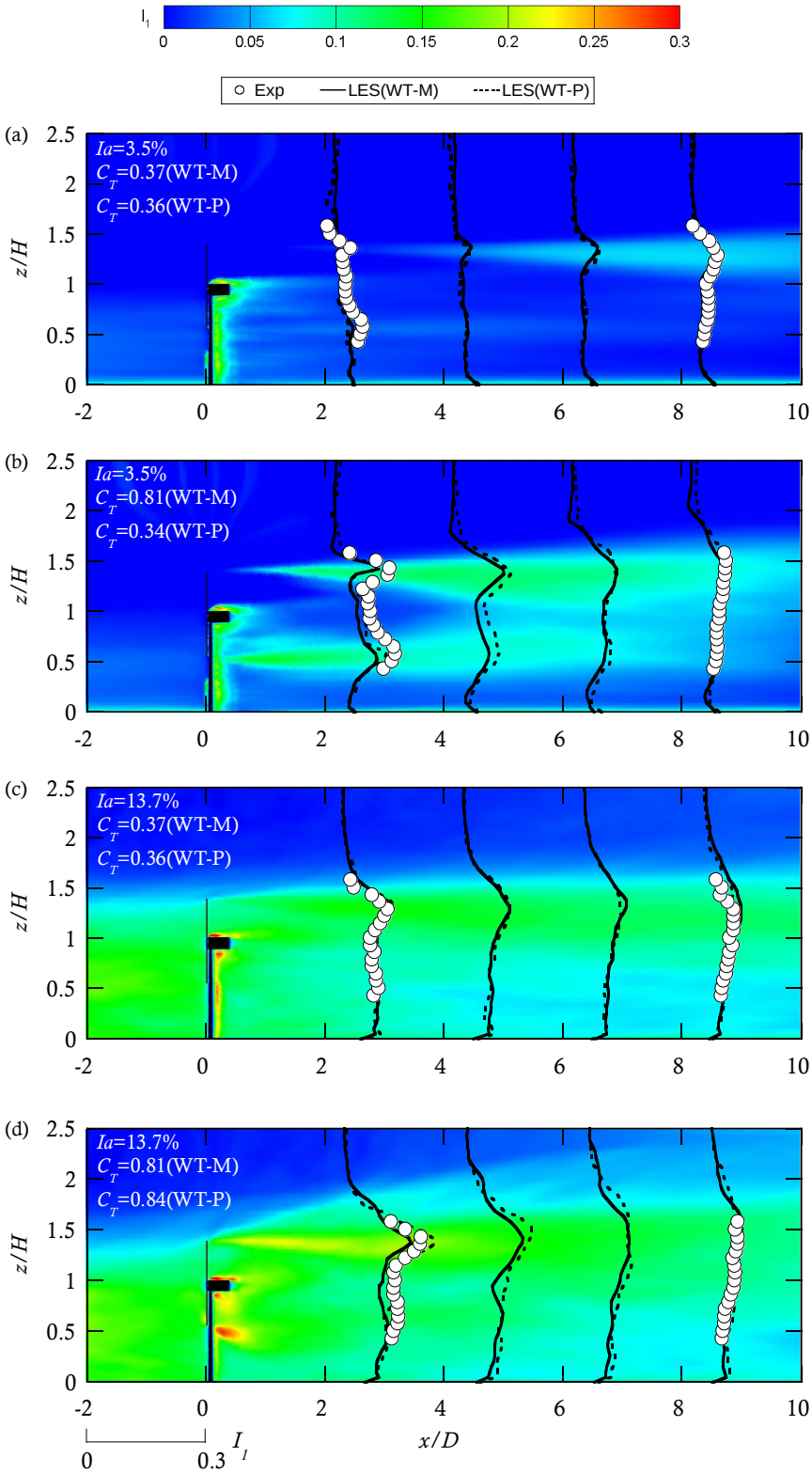

Figure 3-12 Turbulence intensity profiles and contours in vertical $x-z$ plane through the center of rotor.

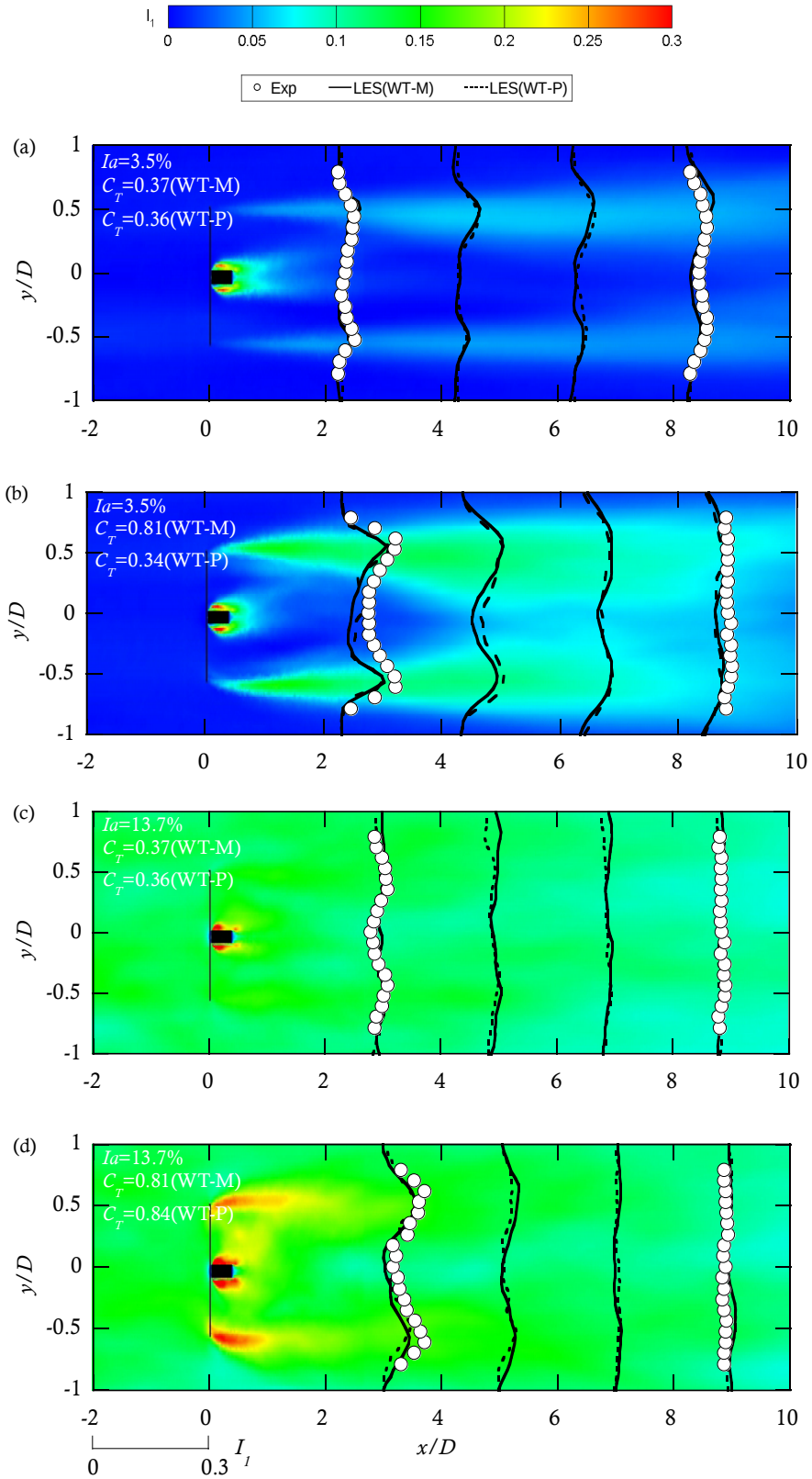

Figure 3-13 Turbulence intensity profiles and contours in the horizontal $x-y$ plane at the hub height.

3.3 Wake Deflection of Yawed Wind Turbine

In this section 3.3, the wind turbine wake behavior under yaw conditions are investigated using RSM simulation. In Section 3.3.1, the computational domain, boundary conditions and specification of various cases are described. In Section 3.3.2, first, the numerical model is validated by comparing with the LES results, including the inflow generation and wake flow simulation. Then in section 3.3.3 and 3.3.4, the wake deflections, mean velocity and turbulence intensity characteristics are systematically investigated.

3.3.1 Numerical Setup

The utility-scale wind turbine model described in section 3.2.1 (Choshi 2.4 MW offshore wind turbine) is adopted to study the wake in various yawed conditions. The effect of the rotor induced forces on the flow is parameterized by using the actuator disk model with rotation under yaw condition (see section 2.2.2).

As shown in Figure 3-14, the computational domain has the streamwise length of 17D, the spanwise length of 6D and the height of 3.2D. The wind turbine model is placed at the center in the spanwise direction, with the rotor diameter D of 0.57 m and the hub height H of 0.7 m. The rotor disk, nacelle and tower are divided in a uniform distance of 0.01 m and then connected smoothly with the main domain by tetrahedral mesh. The main domain is divided by a set of rectangular cells with minimum grid size of 0.001 m near the wall in vertical direction and 0.03 m in horizontal direction. Boundary conditions used in the numerical simulations are summarized in Table 3-3. The values of $U(z)$, $\widetilde{u_i u_j}(z)$ extracted at the location of $x = -4D$ from the LES simulations conducted for the turbulence inflow generation (section 3.2.3) are imposed at the inlet boundary for low and high turbulence boundary layers, respectively. Assuming local Equilibrium of production and dissipation of turbulence kinetic energy $1/2\, P_{ii} = \rho\varepsilon$ in streamwise direction, $k(z)$ and $\varepsilon(z)$ are given by:

$$k(z) = \frac{1}{2}\widetilde{u_i u_j}(z) \tag{3-5}$$

$$\varepsilon(z) = -\widetilde{u_1 u_3}\frac{dU(z)}{dz} \tag{3-6}$$

A stress-free condition ($\partial u/\partial n = 0,\ \partial v/\partial n = 0,\ w = 0$) was used at the top of the domain and a symmetry condition ($\partial u/\partial n = 0,\ \partial w/\partial n = 0,\ v = 0$) at the spanwise sides. At the end of the tunnel, outflow condition is applied ($\partial p/\partial n = 0,\ \partial u/\partial n = 0,\ \partial v/\partial n = 0,\ \partial w/\partial n = 0$). The wall-stress boundary condition is imposed at the ground surface and the roughness height of $z_0 = 1 \times 10^{-4}$ (m) is used.

Eight simulations are performed to study the effects of three parameters, i.e., the yaw angle γ, the trust coefficient C_T and the ambient turbulence intensity I_a. The parameters used in the numerical simulations for each case are summarized in Table 2. The thrust coefficient C_T is defined as:

Table 3-3 Boundary conditions

Boundary	Specification
Inlet	Profiles of $U(z), \overline{u_i u_j}(z), k(z), \varepsilon(z)$
Outlet	Outflow
Side	Symmetry
Top	Symmetry
Bottom	Logarithmic law

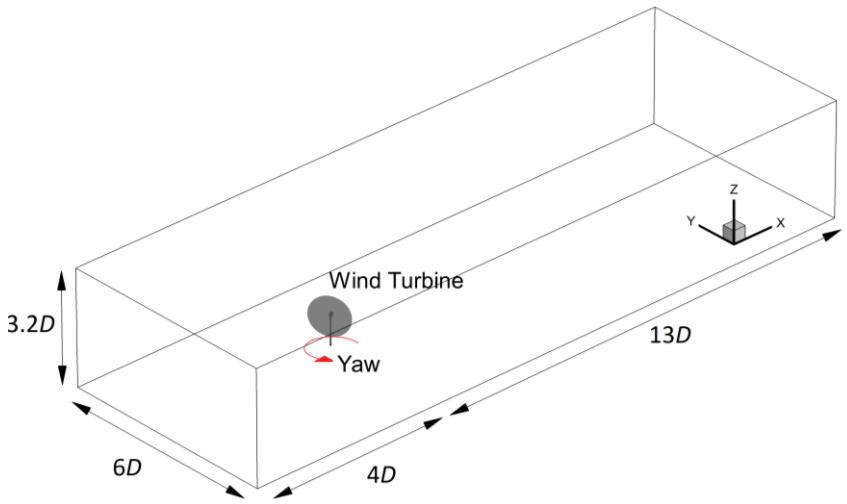

Figure 3-14 Schematic view of the computational domain.

Table 3-4 Parameters of wake simulation under yawed conditions.

Case	γ (Deg.)	I_a	C_T
1	8	0.035	0.36
2	8	0.035	0.84
3	8	0.137	0.36
4	8	0.137	0.84
5	16	0.035	0.36
6	16	0.035	0.84
7	16	0.137	0.36
8	16	0.137	0.84

$$C_T = \frac{F_T}{0.5\rho A_0 (U_h cos\gamma)^2} \tag{3-7}$$

where $A_0 = \pi D^2/4$ is the area of rotor, F_T is the thrust force acting on the rotor and U_h is the mean velocity at the hub height. C_T = 0.36 and 0.84 are selected to consider the two kind of operation condition of maximum power and rated power. Two representative yaw angles of 8° and 16° are chosen to consider the maximum yaw misalignment (≤8°) defined by IEC standard (IEC 61400-1:2005+AMD1:2010, Wind turbines - Part 1: Design requirements, 2014) and the optimal yaw control angle (10°~30°) based on Gebraad et al. (2014).

The RSM simulations are performed with ANSYS Fluent, and the default values recommended by the Fluent Theory Guide (Ansys Inc., 2011) are used for all the model parameters. The second order upwind scheme is applied for the interpolation of velocities, ε and Reynolds Stress. SIMPLE (semi-implicit pressure linked Equations) algorithm is employed for solving the discretized Equations (Ferziger and Perić, 2002).

3.3.2 Validation of Numerical Model

The neutral atmospheric boundary layer profiles without wind turbines are generated by using the inflow condition described in Section 3.3.1. All the profiles of mean velocity in this study are normalized by the mean wind speed U_h at the hub height. The turbulence

intensity is defined as:

$$I_1 = \frac{\sqrt{\overline{u_1 u_1}}}{U_h} \tag{3-8}$$

where $\overline{u_1 u_1}$ is the normal Reynolds stress in the streamwise direction. Note that the ambient turbulence intensity I_a is the streamwise turbulence intensity upwind the turbine at the hub height. Figure 3-15 shows the vertical profiles of mean velocity and turbulence intensity at the several streamwise locations, in which dashed lines denote the result obtained from the LES simulation performed for the inflow generation in see section 3.2.3. Solid lines are the RSM results, and experimental profiles at the position of turbine ($x = 0$) by Ishihara et al. (Ishihara et al., 2004) are also plotted together by the open circles. The quantitative comparison by using the Normalized Root Mean Square Error (NRMSE) (Wikipedia, n.d.) for each case are summarized in Table 3-5, in which the mean values of experimental data are used for the normalization. The RSM result shows good agreement with the LES results and the experimental data.

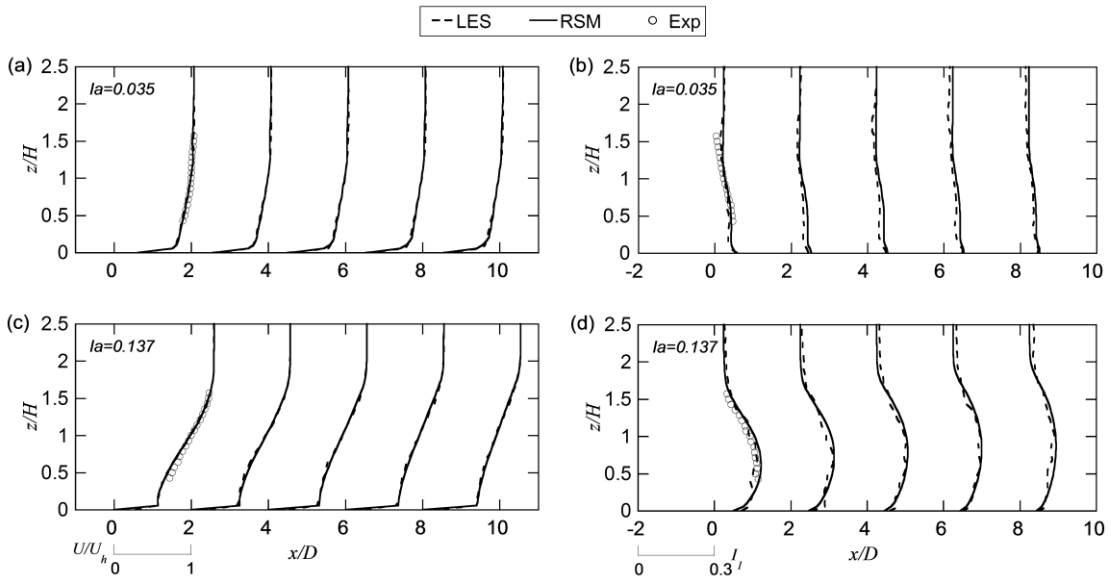

Figure 3-15 Vertical profiles in the simulated neutral atmospheric boundary layers without wind turbines: (a,c) for normalized mean velocity; (b,d) for turbulence intensity.

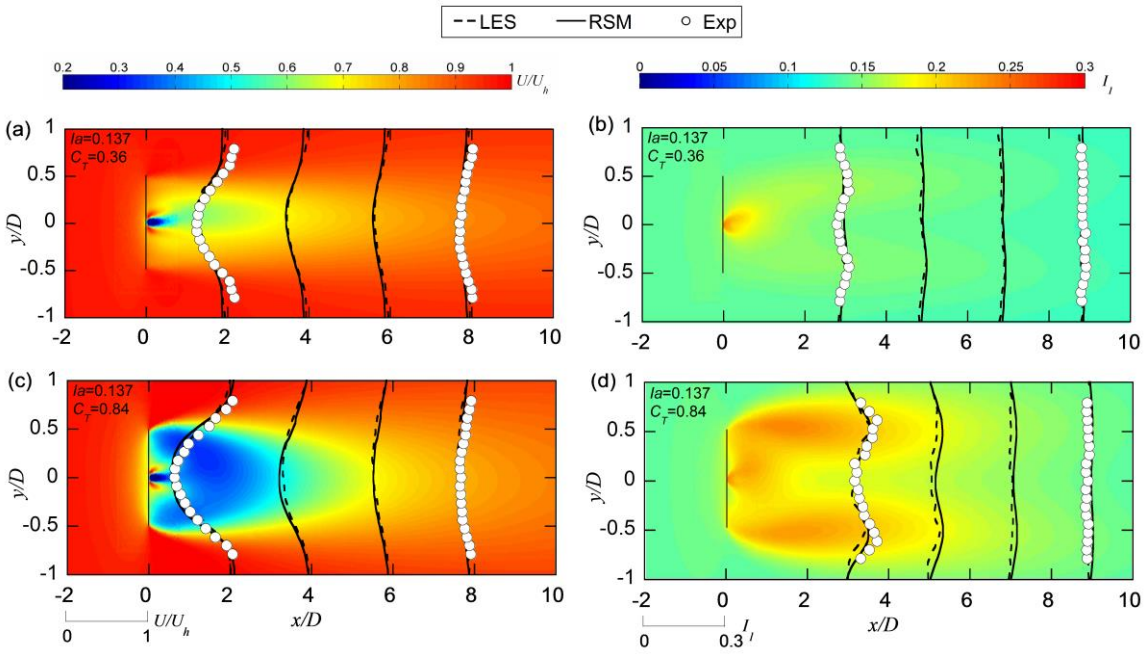

Figure 3-16 Wake characteristics in the horizontal x-y plane at hub height under non-yawed conditions: (a,c) for normalized mean velocity; (b,d) for turbulence intensity.

Table 3-5 NRMSE of simulated profiles respect to experimental data: Inflow for the result in Figure 3-15 and Wake flow for the result in Figure 3-16

		$I_a = 0.035$		$I_a = 0.137$	
Inflow		U/U_h	I_1	U/U_h	I_1
	LES	0.012	0.24	0.031	0.10
	RSM	0.015	0.26	0.032	0.13
		$I_a = 0.137,\ C_T = 0.36$		$I_a = 0.137,\ C_T = 0.84$	
Wake flow		U/U_h	I_1	U/U_h	I_1
	LES	0.068	0.078	0.071	0.12
	RSM	0.078	0.075	0.074	0.10

The LES results for the wind turbine wake simulation have been validated with high accuracy by comparison with the experimental data as shown in section 3.2.4 and 3.2.5. In order to examine the accuracy of the RSM for wind turbine wake simulation, the mean velocity and turbulence intensity in the wake region under the non-yawed condition are compared with the LES results and experimental data (Ishihara et al., 2004) as shown in Figure 3-16, in which the presented results in contour plots are from RSM. The quantitative

comparison by using the NRMSE for each case are summarized in **Table 3-5**. The predicted horizontal profiles of mean velocity and turbulence intensity at selected downwind locations by the RSM agree well with the experimental data and show almost same accuracy with LES.

3.3.3 Mean Velocity under Yawed Conditions

The simulated mean velocity by RSM in the wake region under different yawed conditions are shown in Figure 3-17. The contours of mean velocity and turbulence intensity as well as wake deflections are displayed in the horizontal x-y plane at the hub height ($z = H$). In Figure 3-17, black dashed lines represent the wake boundary denoted by the positions with the mean wind speed equals to the 95% of the free-stream velocity and the open circles denote the wake centers, which are calculated by taking the midpoint between the wake boundaries, based on the same procedure as Jimenez et al. (Jiménez et al., 2009) and Parkin et al. (Parkin et al., 2001). The black dashed lines denote the peak values of turbulence intensity at each location and the open circles show the midpoint position of the two peaks.

From Figure 3-17, it is noticed that the wake velocity deficit reduces when the yaw angle increases. This is consistent with Equation (21) since the larger yaw angle induces smaller thrust force on the rotor. In addition, the wake center trajectories show apparent wake deflections under yawed conditions. As expected, the wake deflection increases with the increase of yaw angle. It can also be seen that the large thrust coefficient (Case 2, 4, 6, 8) induces stronger wake deflection than the cases with small thrust coefficient (Case 1, 3, 5, 7). The high ambient turbulence intensity (Case 3, 4, 7, 8) leads to smaller wake deflection and shorter wake region than cases with the low ambient turbulence (Case 1, 2, 5, 6) as the cases under the non-yawed condition. The high turbulence accelerates the process of flow mixing in the wake region, thus both wake deflection and velocity deficit recover faster than those with the low ambient turbulence intensity.

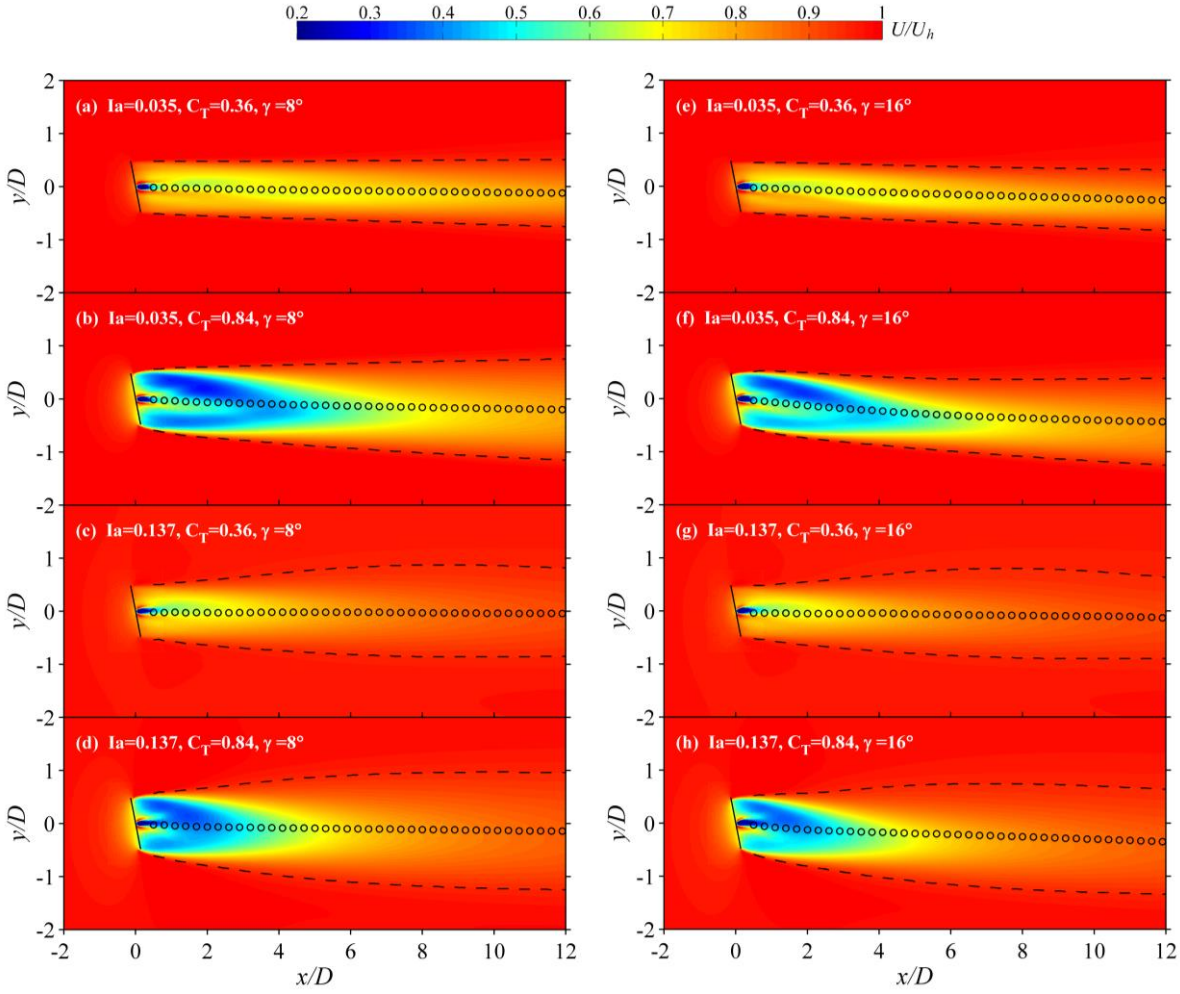

Figure 3-17. Contours of normalized mean velocity U/U_h and wake deflections in the horizontal x-y plane at the hub height. Solid lines represent the wind turbine rotors. Dashed lines and open circles indicate the wake boundaries and wake center trajectories, respectively.

3.3.4 Turbulence Intensity under Yawed Conditions

Figure 3-18 shows that the turbulence intensities in the horizontal x-y plane at the hub height have dual-peak distribution. In the near wake the shear layer leads to two peaks in the turbulence intensity, but in the far wake they are no longer discernible. The wake center trajectories obtained from the mean velocity contours are also plotted together by red dotted lines for comparison. It is found that the midpoint trajectories of turbulence intensity peak trends towards the wake center trajectories. This implies that the turbulence in the wake region are also deflected almost towards the same path as the mean velocity.

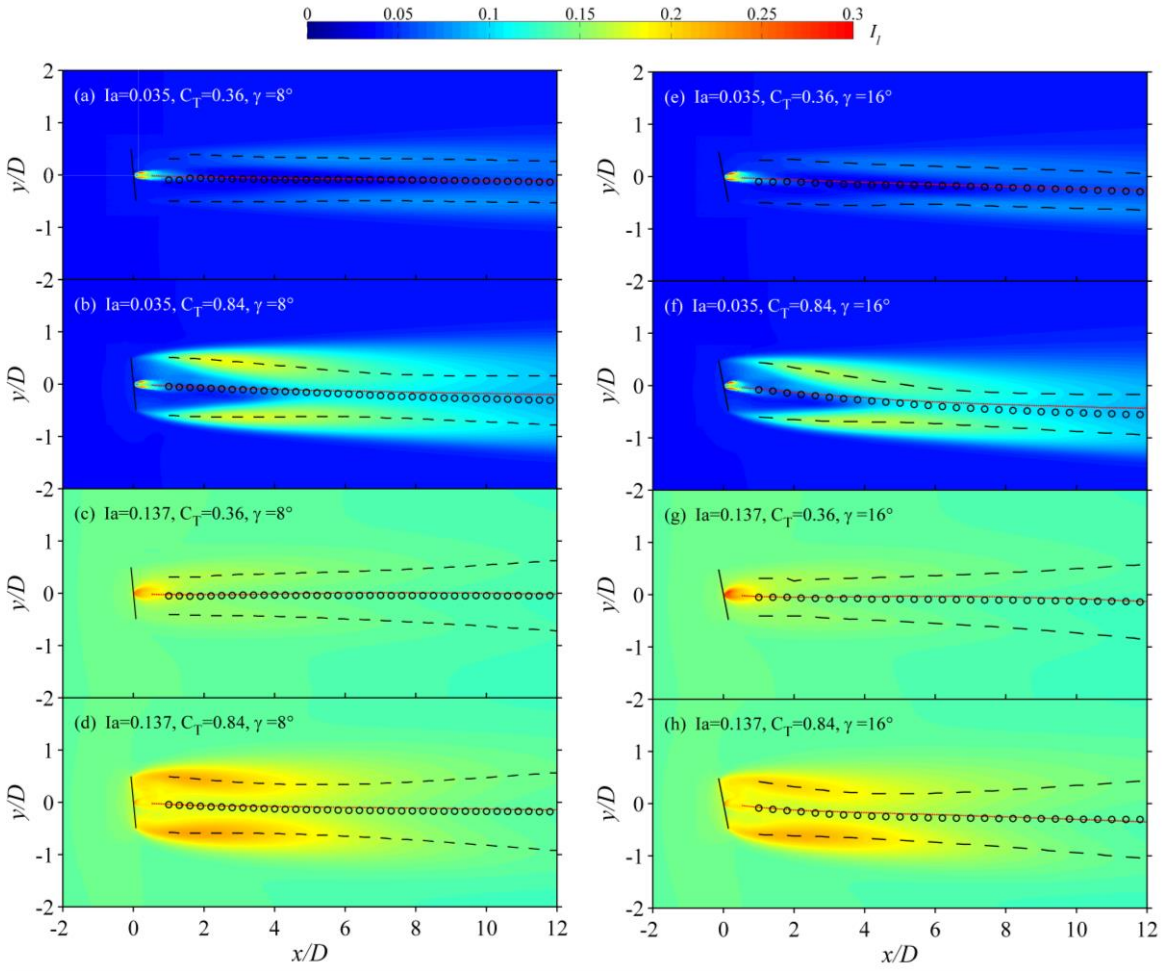

Figure 3-18. Contours of turbulence intensity and wake deflections in the horizontal *x*-*y* plane at the hub height. Solid lines represent the wind turbine rotors. Dashed lines denote the position of peak values of turbulence intensity and the midpoint of the two peaks are indicated by the open circles. The wake center trajectories obtained from the mean velocity contours are plotted by red dotted lines.

3.4 Summary

In this Chapter, a series of numerical simulations of wind turbine wake with different ambient turbulence intensities and thrust coefficients are carried out by using LES for the model and utility-scale wind turbines. Subsequently, a systematic numerical simulation for wind turbine wakes with different ambient turbulence intensities, thrust coefficients, and

yaw angles is carried out by using the Reynolds Stress Model. Following conclusions are obtained:

1. The LES simulation results of mean velocity and turbulence intensity in the wake flow show good agreement with the experiment data for the model wind turbine, which validated the BEM-CFD coupled model for wind turbine wake prediction. The mean velocity and turbulence intensity behind the model and utility-scale wind turbines show quite close profiles, which indicate that the thrust coefficient and ambient turbulence intensity are the dominant parameters for the wake flow in spite of the specific wind turbine type.

2. The effects of ambient turbulence intensity and wind turbine thrust coefficient on the mean velocity are summarized as follows. High ambient turbulence intensity leads to a shorter wake region since the high turbulence accelerates the process of flow mixing in the wake region. In addition, the large thrust coefficient induces stronger velocity deficit in the wake region. The horizontal profiles show axial symmetric and some asymmetry in the near wake region is due to the effect of torque on the rotor.

3. The effects of ambient turbulence intensity and wind turbine thrust coefficient on the turbulence intensity in the wake are summarized as follows. An obvious enhancement of turbulence occurs in the upper half of the wake region, especially at the top tip height. This enhancement is related to the wind shear that is the sharp shape of mean velocity profile near the top tip. In the lower part of the wake flow, the added turbulence intensity is weakened. It is due to the strong turbulence mixing near the ground. Larger thrust coefficient cases exhibit larger turbulence intensity in the wake flow and the maximum turbulence intensity occurs in the near wake region. Meanwhile, it can be clearly observed that the nacelle and tower also generate considerable turbulence but it vanishes quickly in the near wake region. The turbulence intensities in the horizontal direction present a dual-peak and approximately axisymmetric distribution with the maximum value near the two side-tip positions.

4. Reynolds Stress Model shows good performance for wake prediction in atmospheric boundary layer, where both mean velocity and turbulence intensity show good agreement

with those by LES model.

5. The effects of ambient turbulence intensity, thrust coefficient and yaw angle on the wake deflection are systematically investigated. The wake velocity deficit reduces when the yaw angle increases since larger yaw angle induces smaller thrust force on the rotor. In addition, the wake center trajectories show apparent wake deflections under yawed conditions. As expected, the wake deflection increases with the increase of yaw angle. It can also be seen that the large thrust coefficient induces stronger wake deflection than the cases with small thrust coefficient. The high ambient turbulence intensity leads to smaller wake deflection and shorter wake region than cases with the low ambient turbulence as the situation under the non-yawed condition. The high turbulence accelerates the process of flow mixing in the wake region, thus wake deflection recovers faster than those with the low ambient turbulence intensity.

Chapter4. ANALYTICAL MODELLING OF WIND TURBINE WAKES

4.1 Introduction

In this chapter, firstly a new Gaussian-based analytical wake model for prediction of velocity deficit and added turbulence intensity and derived in section 4.2 and 4.3, respectively. The predicted values by the proposed and conventional models are compared with those obtained from the LES simulations and wind tunnel tests. Then, a new analytical wake deflection model for a yawed wind turbine is developed and validated by experimental data. The wake deflection model is later incorporated in the proposed Gaussian-based analytical model to consider the yaw angle effects. The accuracy of the proposed model is examined by numerical simulation results for different ambient turbulence intensities, thrust coefficient effects, and yaw angles. Finally, conclusions of this chapter are summarized.

4.2 Velocity Deficit

The modelling for velocity deficit is derived in this section. Based on the self-similar assumption, the velocity deficit values are determined by a spanwise function and streamwise function, which are discussed in section 4.2.1 and 4.2.2 respectively. Finally, in section 4.2.3, the verification for the velocity deficit model is done by comparison with the numerical results obtained in section 3.2

4.2.1 Spanwise Function

The fully developed wake flow behind still bluff bodies like cylinder and disk have been investigated (Johansson et al., 2003; Schlichting, 1979). The assumption of axisymmetric and the self-similar distribution for the velocity deficit in the far wake region were used in these studies.

In this study, the streamwise velocity deficit induced by the rotor is also assumed to be axisymmetric with respect to the axis of the rotor and have self-similar distribution in the wake cross-section. Therefore, the mean velocity $U(x,y,z)$ in the wake can be determined by the following Equation:

$$U(x,y,z) = U_0(y,z) \text{-} \Delta U \tag{4-1}$$

where $U_0(y,z)$ is the wind speed of incoming flow and ΔU is the velocity deficit induced by the turbine rotor and is a function of x and r which denotes the radial distance from the center of the wake as $r = \sqrt{y^2 + (z-H)^2}$. Since the velocity deficit shows self-similar property, it can be expressed as the product of a streamwise function and a self-similar shape function:

$$\Delta U / U_h = F(C_T, I_a, x/D)\phi(r/\sigma) \tag{4-2}$$

where $F(C_T, I_a, x/D)$ represents the maximum velocity deficit $\Delta U_{\max}$ for each downwind location normalized by the mean wind speed U_h at the hub height, $\phi(r/\sigma)$ is the self-similar distribution of the velocity deficit on the cross section, which is defined as the velocity deficit normalized by the maximum value at the center of the wake section. σ denotes the standard deviation of the mean velocity deficit distribution in the spanwise direction at each cross section and is treated as the representative wake width. $F(C_T, I_a, x/D)$ and $\phi(r/\sigma)$ are termed as "streamwise function" and "spanwise function" for the velocity deficit in this study, respectively.

The Gaussian distribution assumption has been derived by Ishihara et al. (2004) (see Appendix B) and is used as the spanwise function for the velocity deficit in this study as follows:

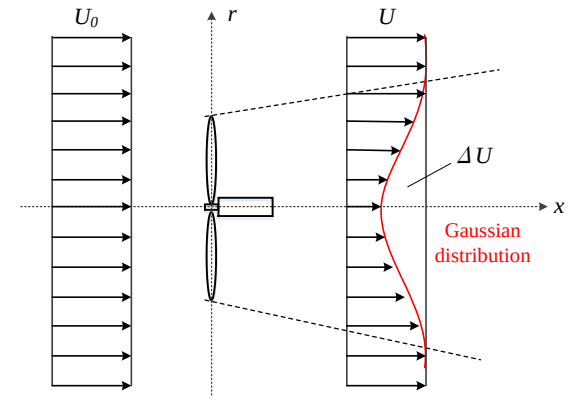

(a) Schematic

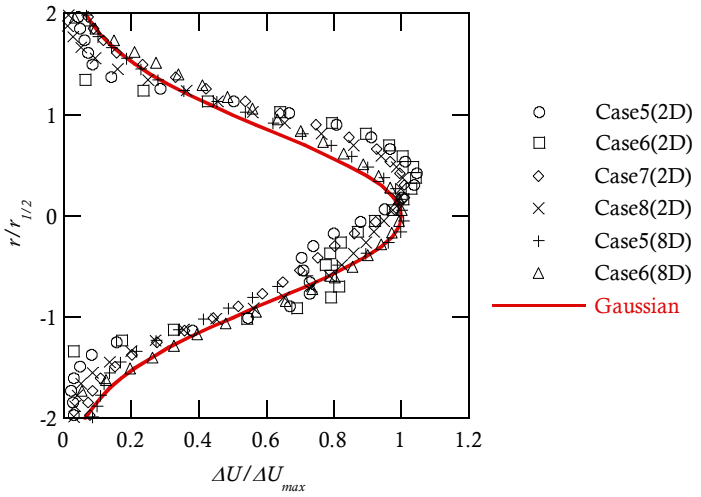

(b) Verification

Figure 4-1 Gaussian distribution for velocity deficit

$$\phi(r/\sigma) = exp\left(-\frac{r^2}{2\sigma^2}\right) \tag{4-3}$$

Figure 4-1 (a) shows the schematic of the Gaussian distribution for velocity deficit. The velocity deficit profiles of selected positions in the horizontal plane at the hub height are normalized by the maximum value $\Delta U_{\max}$ and plotted in Figure 4-1 (b). The distance from the rotor center is normalized by the wake half-width $r_{1/2}$, which is widely used as the characteristic wake width (Bastankhah and Porté-Agel, 2014). $r_{1/2}$ is defined as the half the spanwise distance between two points on a profile at which the mean deficit is half of its maximum. For the Gaussian distribution, σ can be determined by $r_{1/2} = \sqrt{2ln2}\sigma$, and $r_{1/2}$ can be obtained from each spanwise profile as shown in the reference (Bastankhah and

Porté-Agel, 2014). The Gaussian distribution against $r/r_{1/2}$ is also plotted by solid line for comparison. As expected, the LES data generally shows good agreement with the Gaussian distribution in spite of the slight asymmetry in the near wake region.

Similar to Bastankhah and Poste-Agel (2014), the current study also assumes linear expansion of the wake region downstream of the turbine and σ/D is defined as:

$$\frac{\sigma}{D} = k^* \frac{x}{D} + \varepsilon^* \tag{4-4}$$

4.2.2 Streamwise Function

By taking the Gaussian distribution and the self-similarity assumption, Bastankhah and Porte-Agle (2014) derived a streamwise function. However, this analytical solution may diverge in the near wake region as discussed in Appendix. C. Therefore, the first order approximation of Taylor expansion for the Equation. (B.8) is made to find an expression for the far wake region as shown in the following Equation:

$$C(x) = \frac{C_T}{16(k^* x/D + \varepsilon^*)^2} \tag{4-5}$$

Then it is rewritten in a general form as follows:

$$F(C_T, I_a, x/D) = \frac{1}{(a + b \cdot x/D)^2} \tag{4-6}$$

where a and b are the model parameters which can be derived by equating the above two equations as follows:

$$a = 4C_T^{-0.5}\varepsilon^*,\ b = 4C_T^{-0.5}k^* \tag{4-7}$$

A specific expression for k^* has not been given in the reference (Bastankhah and Porté-Agel, 2014). In this study, k^* and ε^* in the above equations are modelled as a function of C_T and I_a. In order to obtain constants in the parameters, except for the results of 8 cases conducted in this study, data from another 9 cases in references (Wu and Porté-Agel, 2011; Xie and Archer, 2014) are also used. There are 10 data points for C_T (0.36, 0.37, 0.81, 0.84,

0.8, 0.461, 0.375, 0.45, 0.55, 0.476) and 7 data points for I_a (0.035, 0.137, 0.048, 0.069, 0.094, 0.134, 0.07) to fit constants in the parameters. Finally, the empirical expression for k^* and ε^* are proposed by data fitting in the far wake region based on Equation (4-5).

$$k^* = 0.11C_T^{1.07}I_a^{0.20},\ \varepsilon^* = 0.23C_T^{-0.25}I_a^{0.17} \tag{4-8}$$

Inserting Equation (4-8) into Equation. (4-7), the parameters a and b are determined as:

$$a = 0.93C_T^{-0.75}I_a^{0.17},\ b = 0.42C_T^{0.6}I_a^{0.2} \tag{4-9}$$

It should be noted that Equation (4-6) can only be used for the far wake region and a correction term p should be added to modify the streamwise function in the near wake region as follows:

$$F(C_T, I_a, x/D) = \frac{1}{(a + b \cdot x/D + p)^2} \tag{4-10}$$

The correction term p in the near wake region should decrease with the distance downwind turbine and can be modelled by a similar form as Equation (4-6), i.e. $p \propto (1 + x/D)^{-2}$. As mentioned in section 3, the influence from turbine aerodynamics is weakened by the high ambient turbulence and large thrust coefficient, thus the correction term can be written as $p \propto C_T^{-\alpha} I_a^{-\beta}(1 + x/D)^{-2}$. The model parameters α and β are obtained by data fitting and expressed as shown in the following Equation:

$$p = 0.15C_T^{-0.25}I_a^{-0.7}(1 + x/D)^{-2} \tag{4-11}$$

The final form of the proposed model and parameters for the velocity deficit are summarized in the Table 4-2.

Figure 4-2 shows the variation of normalized velocity deficit at the hub height with normalized distance downwind the turbine. The experimental data marked by the triangles and the LES results denoted by the open circles and crosses are the value measured along the line in the streamwise direction through the rotor centre. The solid lines denote the result of the proposed model and dotted lines are the result from the model by Katic et al. (1986), which is expressed as follows:

$$\frac{\Delta U}{U_h} = \frac{1-\sqrt{1-C_T}}{(1+2k_w x/D)^2} \tag{4-12}$$

where k_w is the wake decay coefficient and the recommend values is $k_w = 0.4I_a$ for the flat terrain under neutral conditions (Peña et al., 2016).

As can be seen from Figure 4-2, the proposed model shows good agreement with the LES data for all case in the near as well as the far wake region. The model by Katic et al. generally underestimates the velocity deficit since it uses the top-hat shape. The velocity deficits reach maximum in the near wake region and decrease more slowly for the low

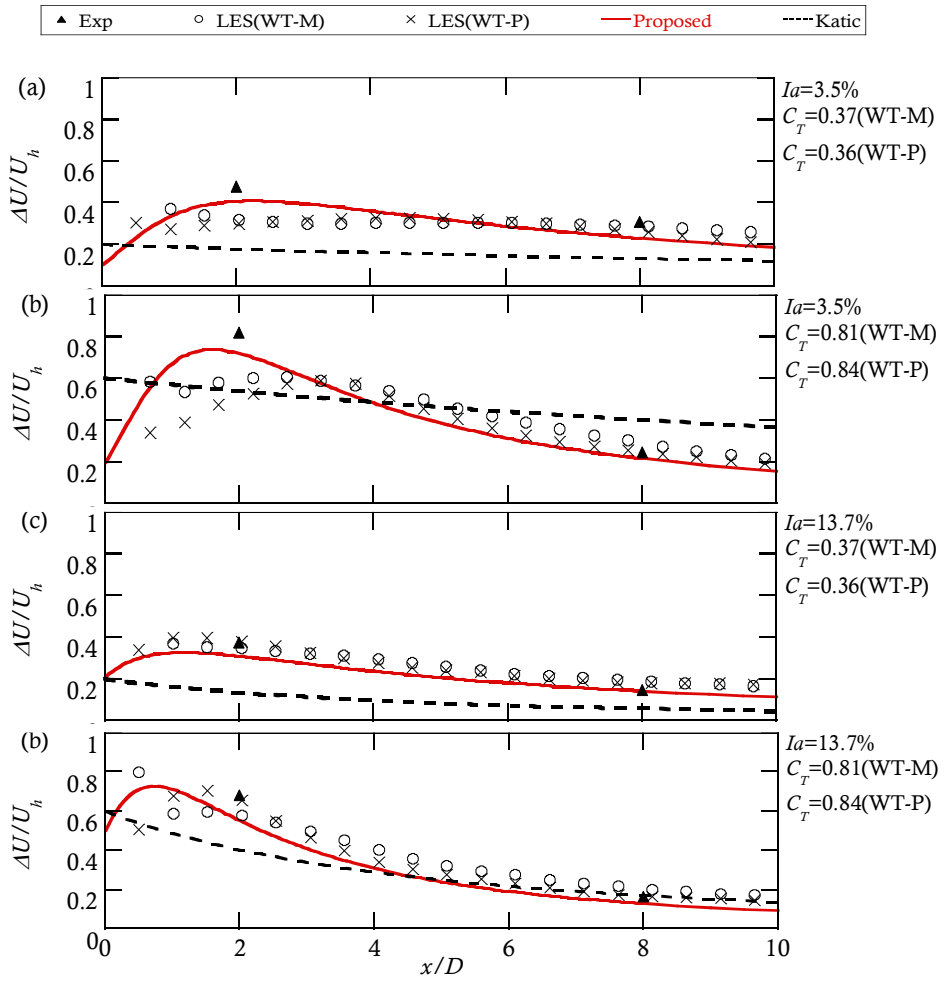

Figure 4-2 Variation of normalized velocity deficit at the hub height with normalized distance downwind the turbine:(a) Case 1 and 5, (b) Case 2 and 6, (c) Case 3 and 7, (d) Case 4 and 8

ambient turbulence cases than those for the high ambient turbulence cases. The predicted velocity deficits by the proposed model catch these behaviours well.

The validation metric, hit rate q (Schatzmann et al., 2010) is used here to quantify the agreement between LES results and values predicted by wake models. q is defined as:

$$q = \frac{1}{N}\sum_{i=1}^{N} n_i \quad with\ n_i = \begin{cases} 1 & \left|\frac{y_i - x_i}{x_i}\right| \le D_q \quad or \quad |y_i - x_i| \le W_q \\ 0 & else \end{cases} \tag{4-13}$$

where, y_i and x_i are the obvserved (LES) and predicted (wake model) values of a given variable for smaple i, respectively, and N is the number of data points. A hit rate q specifies the fraction of model results that differ within an allowed range D_q or W_q from the comparison data. D_q accounts for the relative uncertainty of the predicted values, and W describes the repeatability of the predicted values. The ideal values of the metrics that correspond to perfect agreement is 1.0 for q. The thresholds for q are D_q=0.15 for mean wind speed and D_q=0.21 for turbulence intensity since the standard deviation of variable gives error as $\sqrt{2}$ as the variable itself. $W_q = 0.05|max|$ is used for both mean wind speed and turbulence intensity, in which $|max|$ is a maximum value supposed in the obvservation .

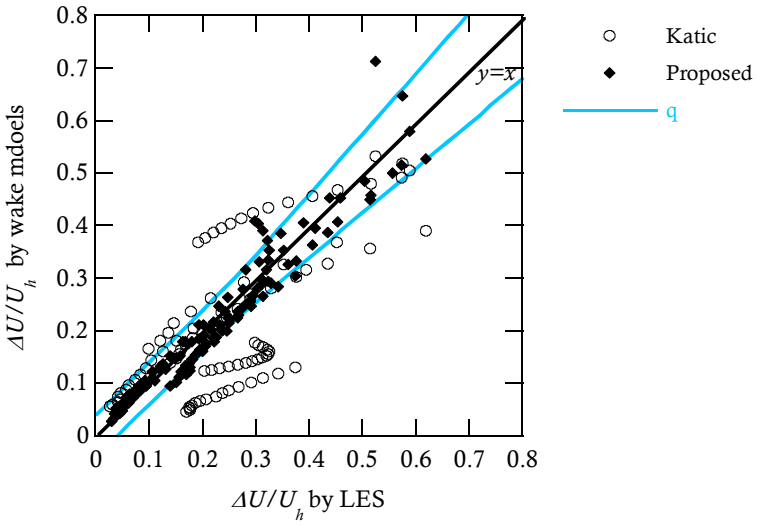

Figure 4-3 Scatter plots for comparison between the wake model and the LES results for normalized velocity deficit at the hub height

Figure 4-3 shows scatter plots for comparison between the wake model and the LES results for normalized velocity deficit at the hub height, together with the corresponding validation metric boundary. The LES data from this study as well as those reported by Wu and Porté-Agel (2012) are used. The proposed model shows better performance for velocity deficit prediction with a higher hit rate than the Katic model as shown in Table 4-1.

4.2.3 Verification

Figure 4-4 and Figure 4-5 compares the vertical as well as horizontal profiles of velocity deficit for each case obtained from the present LES results and the two wake models. It can be seen that the proposed model gives more reasonable distributions than the top-hat shape used by Katic et al., which underestimates the velocity deficit in the center of wake and overestimates them in the outside regions.

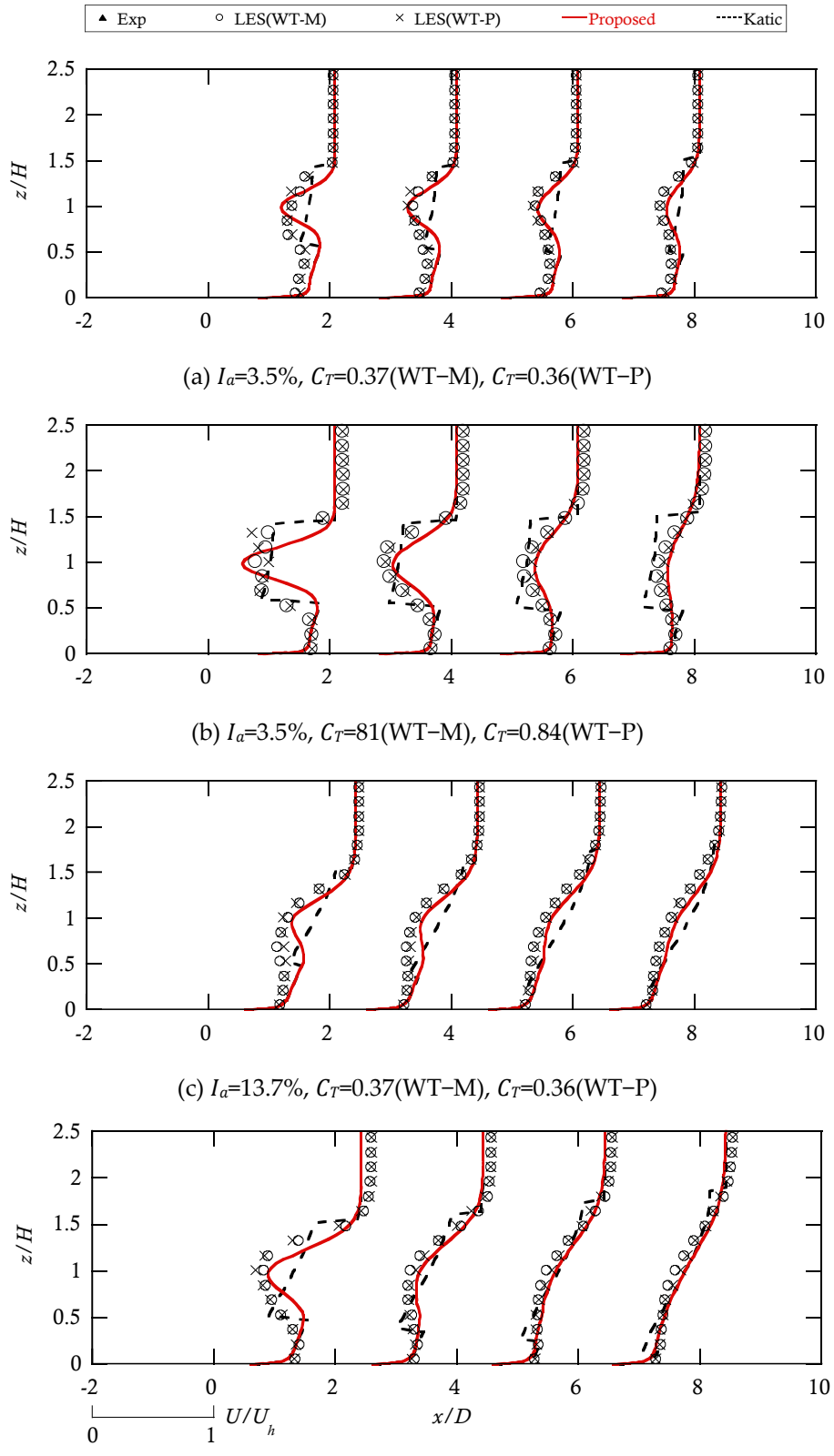

(a) I_a=3.5%, C_T=0.37(WT−M), C_T=0.36(WT−P)

(b) I_a=3.5%, C_T=81(WT−M), C_T=0.84(WT−P)

(c) I_a=13.7%, C_T=0.37(WT−M), C_T=0.36(WT−P)

(d) I_a=13.7%, C_T=81(WT−M), C_T=0.84(WT−P)

Figure 4-4 Validation for mean velocity distribution in vertical direction

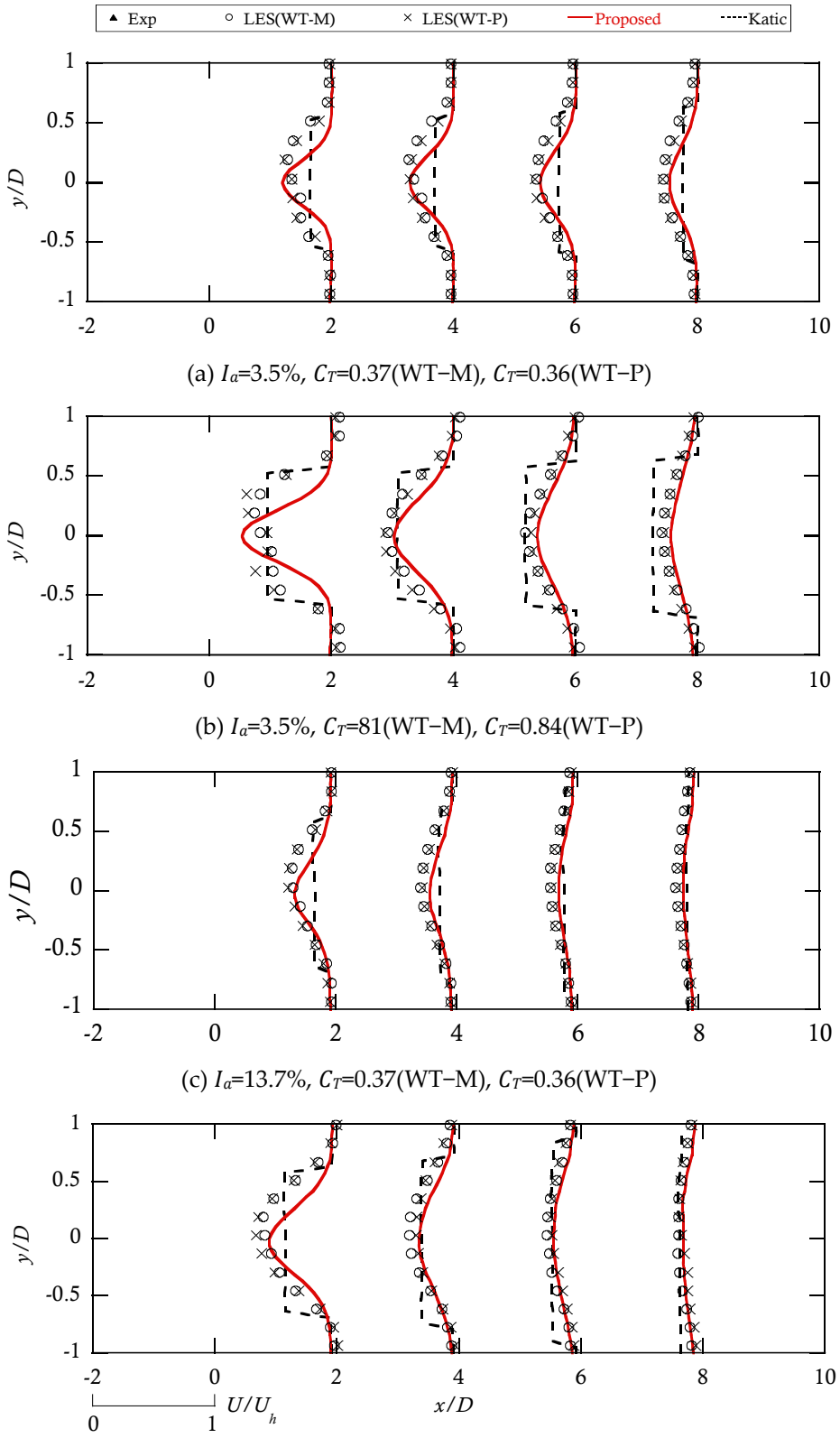

(a) I_a=3.5%, C_T=0.37(WT−M), C_T=0.36(WT−P)

(b) I_a=3.5%, C_T=81(WT−M), C_T=0.84(WT−P)

(c) I_a=13.7%, C_T=0.37(WT−M), C_T=0.36(WT−P)

(d) I_a=13.7%, C_T=81(WT−M), C_T=0.84(WT−P)

Figure 4-5 Validation for mean velocity distribution in horizontal direction.

4.3 Added Turbulence Intensity

As presented in section 3.2.5, the turbulence distribution in the wake region also shows symmetric in the horizontal direction, and the non-symmetric character of turbulence distribution in the vertical distribution is associated with the non-symmetric character of the incident flow. Therefore, firstly the added turbulence intensity is assumed axial symmetric, and the effects of incoming shear layer are later considered to amend for the non-symmetricity in the vertical direction. The turbulence standard deviation in any position $\sigma_u(x,y,z)$ downwind the turbine is determined by the ambient turbulence standard deviation $\sigma_{u_0}(y,z)$ and the added turbulence standard deviation $\Delta u'$ as shown in the following Equation:

$$\sigma_u(x,y,z) = \sqrt{\sigma_{u_0}^2(y,z) + \Delta u'^2} \tag{4-14}$$

4.3.1 Spanwise Function

The self-similarity assumption is also taken for the added turbulence standard deviation $\Delta u'$, which is a function of x and r. The added turbulence intensity ΔI_1 can also be modelled as the product of the maximum value at the location x and the distribution function as follows:

$$\Delta I_1 = \frac{\Delta u'}{U_h} = G(C_T, I_a, x/D)\varphi(r/\sigma) \tag{4-15}$$

where $G(C_T, I_a, x/D)$ is the streamwise function denoting the maximum added turbulence intensity ΔI_{1max} at the tip of the blade for each downwind location, and $\varphi(r/\sigma)$ is the spanwise function which is assumed as a dual-Gaussian shape as shown in Figure 4-6 (a) and σ is the same parameter as in the Gaussian distribution for the velocity deficit.

The maximum value of added turbulence intensity occurs at the tip of blade instead of the center of the rotor. Similar to the velocity deficit distribution in the wake region, the Gaussian shape is used for the added turbulence intensity with peak of the distribution occurring at the rotor tip as shown in Figure 4-6 (a), and is expressed as:

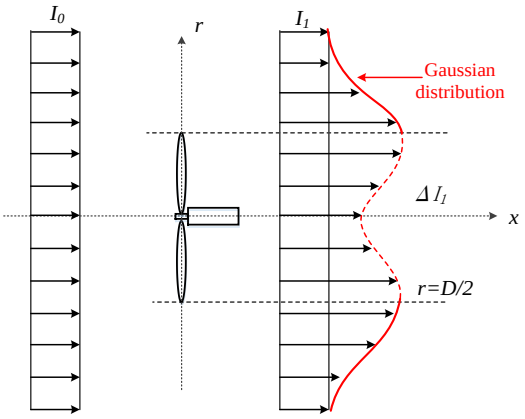

(a) Schematic

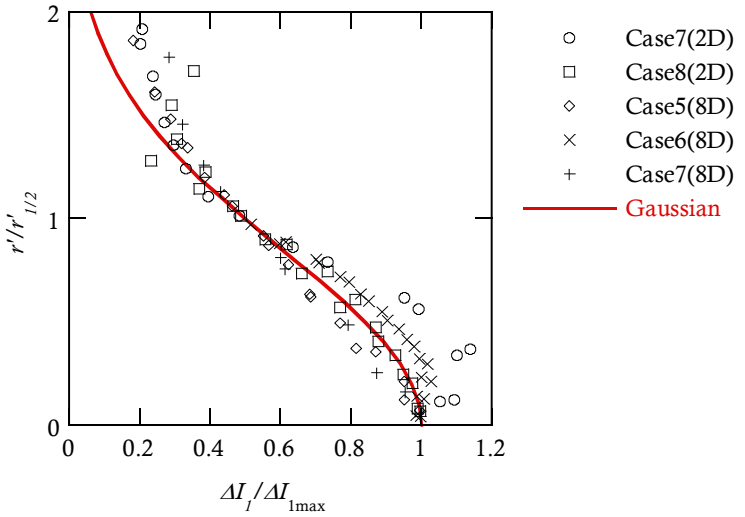

(b) Verification

Figure 4-6 Gaussian distribution for added turbulence intensity

$$\varphi(r/\sigma) = exp\left(-\frac{r'^2}{2\sigma^2}\right) \tag{4-16}$$

In Figure 4-6 (b), the horizontal distributions of added turbulence intensity are plotted together with the Gaussian distribution, in which $r'_{1/2}$ is the half-width for added turbulence intensity distribution at one side. It can be seen that the added turbulence intensity can also be evaluated well by the Gaussian distribution. In the Equation (4-16), r' can be rewritten as $r' = r - D/2$. In the region between the tip sides ($r \leq D/2$) as shown in Figure 4-6 (a), the effect from each side can be combined by the superposition of the turbulence generated at the tip annulus. In this way, the distribution of added turbulence

intensity in the spanwise direction can be expressed by the following Equations:

$$\varphi(r/\sigma) = k_1 exp\left(-\frac{(r - D/2)^2}{2\sigma^2}\right) + k_2 exp\left(-\frac{(r + D/2)^2}{2\sigma^2}\right) \tag{4-17}$$

where k_1 and k_2 are the model parameters and are set to 1 and 0 in the outside region ($r > D/2$) and determined based on the continuity and monotonicity constraint when $r \leq D/2$ as shown in the following Equations:

$$k_1 = \begin{cases} cos^2\left(\pi/2 \cdot (r/D - 0.5)\right) & r/D \leq 0.5 \\ 1 & r/D > 0.5 \end{cases} \tag{4-18}$$

$$k_2 = \begin{cases} cos^2\left(\pi/2 \cdot (r/D + 0.5)\right) & r/D \leq 0.5 \\ 0 & r/D > 0.5 \end{cases} \tag{4-19}$$

4.3.2 Streamwise Function

Assuming that the turbulence viscosity ν_t is constant and velocity deficit is small in the far wake region, namely $U(x, y, z) \approx U_0$, the transport Equation of streamwise added turbulent standard deviation $\Delta u'^2$ has the same expression form as the transport Equation of velocity deficit as shown in Equation. B.3 (see Appendix B):

$$U_0 \frac{\partial(\Delta u'^2)}{\partial x} = \frac{\nu_t}{r'} \frac{\partial}{\partial r'}\left(r' \frac{\partial(\Delta u'^2)}{\partial r'}\right) \tag{4-20}$$

Therefore, similar to the expression of velocity deficit, the maximum $\Delta u'^2$ for each downwind location in the wake region can be modelled analogically as:

$$\Delta u'^2_{max} = \frac{1}{(a' + b'x)^2} \tag{4-21}$$

The maximum added turbulence intensity $\Delta I_{1\max}$ for each downwind location in the wake region can be expressed as:

$$\Delta I_{1max} = \frac{\Delta u'_{max}}{U_h} = G(C_T, I_a, x/D) = \frac{1}{d + e \cdot x/D} \tag{4-22}$$

where the parameter d and e are also a function of the thrust coefficient C_T and the

ambient turbulence intensity I_a and they are obtained by data fitting in the far wake region based on Equation (4-21) as follows:

$$d = 2.3C_T^{-1.2},\ e = 1.0I_a^{0.1} \tag{4-23}$$

As mentioned above for the velocity deficit modelling, it is also necessary to add a correction term q to consider the added turbulence intensity in the near wake region and the streamwise function is expressed by the following Equation:

$$G(C_T, I_a, x/D) = \frac{1}{d + e \cdot x/D + q} \tag{4-24}$$

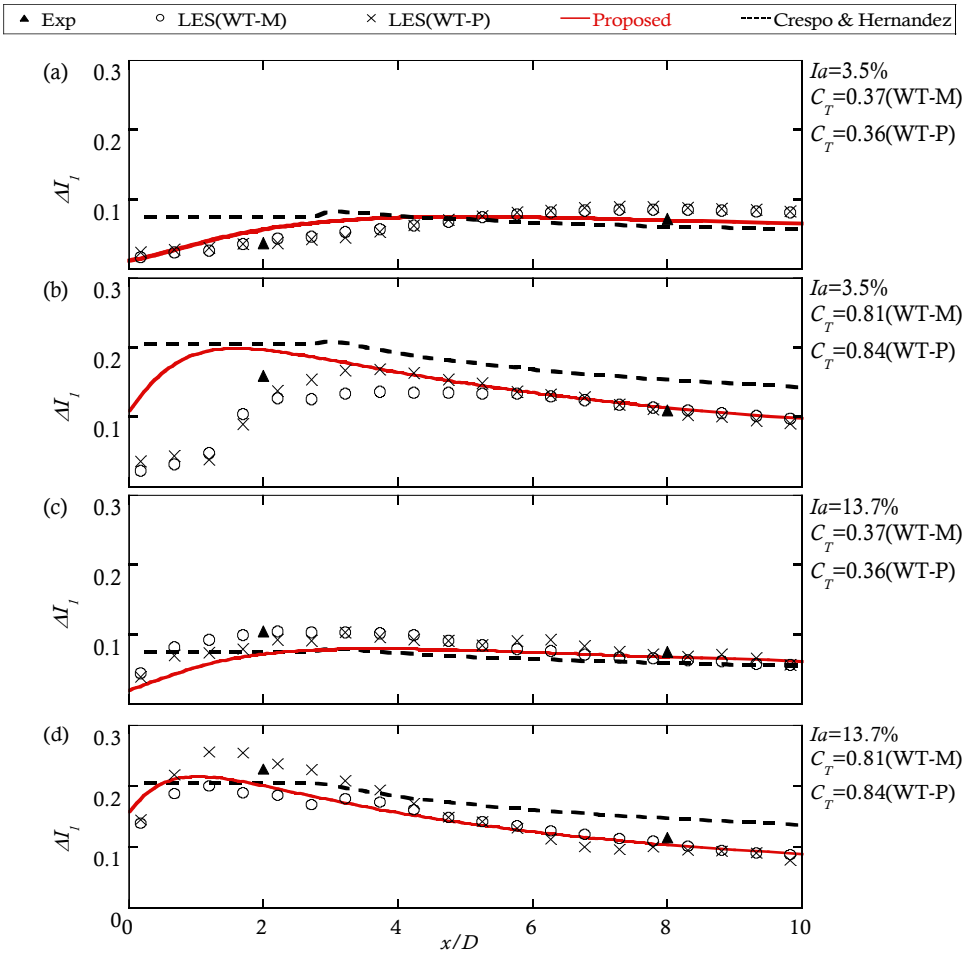

Figure 4-7 Variation of added turbulence intensity at the top tip height with normalized distance downwind the turbine: (a) Case1 and 5, (b)Case2 and 6, (c)Case3 and 7, (d)Case4 and 8

The correction term q in the near wake region is also obtained by the data fitting as shown in the following Equation:

$$q = 0.7C_T^{-3.2}I_a^{-0.45}(1 + x/D)^{-2} \tag{4-25}$$

Figure 4-7 shows the variation of added turbulence intensity at the top tip height with the normalized distance downwind the turbine. The solid lines denote the results predicted by the proposed model and dotted lines are the results from the model by Crespo and Hernández (Crespo and Hernández, 1996), which has the expression for the near and far wake regions as follows:

$$\Delta I_1 = \begin{cases} 0.362\left(1 - \sqrt{1 - C_T}\right) & (x < 3D) \\ 0.73\left(\dfrac{1 - \sqrt{1 - C_T}}{2}\right)^{0.83} I_a^{-0.0325}\left(\dfrac{x}{D}\right)^{-0.32} & (x \geq 3D) \end{cases} \tag{4-26}$$

It can be seen that the proposed model captures the changing of ΔI_1 well for all the cases. In the far wake region, the Crespo and Hernández's model slightly underestimates ΔI_1 for small C_T cases and overestimates ΔI_1 for large C_T cases. On the other hand, it overestimates ΔI_1 in the near wake region for some cases.

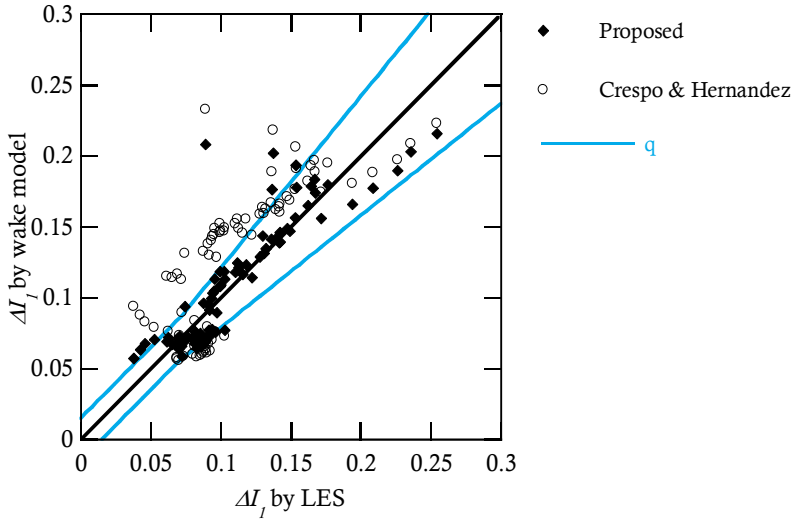

Figure 4-8 Scatter plots for comparison between the wake model and the LES results for added turbulence intensity at the top-tip height

Table 4-1 Hit rate for the wake model in the streamwise direction

Wake model	$\Delta U/U_h$	ΔI_1
Proposed model	0.86	0.81
Katic	0.31	--
Crespo and Hernandez	--	0.36

Figure 4-8 shows scatter plots for comparison between the wake model and the LES results for added turbulence intensity at the top-tip height, together with the corresponding validation metric boundary. The LES data from this study as well as those reported by Wu and Porté-Agel (2012) are used. The proposed model shows better performance for added turbulence intensity prediction with a higher hit rate than the Crespo and Hernández's model as shown in Table 4−1.

In addition, a correction term $\delta(z)$ to describe the weakened turbulence intensity in the lower part of the wake flow is added as follows:

$$\delta(z) = \begin{cases} 0 & (z \geq H) \\ I_a sin^2\left(\pi \frac{H-z}{H}\right) & (z < H) \end{cases} \tag{4-27}$$

The complete form of the proposed model for the added turbulence intensity is also summarized in Table 4-2.

4.3.3 Verification

Figure 4-9 and Figure 4-10 shows the vertical as well as horizontal profiles of turbulence intensity for each case obtained from the LES results and wake models. It can be clearly observed that the proposed wake model well predicts the spatial distributions and maximum values of the turbulence intensities, while the model based on the top-hat shape overestimates the turbulence intensity at the center of wake and underestimates them in the outside region.

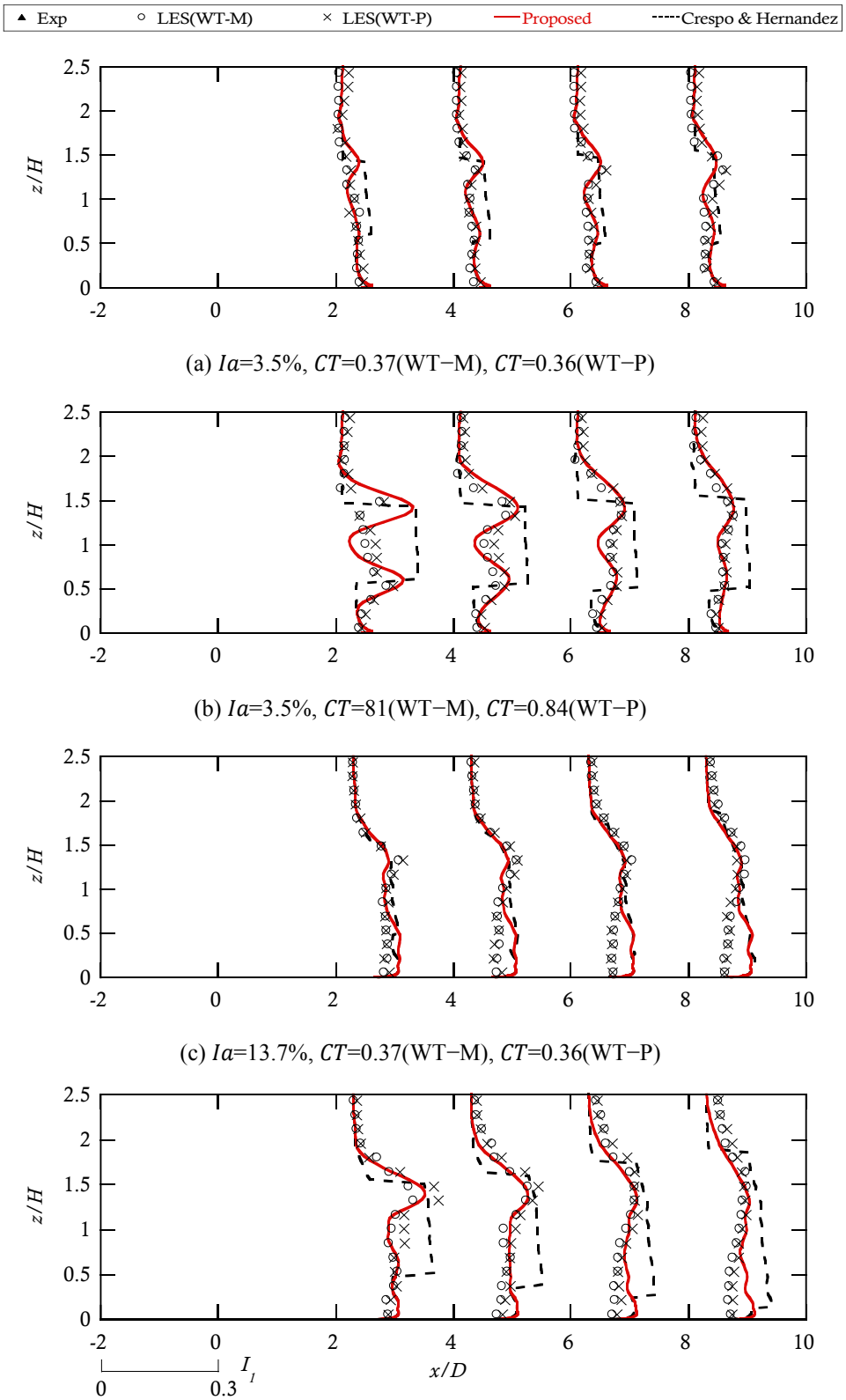

(a) Ia=3.5%, CT=0.37(WT−M), CT=0.36(WT−P)

(b) Ia=3.5%, CT=81(WT−M), CT=0.84(WT−P)

(c) Ia=13.7%, CT=0.37(WT−M), CT=0.36(WT−P)

(d) Ia=13.7%, CT=81(WT−M), CT=0.84(WT−P)

Figure 4-9 Validation for turbulence intensity distribution in vertical direction.

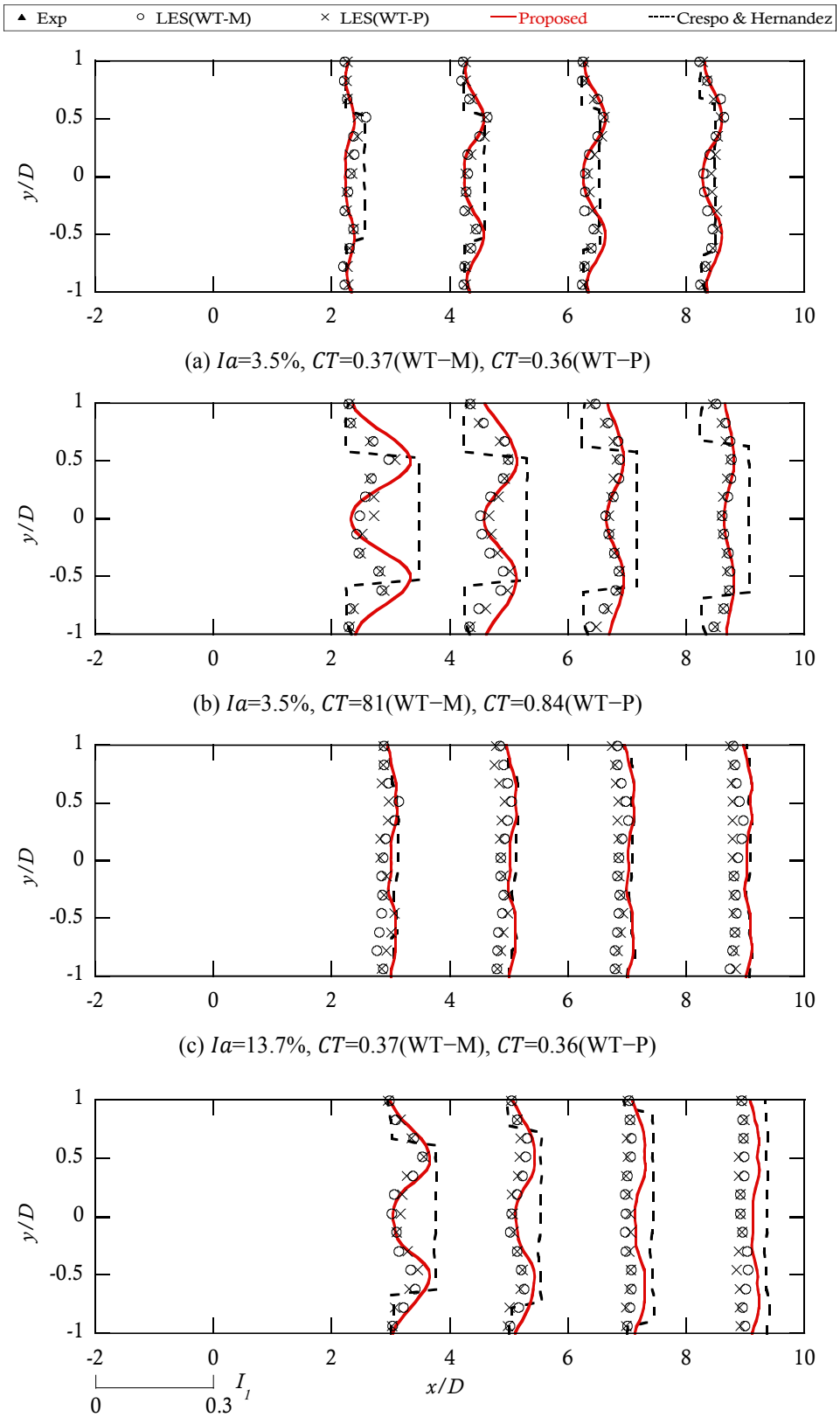

(a) Ia=3.5%, CT=0.37(WT−M), CT=0.36(WT−P)

(b) Ia=3.5%, CT=81(WT−M), CT=0.84(WT−P)

(c) Ia=13.7%, CT=0.37(WT−M), CT=0.36(WT−P)

(d) Ia=13.7%, CT=81(WT−M), CT=0.84(WT−P)

Figure 4-10 Validation for turbulence intensity distribution in horizontal direction

Table 4-2 Summary of the new Gaussian-based analytical wake model

Wake model	Representative wake	Velocity deficit	Added turbulence intensity
Formulas	$\sigma/D = k^* x/D + \varepsilon^*$	$\Delta U(x,y,z)/U_h = \frac{1}{\{a + b \cdot x/D + c(1+x/D)^{-2}\}^2} \cdot \exp\left(-\frac{r^2}{2\sigma^2}\right)$ $r = \sqrt{y^2 + (z-H)^2}$	$\Delta I_1(x,y,z) = \frac{1}{d + e \cdot x/D + f(1+x/D)^{-2}} \cdot \left\{k_1 \exp\left(-\frac{(r-D/2)^2}{2\sigma^2}\right) + k_2 \exp\left(-\frac{(r+D/2)^2}{2\sigma^2}\right)\right\} - \delta(z)$, $\delta(z) = \begin{cases} 0 & (z \geq H) \\ I_a \sin^2\left(\pi \frac{H-z}{H}\right) & (z < H) \end{cases}$
Parameters	$k^* = 0.11 C_T^{1.07} I_a^{0.20}$ $\varepsilon^* = 0.23 C_T^{-0.25} I_a^{0.17}$	$a = 0.93 C_T^{-0.75} I_a^{0.17}$ $b = 0.42 C_T^{0.6} I_a^{0.2}$ $c = 0.15 C_T^{-0.25} I_a^{-0.7}$	$d = 2.3 C_T^{-1.2}$ $e = 1.0 I_a^{0.1}$ $f = 0.7 C_T^{-3.2} I_a^{-0.45}$ $k_1 = \begin{cases} \cos^2(\pi/2 \cdot (r/D - 0.5)) & r/D \leq 0.5 \\ 1 & r/D > 0.5 \end{cases}$ $k_2 = \begin{cases} \cos^2(\pi/2 \cdot (r/D + 0.5)) & r/D \leq 0.5 \\ 0 & r/D > 0.5 \end{cases}$

4.3.4 Comparison with Frandsen's Model

In the IEC61400-1 for wind turbine design ("IEC 61400-1:2005+AMD1:2010, Wind turbines - Part 1: Design requirements," 2014), the turbulence intensity in a wind turbine wake is estimated by the following formula:

$$\hat{\sigma}_T = \sqrt{\hat{\sigma}_w^2 + \hat{\sigma}_c^2} \tag{4-28}$$

where $\hat{\sigma}_T$ is the turbulence standard deviation in the wake region, $\hat{\sigma}_w$ is the turbulence standard deviation generated by the turbine and $\hat{\sigma}_c^2$ is the ambient turbulence standard deviation. The added turbulence intensity is defined as the $\hat{\sigma}_w$ normalized by the mean wind speed U_h at the hub height as follows,

$$\Delta I_1 = \frac{\hat{\sigma_w}}{U_h} = \frac{1}{1.5 + \frac{0.8}{\sqrt{C_T}}\frac{x}{D}} \tag{4-29}$$

This model by Frandsen (2007) was derived based on the data fitting at the wind speed in a range from 9m/s to 11m/s and the thrust coefficient C_T was about 0.7 based on the approximation of $C_T \approx 7/U_h$. In this model, the turbulence standard deviation is assumed to be constant in the cross section of the wake.

In addition, it should be noted that in the conventional wake models, including the proposed model, the added turbulence intensity is defined by reference of the mean velocity U_h at the hub height. However, the local turbulence intensity is crucial for a specific turbine load evaluation in the real wind farm as investigated by Göçmen et al. (2016). It is defined by the reference of local mean velocity and is expressed as follows:

$$\Delta I_1^{local} = \frac{\Delta I_1 \cdot U_h}{U} \tag{4-30}$$

where U is the local mean velocity in the wake region and is calculated based on Equation (4-1).

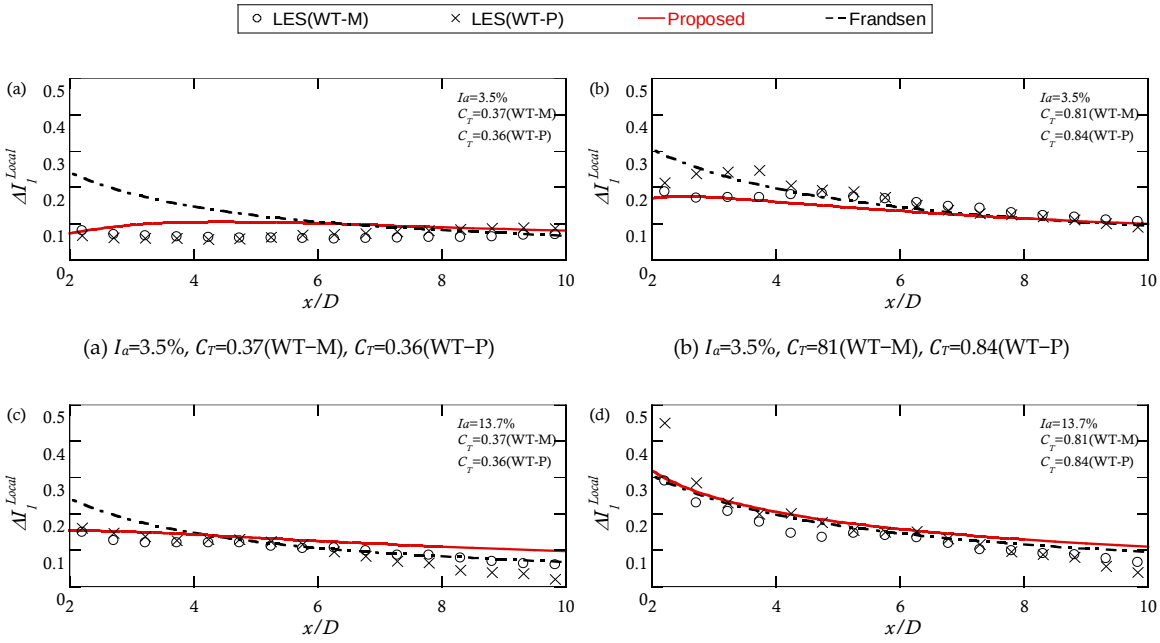

(a) I_a=3.5%, C_T=0.37(WT−M), C_T=0.36(WT−P)

(b) I_a=3.5%, C_T=81(WT−M), C_T=0.84(WT−P)

(c) I_a=13.7%, C_T=0.37(WT−M), C_T=0.36(WT−P)

(d) I_a=13.7%, C_T=81(WT−M), C_T=0.84(WT−P)

Figure 4-11 Local added turbulence intensity at the hub height

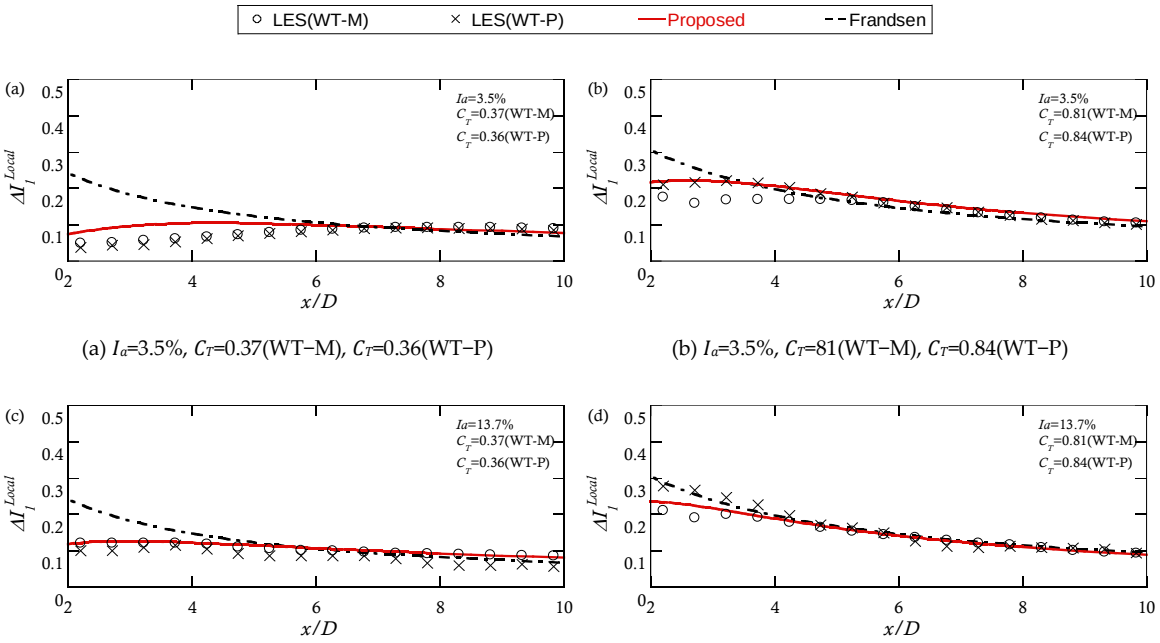

(a) I_a=3.5%, C_T=0.37(WT−M), C_T=0.36(WT−P)

(b) I_a=3.5%, C_T=81(WT−M), C_T=0.84(WT−P)

(c) I_a=13.7%, C_T=0.37(WT−M), C_T=0.36(WT−P)

(d) I_a=13.7%, C_T=81(WT−M), C_T=0.84(WT−P)

Figure 4-12 Local added turbulence intensity at the top tip height

In order to examine applicability of the proposed model and Frandsen's model, the local turbulence intensity predicted by the wake models and LES at hub height and top tip height are shown in Figure 4-11 and Figure 4-12. These two representative locations are chosen to consider that maximum mean velocity deficit at the hub height and the maximum added standard deviation at the top tip height, which might represent the maximum local turbulence intensity in the cross section of wake. The wind turbines are rarely laid close less than 2D, therefore the data in the wake region of $x/D > 2$ are shown. It can be seen that the local turbulence intensity predicted by the proposed model generally show good agreement with LES data in both near and far wake region. The Frandsen's model also shows good prediction in the far wake region but overestimates the values in the near wake region for small C_T cases since it is originally applicable to the case with $C_T \approx 0.7$ as mentioned above. It implies that the Frandsen's model is slightly conservative from the point of view of safety for the turbulence intensity prediction in near wake region under the condition with small thrust coefficient.

Similar to the approach implemented in reference (Niayifar and Porté-agel, 2016) for power prediction in a wind farm by using the single wake model of Bastanhah and Porté-Agel , the proposed model can also be directly applied over a small-scale wind farm. On the other hand, inside a large-scale wind farm more with than 5 rows of wind turbine, the single wake model needs modifications as suggested in IEC standard.

4.4 Wake Deflection in Yawed Conditions

A new analytical model to predict the wake deflection is derived and validated in Section 4.4.1. The wake model proposed in section 4.2 and 4.3 is extended by incorporating the yaw angle effects in Section 4.4.2. Mean velocity and turbulence intensity predicted by the proposed model are compared with those obtained from the numerical simulations.

4.4.1 Wake Deflection Model

As mentioned by Jimenez et al. (Jiménez et al., 2009), the wake defection can be explained based on the concept of momentum conservation. When the wind turbine axis is not

aligned with the wind direction, the rotor induced thrust forces would add lateral component to the incoming airflow. This lateral force induces a lateral velocity which then causes the wake to deflect towards one side. Jimenez et al. (Jiménez et al., 2009) proposed an analytical model to evaluate the wake deflection based on this concept and the assumption of top-hat for the velocity deficit and the skew angle of the wake deflection as shown in Appendix D. However, this model overestimates the wake deflection since the assumption of the top-hat for the velocity deficit is not accurate as pointed out by Ishihara et al. (Ishihara et al., 2004). Recently, Bastankhah and Porté-Agel (Bastankhah and Porté-Agel, 2016) proposed an analytical model based on the assumption of the Gaussian distribution for the velocity deficit and the skew angle of the wake deflection as described in Appendix E, However, the parameters in this model were not specified.

In this study, the Gaussian distribution function of velocity deficit is used together with the momentum conservation in the lateral direction to derive a new analytical wake deflection model. The model development is shown schematically in Figure 4-13, in which θ is the skew angle denoting the inclination angle of velocity in the wake with respect to the upstream velocity and the wake width D_w is the spanwise distance between the two side boundaries. Similar to the basic approach of Jimenez et al. (Jiménez et al., 2009), the zone denoted by the red dashed lines is the control volume taken into account. It should be noted that to build the control volume, it is necessary to define a specific wake boundary. For simplification, the assumption of top-hat for the skew angle of the wake deflection is adopted and the wake width is defined as a function of ambient turbulence intensity and thrust coefficient, while Bastankhah and Porté-Agel took the assumption of Gaussian distribution for the skew angle. Based on the Gaussian distribution assumption for the velocity deficit, the wake half-width $r_{1/2}$ denotes the location where the velocity deficit equals the half the maximum value, and the velocity deficit normalized by the maximum value at the twice of half-width $2r_{1/2}$ is 0.018. Accordingly, $D_w = 4r_{1/2} = 4\sqrt{2ln2}\sigma$ is used to represent the wake boundary denoted by the black dotted lines downstream the turbine. Here, σ is the representative wake width for a Gaussian distributed velocity deficit in the spanwise direction. In this study, the yaw angle γ is positive in the anti-clockwise direction from the top view, corresponding to the situations where the wind is reaching the turbine from the right side when seen from the turbine.

The turbine induced force exerting on the control volume is supposed to be due only to the velocity component perpendicular to the rotor and it is expressed by the following Equation:

$$F_T = -\frac{1}{2} C_T \rho A_0 (U_0 cos\gamma)^2 \tag{4-31}$$

The projections of this thrust force in streamwise and spanwise directions are expressed as:

$$F_x = -\frac{1}{2} C_T \rho A_0 (U_0 cos\gamma)^2 cos\gamma \tag{4-32}$$

$$F_y = -\frac{1}{2} C_T \rho A_0 (U_0 cos\gamma)^2 sin\gamma \tag{4-33}$$

As shown in Figure 4-13, m_1 is the mass flow crossing the wind turbine, m_2 is the flow entertainment into the wake and m_3 is the mass flow crossing the outlet of the control volume and is expressed as:

$$m_3 = \rho \int U_w dA \tag{4-34}$$

where U_w is the velocity in the wake region.

By taking the momentum conservation in the control volume, the following relationship can be obtained:

$$\vec{F} = m_3 \overrightarrow{u_3} - (m_1 \overrightarrow{u_1} + m_2 \overrightarrow{u_2}) \tag{4-35}$$

The above Equation can be decomposed into streamwise and spanwise components, respectively.

$$F_x = \rho \int U_w^2 cos\theta dA - (m_1 U_0 + m_2 U_0) \tag{4-36}$$

$$F_y = -\rho \int U_w^2 sin\theta dA \tag{4-37}$$

where the skew angle θ is small enough with the approximation of $cos\theta \approx 1$ and $sin\theta \approx \theta$ in the far wake region.

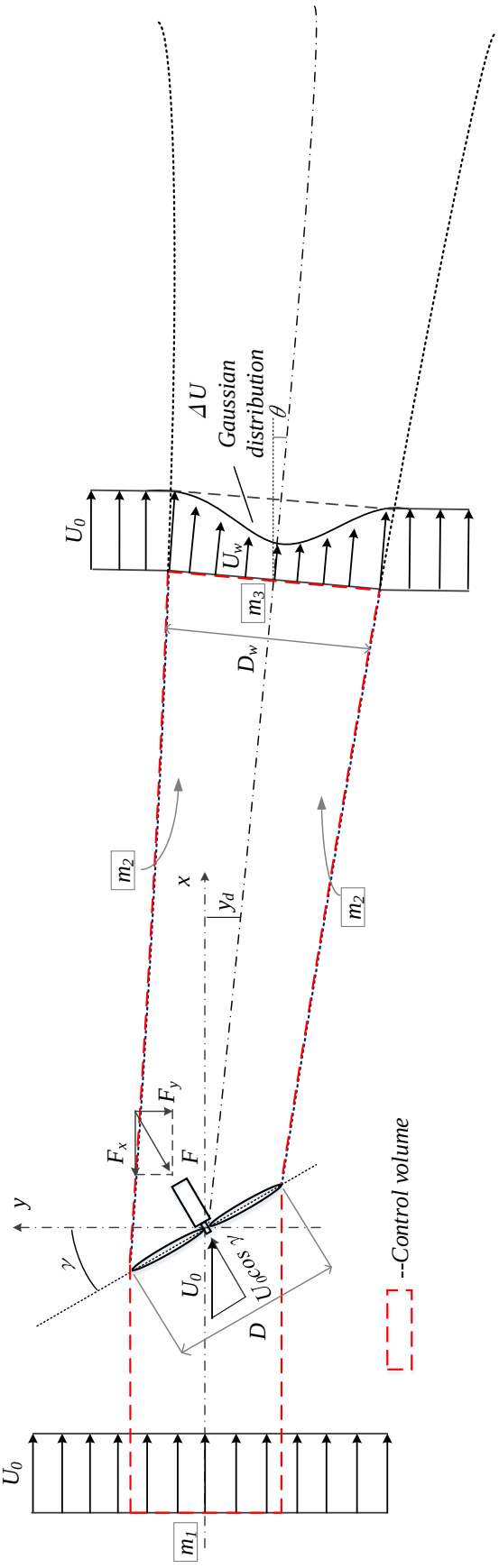

Figure 4-13 Schematic of the momentum conservation-based model for the wake deflection. Black dotted lines downstream the turbine represent the wake boundaries and the part overlapped by the red dashed lines are used to establish the control volume.

From the mass conservation $m_1 + m_2 = m_3$ and substituting Equations (4-32) and (4-34) into Equation (28), the following relation can be derived for streamwise direction:

$$\frac{1}{2}(C_T \cos^3\gamma)\rho A_0 U_0^2 \approx -\rho \int U_w \Delta U dA \tag{4-38}$$

It is not difficult to find that the above Equation has the same form with that under the non-yawed conditions if the transformation of $C_T' = C_T \cos^3\gamma$ is used. Thus, the formula of velocity deficit under the non-yawed conditions is also applicable to that under the yawed conditions, and based on the self-similarity assumption the velocity in the wake region can be expressed as:

$$U_w = U_0(1 - F\varphi) \tag{4-39}$$

where φ and F are the spanwise and streawise functions for velocity deficit. The Gaussian distribution is used for φ:

$$\varphi = exp\left(-\frac{r'^2}{2\sigma^2}\right) \tag{4-40}$$

where r' is the distance from the wake center in the spanwise direction. The streamwise function in the far wake region can be obtained by taking the first order approximation of Taylor expansion for the solution derived by Bastankhah and Porté-Agel (Bastankhah and Porté-Agel, 2014)

$$F=1-\sqrt{1-\frac{C_T'}{8(\sigma/D)}} \approx \frac{C_T'}{16(\sigma/D)^2} = \frac{C_T cos^3\gamma}{16(\sigma/D)^2} \tag{4-41}$$

As mentioned above, the wake deflection is induced by the lateral force component, therefore the momentum Equation in spanwise direction is analyzed to reveal the relationship between them. The skew angle θ is assumed to be constant within the assumed wake boundary. Then by equating Equations (4-33) and (4-37) and taking the approximation of $sin\theta \approx \theta$, the expression of skew angle θ is obtained as:

$$\theta = \frac{-F_y}{\rho \int U_w^2 dA} \tag{4-42}$$

Based on the above assumed wake boundary of $D_w = 4\sqrt{2ln2}\sigma$, the integration in the above Equation (4-42) is calculated in the spanwise direction under a polar coordinate system (Φ, r') with the origin at the wake center as follows:

$$\int U_w^2 dA = U_0^2 \int_0^{2\pi} d\Phi \int_0^{2\sqrt{2ln2}\sigma} (1 - F\varphi)^2 dr' \tag{4-43}$$

By inserting Equations (4-40), (4-41) and (4-43) into Equation (4-42), the skew angle θ can be determined as:

$$\theta = \frac{C_T cos^2\gamma sin\gamma}{44.4(\sigma/D)^2 - 1.88 C_T cos^3\gamma} \tag{4-44}$$

As it is known, the skew angle is the derivative of the wake deflection:

$$\theta(x) = \frac{dy_d(x)}{dx} \tag{4-45}$$

Considering that the above derivation process is just applicable for the far wake region, Equation (4-45) is integrated from an initial far wake location x_0 to find the far wake deflection for $x > x_0$ as:

$$\frac{y_d(x)}{D} = \frac{1}{D}\int_{x_0}^{x} \theta(x) dx + \frac{y_{d0}}{D} = \frac{1}{k^*}\int_{\sigma_0/D}^{\sigma/D} \theta(x) d(\sigma/D) + \frac{y_{d0}}{D} \tag{4-46}$$

where y_{d0} is the wake deflection at $x = x_0$ and dx is replaced by $\frac{1}{k^*} d(\sigma/D)$ based on the expression of σ/D as follows:

$$\sigma/D = k^* x/D \ + \varepsilon^* \tag{4-47}$$

where k^* and ε^* are the parameters with the function of C_T and I_a as shown in the wake model for non-yawed conditions.

Then by substituting Equation (4-42) into Equation (4-46), the final expression for the far wake deflection is obtained as follows:

$$\frac{y_d(x)}{D} = \frac{\sqrt{C_T cos\gamma} sin\gamma}{18.24 k^*} ln \left| \frac{\left(\sigma_0/D + 0.2\sqrt{C_T cos^3\gamma}\right)\left(\sigma/D - 0.2\sqrt{C_T cos^3\gamma}\right)}{\left(\sigma_0/D - 0.2\sqrt{C_T cos^3\gamma}\right)\left(\sigma/D + 0.2\sqrt{C_T cos^3\gamma}\right)} \right| + \frac{y_{d0}}{D} \tag{4-48}$$

To complete the above model, the values of x_0 and y_{d0}/D also need to be determined. In this study, the wake deflection in the near wake region for $x \leq x_0$ is also assumed to be linear with the distance, and is expressed by:

$$\frac{y_d(x)}{D} = \theta_0 \frac{x}{D} \tag{4-49}$$

where θ_0 is the initial skew angle and it can be determined based on the approach of Coleman et al. (Coleman and Feingold, 1945):

$$\theta_0 = \frac{0.3\gamma}{\cos\gamma}\left(1 - \sqrt{1 - C_T \cos^3\gamma}\right) \tag{4-50}$$

Note that the apparent difference between Equation (4-50) and the original formula is due to the different definition of thrust coefficients as shown in Equation (3-7).

For the value of x_0 and σ_0, Bastankhah and Porté-Agel (2016) derived the onset of the far wake region based on the idealized potential core analysis. In this study, a simple method to find the value of x_0 and σ_0 is derived from the mathematical viewpoint. The wake skew angle predicted in the near and far wake region should have the same value at the joint location, i.e., x_0. Thus, by equating Equations (4-44) and (4-50), the value of σ_0 can be directly obtained as:

$$\frac{\sigma_0}{D} = \sqrt{\frac{C_T cos^2\gamma(sin\gamma + 1.88cos\gamma\theta_0)}{44.4\theta_0}} \tag{4-51}$$

The value of x_0 can be calculated based on Equation (4-47) as follows:

$$\frac{x_0}{D} = \left(\frac{\sigma_0}{D} - \varepsilon^*\right)/k^* \tag{4-52}$$

As noted by Bastankhah and Porté-Agel (2016), the above estimation of x_0 does not aim to accurately predict the near wake length, but give an initial value for the far wake model.

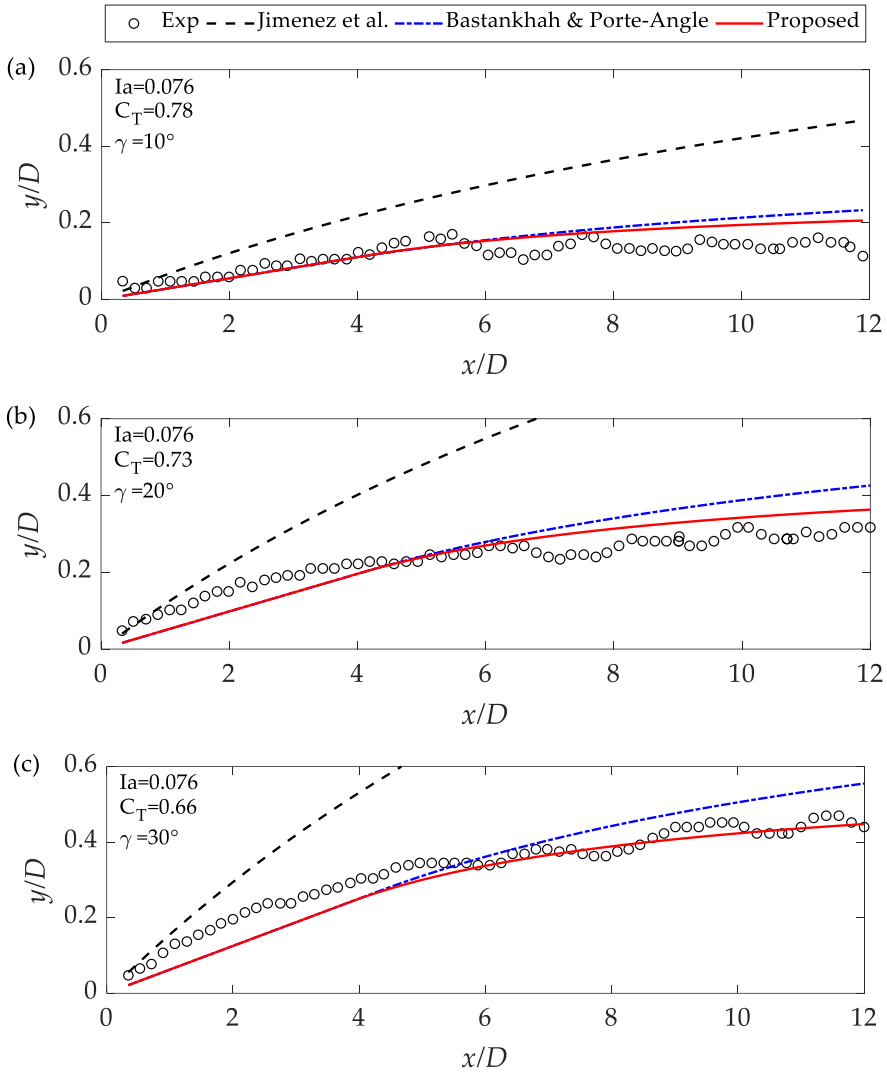

Figure 4-14 Comparison between wake deflection models and the experiment results.

Table 4-3 NRMSE of predicted wake deflections.

Model	$C_T = 0.78, \gamma = 10°$	$C_T = 0.73, \gamma = 20°$	$C_T = 0.66, \gamma = 30°$
Jiménez	1.38	1.16	0.94
Bastankhah and Porté-Agel	0.31	0.23	0.13
Proposed	0.29	0.20	0.11

Figure 4-14 shows the comparison between the wake center trajectories obtained from the experiment by Bastankhah and Porté-Agel (2016) and those predicted by the models. In addition, the NRMSE of predicted result respect to the experimental data for each model

are summarized in Table 4-3, in which the mean value of deflections from experimental data in the far wake region ($x/D > 10$) is used for the normalization. Note that the corresponding C_T shown in the figure for each case need to be replaced with $C_T/\cos^2\gamma$ for the calculation of Jiménez's model and the proposed model since the thrust coefficient $C_T = F_T/(0.5\rho A_0 U_h^2)$ defined by Bastankhah and Porté-Agel (2016) is different from Equation (3-7). It is found that, the Jiménez's model generally overestimates the wake deflections. The proposed model denoted by solid red lines and the Bastankhah and Porté-Agel's model plotted by blue dashed lines show good agreement with the experimental data. The parameter $k_y = k_z = 0.022$ from the experimental data fitting is used for the Bastankhah and Porté-Agel's model.

4.4.2 Wake Model for Yawed Wind Turbines

Figure 4-15 shows the schematic of wake model under yawed conditions for the velocity deficit and added turbulence intensity, in which U_0 and I_0 denote the upstream mean velocity and turbulence intensity. In order to incorporate the yawed condition into the wake model proposed in section 4.2, two basic assumptions are used in this study. One is to assume that the Gaussian distribution and self-similarity are applicable for the velocity deficit and added turbulence intensity distributions in cross-section of wake, and the other is to assume that the turbulence intensity distributions have the same wake deflections as those for the velocity deficit at each downwind location. Based on these assumptions, the wake model for the non-yawed wind turbines is modified for the velocity deficit and added turbulence intensity prediction under yawed conditions:

$$\Delta U(x,r)/U_0 = F(C_T', I_a, x/D)\phi(r'/\sigma) \tag{4-53}$$

$$\Delta I_1(x,r) = G(C_T', I_a, x/D)\varphi(r'/\sigma) \tag{4-54}$$

where the C_T' is the trust coefficients under the yawed condition and r' is the distance from the wake center in the spanwise direction. They need to be replaced by the following expressions as mentioned at Section 4.3.1:

$$C_T' = C_T \cos^3\gamma \tag{4-55}$$

$$r' = \sqrt{(y + y_d)^2 + (z - H)^2} \tag{4-56}$$

The parameters used in the wake model proposed in section 4.2 are shown in Table 4-2. Figure 4-16 shows the deflected wake center trajectories under the different conditions, in which the open circles denote the numerical results. The predicted values by Jimenez's model and the proposed model are plotted by black dashed lines and red solid lines, respectively. The model of Bastankhah and Porté-Agel is not plotted since the parameters k_y and k_z have not been specified. It is noticed that the proposed model shows good agreement with the numerical results, however, the Jiménez's model overestimates the deflections especially for the cases with the large thrust coefficients. In addition, it is clearly observed that the wake deflections increase almost linearly in the near wake region and then grow slowly in the far wake region. The slopes, i.e., wake skew angles are almost same for the cases with the same C_T and under the same yaw angles. This justifies that Equations (4-49) and (4-50) are suitable for the initial wake deflection prediction by assuming a constant initial skew angle which just depends on the C_T and the yaw angle γ. The high ambient turbulence generally decreases the length of potential core region and accelerates the flow mixing in the far wake region, whereby the wake deflections decrease. It can be inferred that the yaw control strategy is more efficient under low ambient turbulence such as in offshore wind farms.

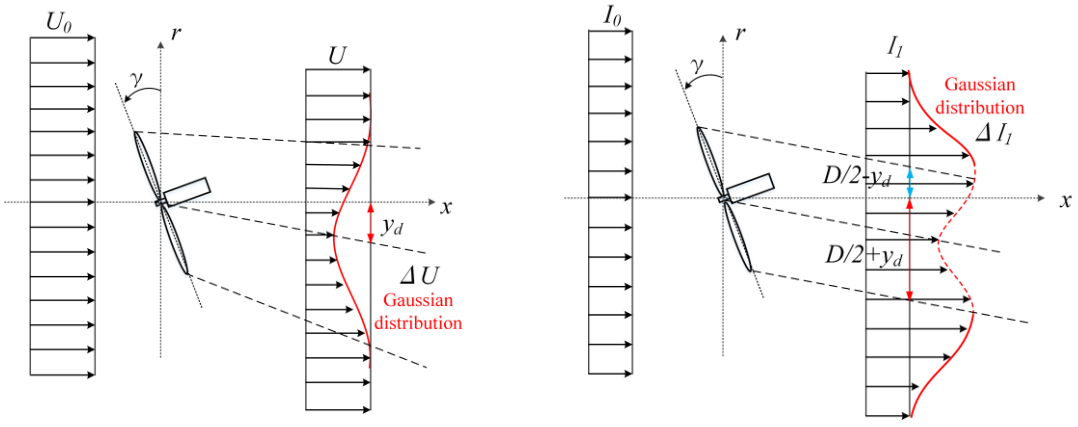

(a) mean velocity (b) turbulence intensity.

Figure 4-15 Schematic of the Gaussian-based wake model in yawed condition:

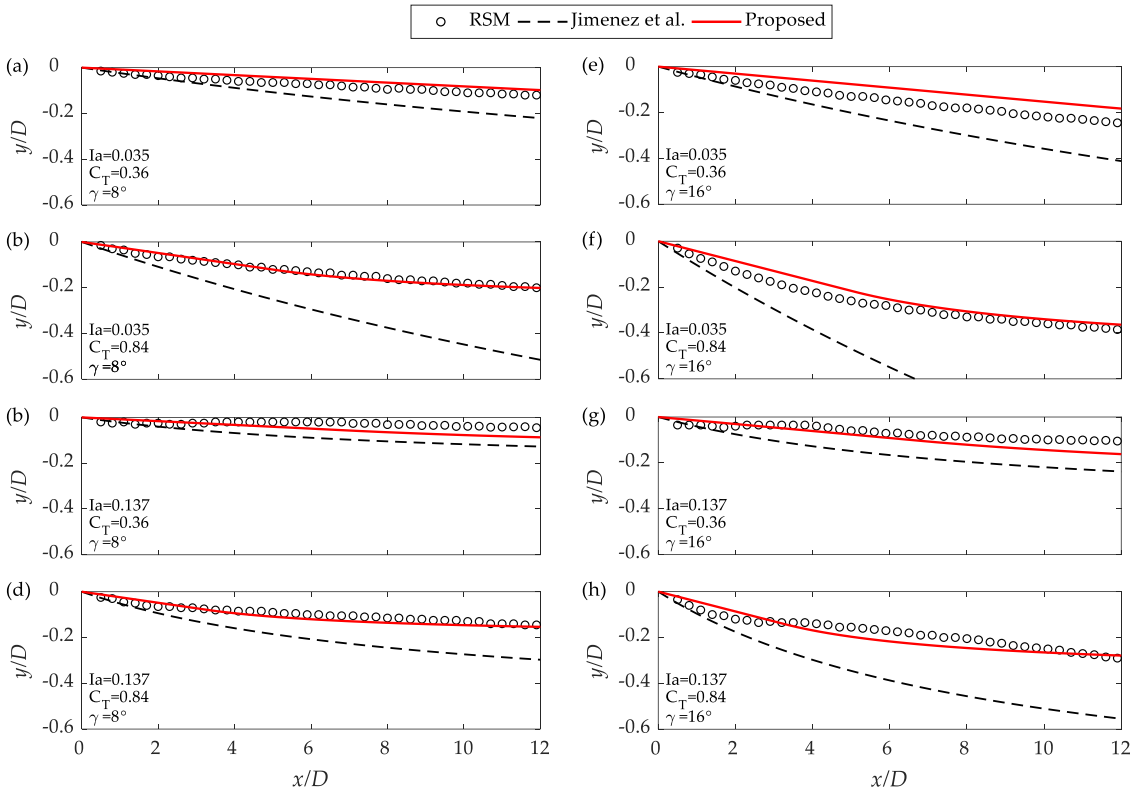

Figure 4-16 Validation for predicted wake deflections in yawed conditions.

Figures 4-17 and 4-18 show comparisons between the simulation results and the wake models for mean velocity and turbulence intensity, respectively. In these figures, the horizontal profiles of the normalized mean velocity and turbulence intensity at selected downwind locations of x =2D, 4D, 6D, 8D, 10D and 12D are plotted. The numerical results are shown by the open circles and the red solid lines denote the results predicted by the proposed model. The x-axis illustrates the distance from the wind turbine normalized by the rotor diameter D. The distance of 2D corresponds to a unit scale of normalized mean velocity U/U_h in Figure 4-17 and a scale of turbulence intensity with the value of 0.3 in Figure 4-18, respectively. In Figure 4-17, the mean velocity predicted by the Jiménez's model is also plotted by black dashed lines for comparison. The velocity deficit for this model is calculated with the top-hat model proposed by Katic et al. (1986):

$$\frac{\Delta U}{U_h} = \frac{1-\sqrt{1-C_T\cos^3\gamma}}{(1+2k_w x/D)^2} \tag{4-57}$$

where k_w is the wake decay factor and the recommended values is $k_w = 0.4I_a$ for the flat terrain under the neutral conditions (Peña et al., 2016).

As shown in Figure 4-17, the proposed model gives more accurate predictions for the mean velocity distributions under the different yawed conditions than those by the top-hat shape used in the Jimenez's model, which underestimates the velocity deficit in the center of the wake and overestimates them in the outside regions.

Since the turbulence intensity prediction was not included in the previous wake models proposed by Jimenez et al. (2009) and Bastankhah and Porté-Agel (2016), only turbulence intensities by the proposed model in this study are plotted for comparison with the numerical results. As shown in Figure 4-18, the proposed model satisfactorily predicts the turbulence intensity distribution in the wake of yawed turbines. It is noticed that the predicted mean velocity and turbulence intensity distributions in the spanwise direction are assumed symmetric to the wake center trajectory, while the profiles of mean velocity and turbulence intensity from the numerical simulations present slightly skewed shape as shown in Figures 4-17 and 4-18.

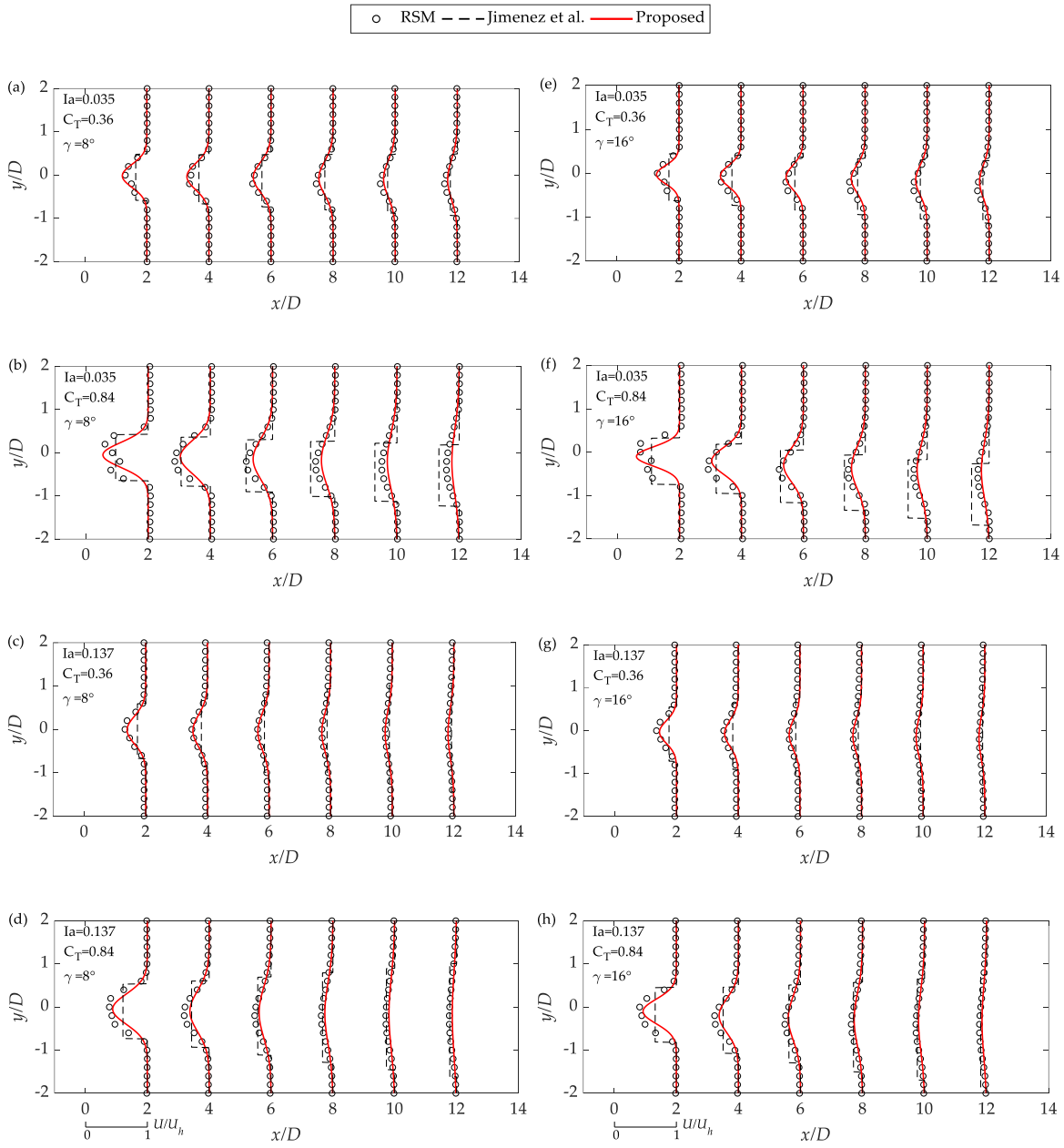

Figure 4-17 Validation for the predicted mean velocity under the yawed conditions.

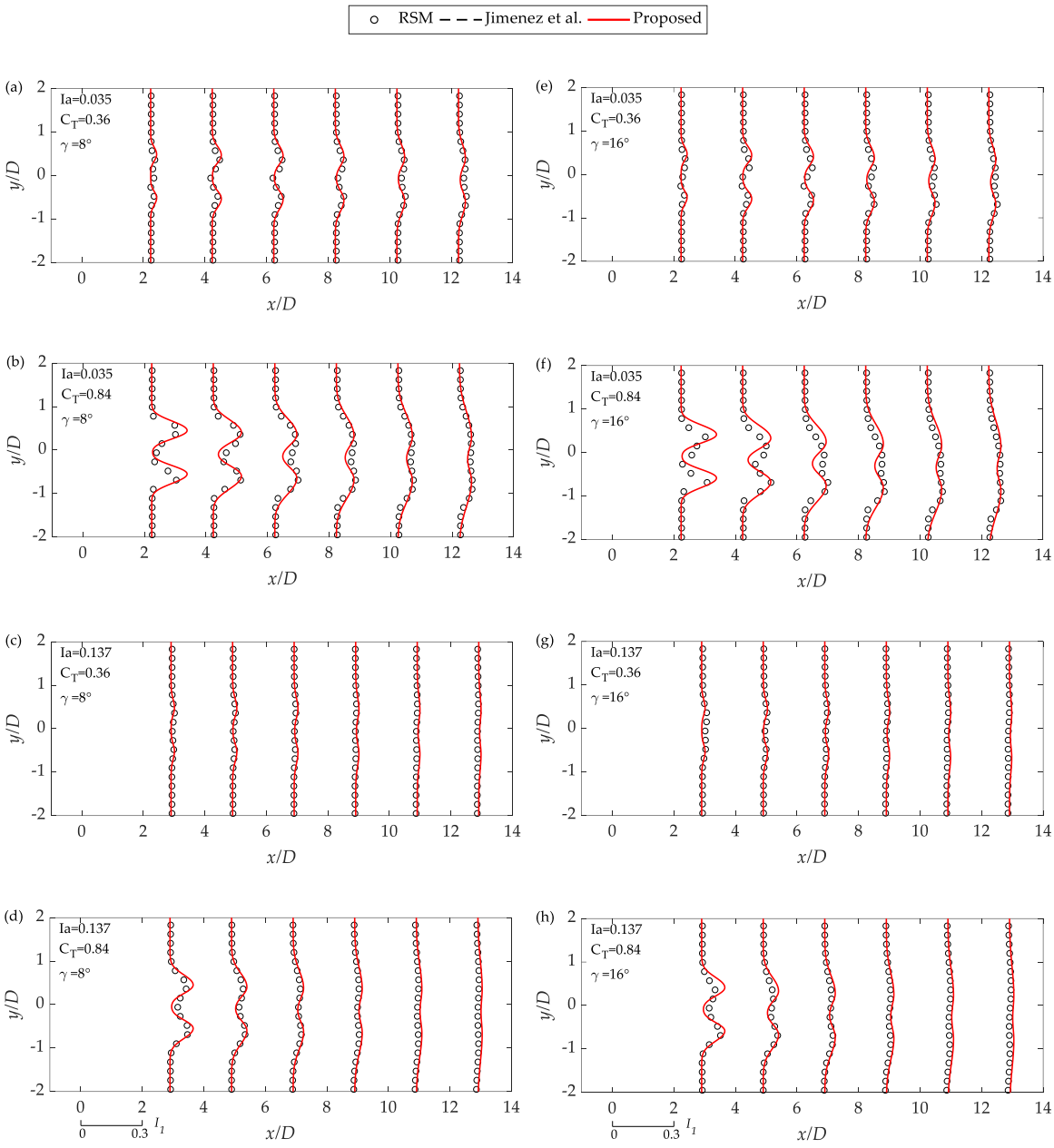

Figure 4-18 Validation for the predicted turbulence intensity under the yawed conditions.

4.5 Summary

A new Gaussian-based wake model is proposed based on systematic analysis of the ambient turbulence intensity and the thrust coefficient effects on the wake flow. Then a new analytical model for wake deflection is developed based on the theoretical analysis of turbine induced force and the momentum conservation for a control volume around the yawed turbine. The proposed wake deflection model is incorporated into the Gaussian-based wake model to predict the mean velocity and turbulence intensity in the wake region. Following conclusions are obtained:

1. A new Gaussian-based wake model is proposed to predict the mean velocity deficit and added turbulence intensity in the near and far wake region. The proposed model shows good performance for prediction of maximum values as well as distributions of mean velocity and turbulence intensity under various ambient turbulence and thrust coefficient conditions.

2. The applicability of the Frandsen's model used in IEC61400-1 and the proposed model for the local turbulence intensity prediction in the wake region are investigated. The proposed model provides more accurate predictions, while Frandsen's model shows conservative results in the near wake region.

3. A new analytical wake deflection model is proposed based on the Gaussian distribution for velocity deficit and the top-hat shape for skew angle and it is validated by comparison with the results obtained from the wind tunnel test and the numerical simulations. The model parameters are determined as the function of ambient turbulence intensity and thrust coefficient, which enables the model to have good applicability under various conditions.

4. The proposed Gaussian based wake model is later updated for yaw wind turbines by incorporating the proposed wake deflection model to consider the yaw angle effects, which shows good performance for predicting distributions of mean velocity and turbulence intensity by comparison with the numerical results.

Chapter5. Application in Real Wind Farm over Complex Terrain

5.1 Introduction

This chapter aims to address the subject of wind turbine wakes over the complex terrain and to validate the developed numerical framework and analytical wake model in real wind farms. The numerical model including the DDES framework, canopy model, and wind turbine model has already been presented in Chapter 2. Firstly, the comprehensive field measurement conducted in the test site is introduced in section 5.2. Next, the setup of the simulation cases is described in section 5.3. In section 5.4, firstly the built numerical framework is validated by the comparison of the predicted wind field and turbine wake flow over the terrain with measurements. Then the escarpment induced terrain effects on the turbine wake flow are systematically investigated. Further, the applicability of a new wake model in complex terrain is verified by the numerical results. Conclusions of this study are summarized in section 5.5.

5.2 Field Measurement

5.2.1 Target Site

As shown in Figure 5-1, a test site in the Tomamae wind farm, located in Hokkaido facing the Japan Sea, is considered. One of the prominent topographic features of this site is a

(a) Location of Tomamae

(b) Photography of test site

(c) Layout of wind turbines, LiDAR, Met-masts, and surrounding terrains

Figure 5-1 Test site in the Tomamae wind farm

steep escarpment along the west coast, up to around 40 m above sea level. In addition, the east side are continuous mountainous areas with approximate 180 m altitude. This coast

onshore site is mainly characterized by the ranch, farmland, grass, and nearby buildings and forests, which adds to the complexity of the land surface roughness. There are totally 20 wind turbines (WT01 ~ WT20) in this local site. Comprehensive measurement campaigns were carried out successively in the Tomamae wind farm, including a ground-based vertical profile LIDAR, three Met-masts equipped with anemometers and wind turbine SCADA data, as shown in the whole wind farm layout (Figure 5-1 c).

5.2.2 LiDAR Data

A ground-based Light Detection and Ranging (LiDAR) system, WindCube V2 was set at the northwest side close to the escarpment edge, approximately 68 m from the No.3 wind turbine (WT03). The WindCube V2 is a pulse Doppler LiDAR that emits short pulses of laser energy to measure radial wind speed. The time series of the returned signal is then split up into blocks that correspond to range gates and processed to estimate the averaged

(a) Photography of the LiDAR

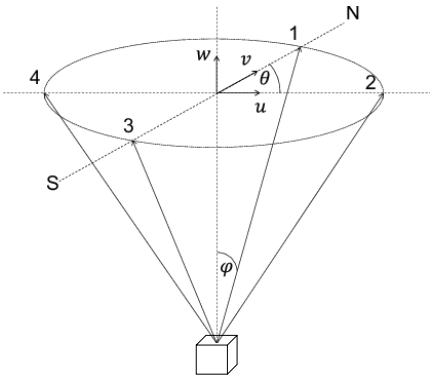

(a) Scetch of DBS strategy

Figure 5-2: Vertical Profile LiDAR in the test site

Table 5-1 Specification of LiDAR system

Measurement period	2015/11/4 ~ 2016/1/27
Type of machine	WindCube V2
Measured height	40m ~ 220m (every 20 m)
Velocity resolution	0.1 m/s
Time sampling resolution	1 s
Time-averaged period	10 min
Data availability	93.5% (40.0 m)

radial wind speed at each range gate (Huffaker and Hardesty, 1996). As shown in Figure 5-2 (c), the Doppler beam swinging (DBS) technique is utilized to measure the horizontal wind speed at each height. An optical switch points the lidar beam in four cardinal directions (north, east, south, and west) at a cone angle of 28°, plus a vertically pointing beam to obtain the vertical velocity. The velocity algorithm calculates the u, v, and w components every second using the current radial velocity and the those obtained from previous three beam locations (Pena et al .2015). The basic specification parameters are summarized in Table 5-1. The wind speed at different height were measured simultaneously and statistical data in every 10 minutes were also automatically recorded.

5.2.3 Wind Turbine and SCADA Data

(a) Utility-scale wind turbine

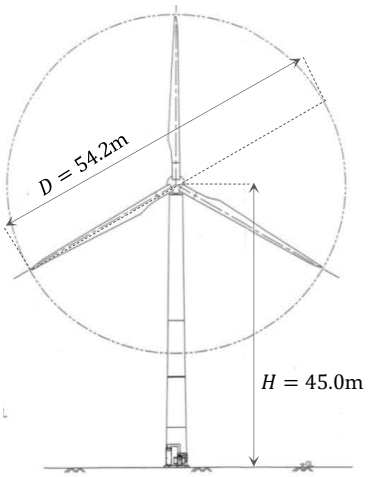

(b) Dimensions of wind turbine

Figure 5-3 1MW wind turbine in Tommae wind farm

Table 5-2 Specification of Wind turbine

Manufacturer	Bonus-Energy A/S (Simens Wind Power A/S)
Rated power generation	1000/kW
Rated rotor speed	21/14rpm
Rotor diameter	54.2m
Hub height	45m
Cut-in wind speed	3m/s
Rated wind speed	15m/s
Cut-out wind speed	25m/s

In this campaign, a Bonus B54/1000 1MW wind turbine in the Tomamae wind farm is considered to study the wakes in complex terrain. The Bonus B54/1000 is a stall-regulated turbine with a rotor diameter of D=54.2 m and a hub height of H=45.0 m. The basic specification of the wind turbine is summarized in Table 5-1. The wind turbine is instrumented with a Supervisory Control and Data Acquisition (SCADA) system for recording meteorological properties (wind speed, wind direction etc.) and also the turbine operational conditions (electric active power, turbine rotational speed, yaw angle etc.). In this campaign, the 10 min time-averaged SCADA data covers the period from Nov 12th, 2015 to Jan 27th, 2016.

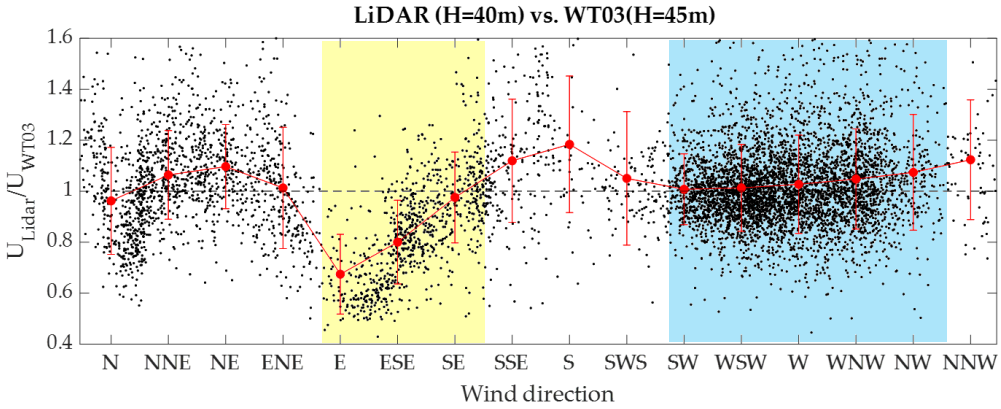

Figure 5-4 Comparison of LiDAR data and SCADA data

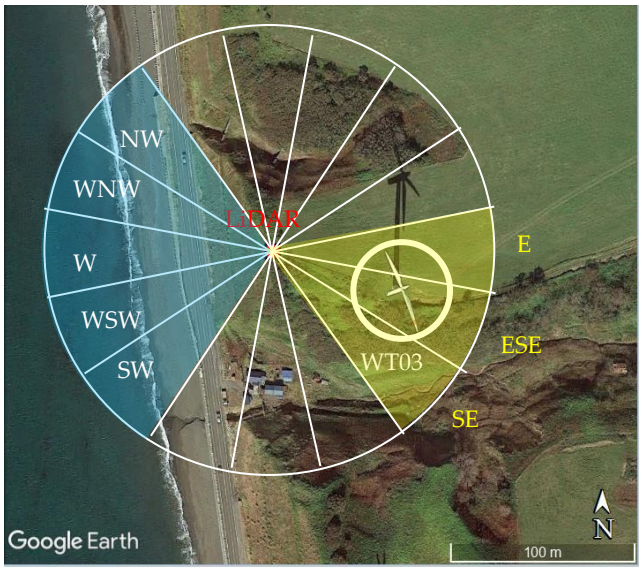

Figure 5-5 Schematic of wind sector division at the location of LiDAR

Figure 5-4 shows the comparison of LiDAR data and SCADA data obtained from WT03, where U_{LiDAR} is the wind speed measured by LiDAR at the height of H=40m, U_{WT03} is the wind speed at the WT03 hub height. Black dots denote the ratio of wind speed at those two locations, and the red slid circles are the bin averaged values for each wind direction with the sector range of 22.5°. Firstly, it can be seen that the wind speed obtained from LiDAR and SCADA are quite close for NW, WNW, W, WSW and SW directions, where the wind blow from the sea side. Since the LiDAR and WT03 are quite close and just in the coast line, the wind speed at the level of 40m from ground are less affected by the local terrain. However, in the wind directions of E, ESE and SE, there is an obvious velocity deficit of LiDAR compared with the velocity from SCADA, which is mainly induced by the wind turbine wake from WT03. As also can be clearly identified from Figure 5-5, the LiDAR is in the wake region, when the incoming wind is from E, ESE and SE these directions.

Wind field in this coastal area is extremely complex as the atmospheric features vary with different wind direction. Measurement in the wind farm are not only essential for the maintenance but also can provide very valuable information of the wind field. The LiDAR data and wind turbine SCADA data would be used in this study for the validation of the numerical wake modelling.

5.3 Numerical Setup

5.3.1 Configuration of the Numerical Wind Tunnel

As shown in Figure 5-6, the numerical wind tunnel is built by the dimensions of 18km×18km×2km (streamwise direction, spanwise direction and vertical direction) with a scale of 1:2000. The height of domain is determined by limiting the blockage ratio to a specified value. 5% is often considered to be an acceptable limit of blockage ratio for a wind tunnel experiment (Fujino, et al. 2012). Considering the average elevation in the current considered site is lower than 100 m, 2 km is adopted as the calculation domain height. The range of complex terrain is determined as 4 km based on an iteration procedure, as recommended by Qi (2016). In the inflow generation zone, roughness blocks are placed

7km upstream from the origin, following the experiment setup by Yamaguchi et al. (2003). It is used to simulate the neutrally stratified atmospheric boundary layer in the ocean side with the mean velocity profile following the power law α=0.1. For the land side, the boundary layer would be automatically developed through the surrounding terrain and forests within the considered region as performed by Liu et al. (2016). As The location of LIDAR is set as the origin of the computational domain for wind flow and wake flow simulation cases for WT03. And then the origin was moved to No. 4 wind turbine (WT04), which is close to the escarpment edge, to investigate the escarpment effects on wake flow of WT04.

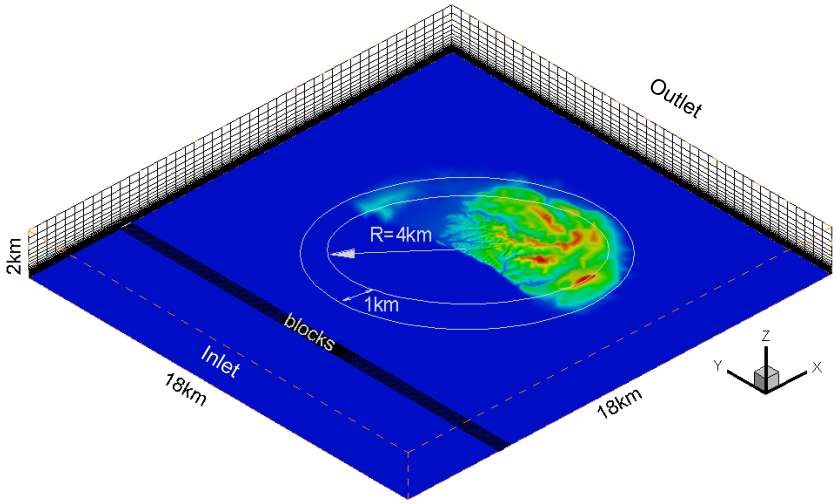

(a) Global view of the domain

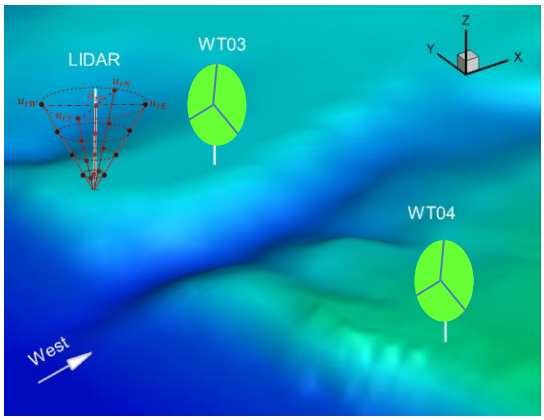

(b) Local view of the terrain near the WT03, WT04, and LiDAR

Figure 5-6 Configuration of the numerical simulation domain

5.3.2 Topography and Roughness Database

The topography model with a scale of 1:2000 and a radius R=4km is generated based on the digital elevation model (DEM), as shown in Figure 5-7. The DEM database used in this research is provided by the Geospatial Information Authority of Japan in raster format, which describes the topography in whole Japan with an available minimum resolution of 10m×10m. When modelling topography in numerical simulations, a two-dimensional interpolation method combines triangle-based linear and cubic interpolations is utilized to calculate the elevation of topography at grid nodes in the bottom boundary in numerical simulations.

$$h_{node} = \begin{cases} h_{node}^{cubic} & \min(h_{DEM,i}) \le h_{node}^{cubic} \le \max(h_{DEM,i}) \\ h_{node}^{linear} & else \end{cases}, \quad i = 1,2,3,4 \tag{5-1}$$

where the h_{node} is the elevation of topography at grid nodes in bottom boundary. h_{node}^{linear} and h_{node}^{cubic} are calculated elevation from DEM by using triangle-based linear and cubic interpolation methods, respectively. $h_{DEM,i}$ are elevations of closest surrounding four locations from DEM. In addition, the outer ring with width of 1km is used to smooth the surrounding terrain.

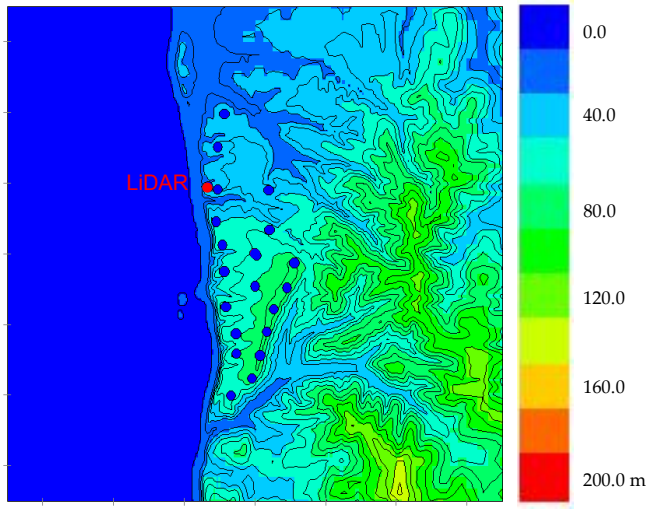

Figure 5-7 DEM database in Tomamae wind farm

The Ministry of Land, Infrastructure, Transport and Tourism of Japan (MLIT) classified all land-use conditions into 11 categories and provided corresponding roughness length z_0 for each category. In consideration of the buildings and forest are dominant surface roughness conditions and can strongly affect above flow fields, therefore canopy model described in section 2.3.2 is applied. The distribution of the vegetation and buildings are obtained from the database provided by the National Land Numerical Information of Japan and then locally modified based on the Google map as shown in Figure 5-8. The average height of forest is set as 13.3m for the canopy layers with the parameters determined based on the procedure proposed by Enoki and Ishihara (2012).

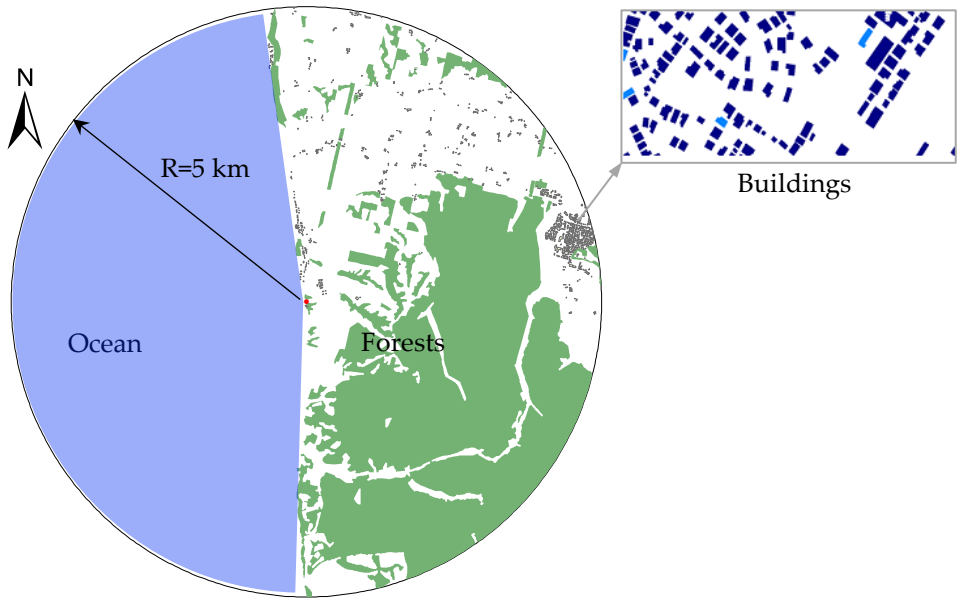

Figure 5-8 Roughness database in Tomamae wind farm

5.3.3 Grid System

For the sake of reducing calculation cost as well as keep prediction accuracy, a hybrid grid system is designed as shown in Figure 5-9. Fine grid with the horizontal resolution of 2m in horizontal direction is used for the turbine zone to capture the detailed turbulence features in the turbine wake region. An additional zone is horizontally a square centered

at the origin with side length of 2km and resolution of 8m to consider the effects from the closely surrounding terrain and vegetations. Relative coarse grid resolution is used in the buffer zone. Besides, additional upstream buffer zone was appended in front of roughness blocks to avoid perturbations from the inlet condition. The σ grid system is applied to modify the vertical coordinate of grid nodes above the topography, which means keeping the ratio of the vertical size of adjacent grids unchanged. The vertical grid size of the first layer is set as 0.4 m in real scale with a growing ratio of 1.15. Numerical simulations for different wind direction were performed using the same grid system, as implemented like the turn table in wind tunnel, which means the coordinated of the terrain were rotated when the wind direction was changed.

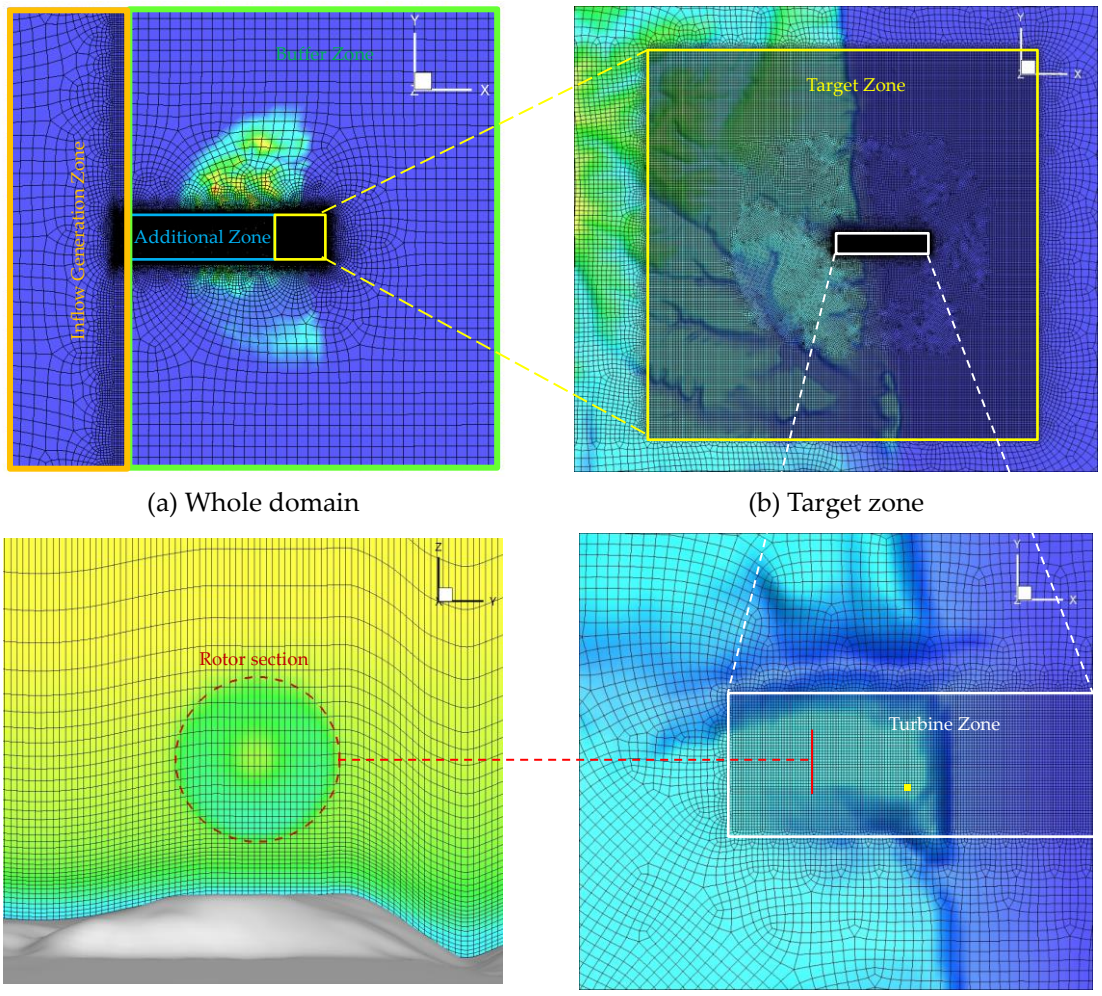

(a) Whole domain (b) Target zone

(c) Rotor section (d) Turbine zone

Figure 5-9 Hybrid grid system of computational domain

5.3.4 Boundary Condition and Solution Scheme

Finite volume method is employed in this study and the simulations are performed with a modified DDES model (see section 2.1.3). The effect of the rotor induced forces on the flow is parameterized by using the coupled BEM-CFD approach described in section 2.2.1, in which the lift and drag forces are calculated based on the blade element theory and then unevenly distributed on the actuator disk.

The central difference scheme is applied for the interpolation of velocities and second order upwind scheme is used for the turbulent kinetic energy and dissipation rate. SIMPLE algorithm is employed for solving the discretized Equations. Boundary conditions used in the numerical simulations are summarized in Table 5-3. A stress-free condition ($\partial u/\partial n = 0$, $\partial v/\partial n = 0$, $w = 0$) was used at the top of the domain and a symmetry condition ($\partial u/\partial n = 0$, $\partial w/\partial n = 0$, $v = 0$) at the spanwise sides. Uniform wind flow with a speed of 10m/s was set at the inlet ($p = 0$, $u = 10$ m/s, v=0, w=0). At the end of the tunnel, outflow condition is applied ($\partial p/\partial n = 0$, $\partial u/\partial n = 0$, $\partial v/\partial n = 0$, $\partial w/\partial n = 0$). The wall-stress boundary condition is imposed at the ground surface with the roughness height z_0=0.0002m for ocean area and z_0=0.03m for land area, respectively.

Table 5-3 Boundary conditions in simulations on steep terrains

Boundary	Setting
Inlet Boundary	Velocity inlet
Outlet Boundary	Outflow
Side Boundary	Symmetry
Top Boundary	Stress-free
Bottom Boundary	Logarithmic law

5.4 Numerical Results and Discussion

5.4.1 Wind Flow over Complex Terrain

To verify the accuracy of the modified DDES model and the boundary conditions described above, wind flow in the boundary layer without turbines is predicted and compared with

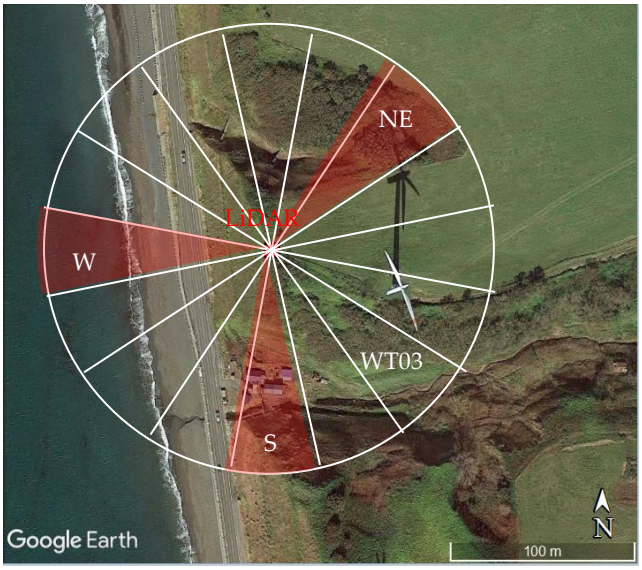

Figure 5-10 Schematic of wind flow simulation cases for LiDAR at W, NE, and S directions

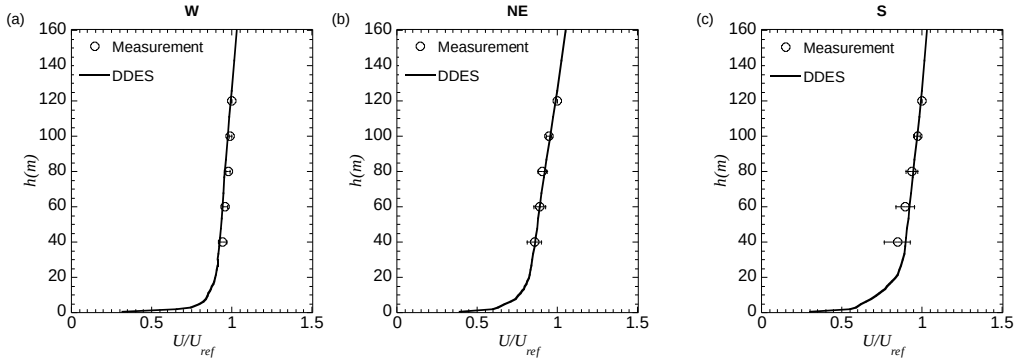

Figure 5-11 Comparison between predicted and measured wind flow at the location of LIDAR: (a)West wind direction, (b) North-East wind direction, (c)South wind direction

the measurements. As shown in Figure 5-10, three representative wind directions (West, North-East and South) were chosen to perform the wind flow simulation, where the LIDAR is not in the wind turbine wake region. The vertical profiles of the mean wind speed at the location of LIDAR in these three wind directions are shown in Figure 5-11, in which the mean velocity is normalized by the referred value U_{ref} at the height of 120m. The error bars in the measurements show the standard deviations of the averaged values. An obvious difference of the gradient of the velocity profile is found in these three directions since the terrain and surface roughness vary with the wind directions. In W direction, there is a speed up at the low elevation over the escarpment, as a result the vertical profile is almost

straight with quite low gradient. In general, the numerical results show favourably good agreement with the measurements for each wind direction and validate the developed numerical model simulating the turbulent flow over the terrain covered by vegetations.

5.4.2 Wake Flow over Complex Terrain

Once the CFD solver has been validated for complex terrain flows, the next is to validate the built wind turbine model. As the LIDAR is located with the distance of 1.4D from the No.3 wind turbine, it is significantly affected by the wake. Numerical simulations of the wake flow over the terrain are performed for WT03 in three representative wind directions: East, East-South-East and South-East. Note that for each wind direction simulation, the rotor rotational speed is kept 21 RPM, which is same as the real situation. Figure 5-12 shows the resolved mean velocity distribution in vertical and horizontal directions, in which it can be clearly identified that the relative positions between the wind turbine rotor and LiDAR change with wind directions. The wake regions in these three cases are quite short, since the ambient turbulence is relatively strong when the wind is from the land side.

Figure 5-13 presents a quantitative comparison for the mean velocity profile extracted at the DDES simulation with those obtained from the measurement. Since the wake behavior are directly related with the turbine operation condition, the plotted mean wind speeds by LIDAR are bin averaged values with the criteria of $U_{SCADA} \pm 0.5$m/s, where the U_{SCADA} is the mean wind speed measured by the SCADA of WT03. The reference mean wind speeds U_{ref} at the height of 120m are used for normalization. The error bars in the measurements show the standard deviations of the averaged values. A significant deceleration of the wind flow is observed in the turbine rotor area because of the extracted energy by the wind turbine. In E and SE, the positions of LiDAR are closely located at the edge of wake region, while in ESE direction LiDAR beams are almost emerged in the wake, resulting in stronger velocity deficit compared with those in E and SE. It is clearly observed that, the velocity deficit and distribution in these three wind directions are well reproduced, which implies that the wind turbine model is developed with good accuracy. The velocity is slightly overestimated around the hub height for ESE, which is likely due to the effect of the nacelle, which was not modelled in the simulations.

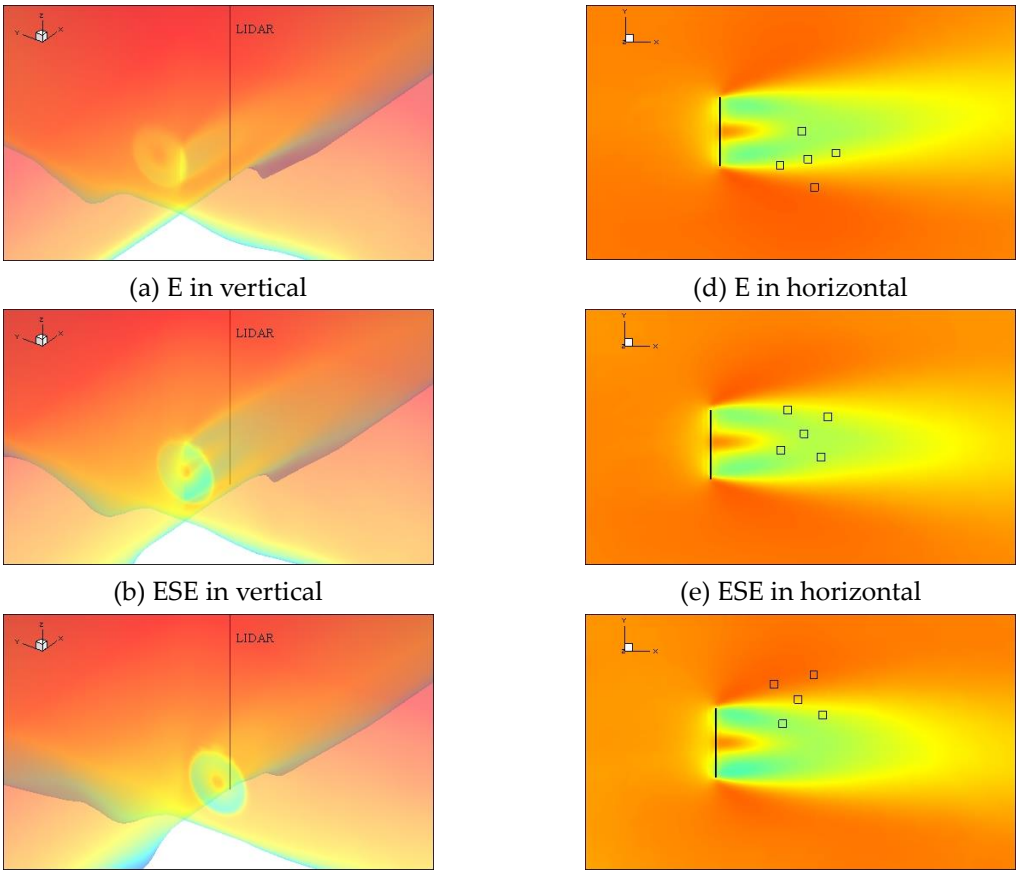

(a) E in vertical (d) E in horizontal

(b) ESE in vertical (e) ESE in horizontal

(c) SE in vertical (f) SE in horizontal

Figure 5-12 Contours of mean velocity distribution in different wind direction: (a), (b) and (c) shows contours in the vertical plane of rotor section and the plane of y=0 through the LiDAR denoted by a vertical solid line; (d), (e), and (f) presents the contours in the horizontal plane with the height of H=40 m from ground, where the open squares mark the beams positions of LiDAR

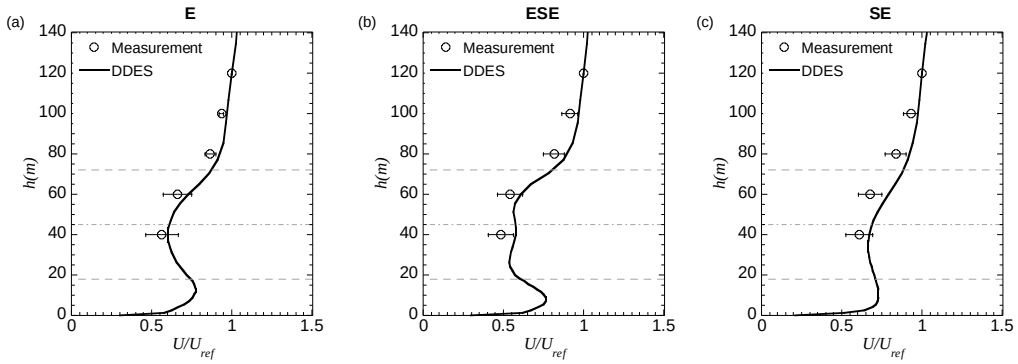

Figure 5-13 Comparison between predicted and measured wind turbine wake flow at the location of LIDAR for normalized mean streamwise velocity. The two dashed lines mark the turbine bottom and top tips, dot-dashed lines show the hub height position. The averaged hub height wind speed are 8.5m/s, 7.5m/s, and 6.5m/s for E, ESE, and SE.

5.4.3 Terrain Effects on the Wind Turbine Wake

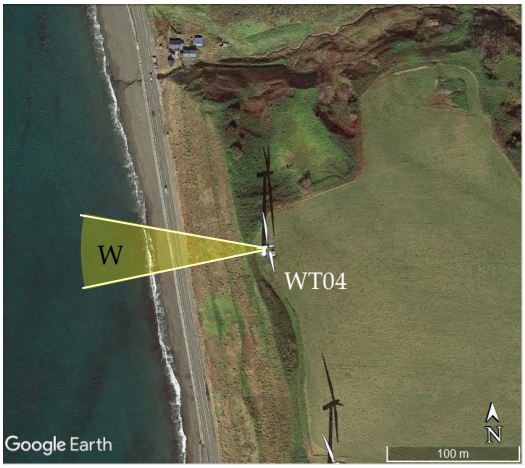

Figure 5-14 Schematic of wake simulation cases for WT04 in W direction

The escarpment is one of the most representative types of terrain in the coastal region of Japan. Therefore, it would be of great meanings to systematically investigate such kind of terrain effects on the wind turbine wakes. As shown in Figure 5-14, the No. 4 wind turbine (WT04), sited close to the edge of the escarpment, are chosen for numerical investigation with the incoming wind direction of West.

Two different terrain heights are considered with the scale ratios of H_{hill}/H_{hub}=0.9 for low escarpment and H_{hill}/H_{hub}=3.6 for high escarpment case, respectively, where H_{hill} is the local elevation at the turbine location. Note the original slope of the terrain is kept for these two cases. Firstly, the CFD simulations are carried out without the turbine to examine the wind flow features over the escarpment. Figure 5-15 shows the mean velocity distribution over the escarpment. There is an obvious speed up over the edge of the escarpment as expected. In addition, the wind direction changes in the vertical direction with the inclination angle regards to the wind turbine. It is noticed that in the horizontal direction, the wind direction was shifted to the left side, which is due to the fact that the edge of the escarpment is not regularly perpendicular to the wind direction. Figure 5-16 presents the distribution of the inclination angle and yaw angle extracted at the hub height, where $x/D = 0$ represent the location of wind turbine. Generally, the terrain induced inclination and yaw angle are larger over the higher escarpment. The inclination angle decreases

rapidly in the downwind regions, whereas the yaw angle decreases slowly.

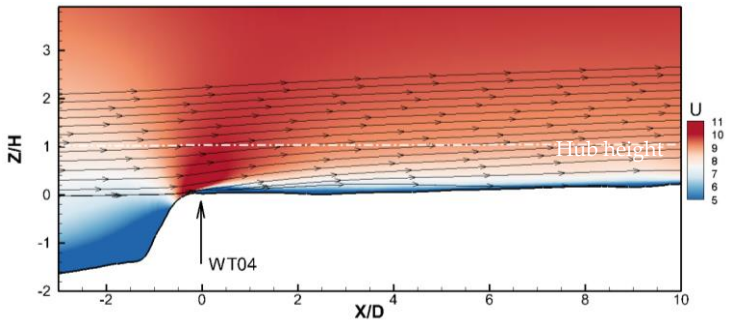

(a) vertical direction: x-z plane through the WT0$

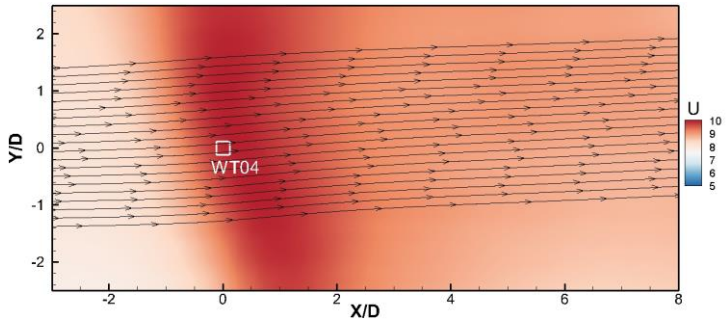

(b) horizontal direction: x-y plane at the hub height

Figure 5-15 Mean velocity contours and streamlines over the escarpment

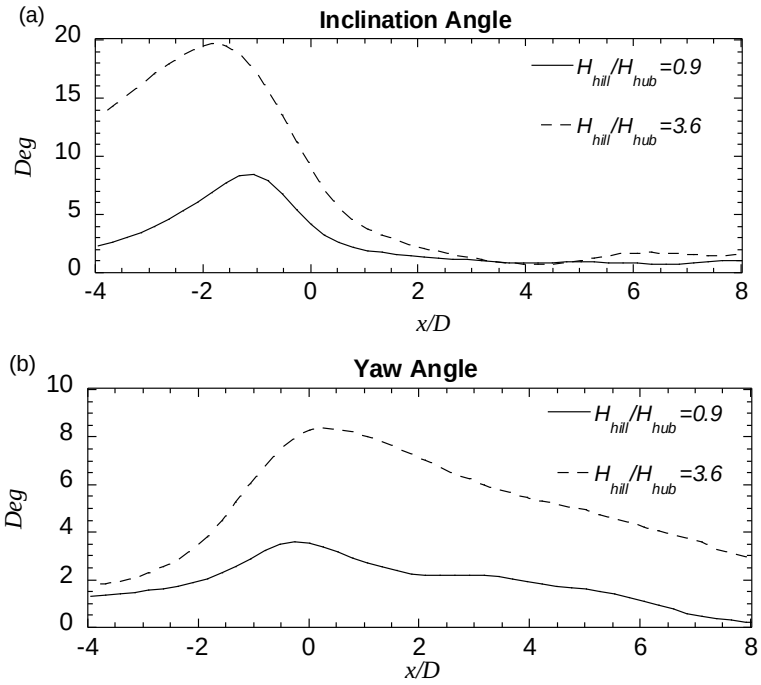

Figure 5-16 Terrain induced inflow angle at the hub height: (a)inclination angle in vertical direction; (b) yaw angle in horizontal direction

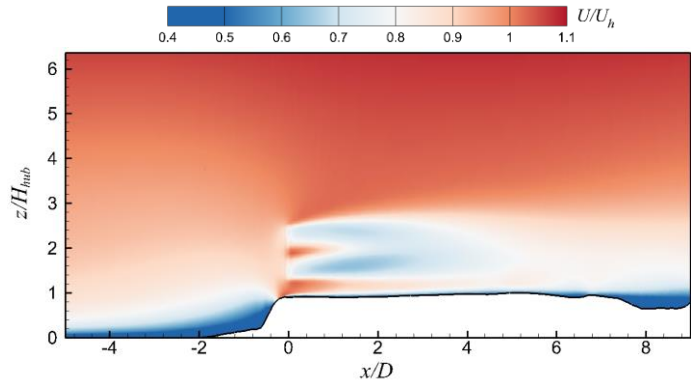

(a) vertical for H_{hill}/H_{hub}=0.9

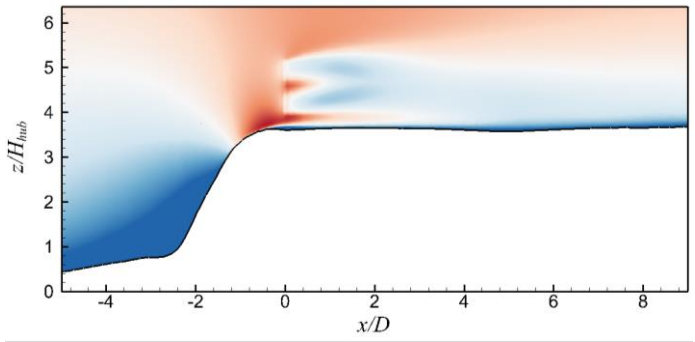

(b) vertical for H_{hill}/H_{hub}=3.6

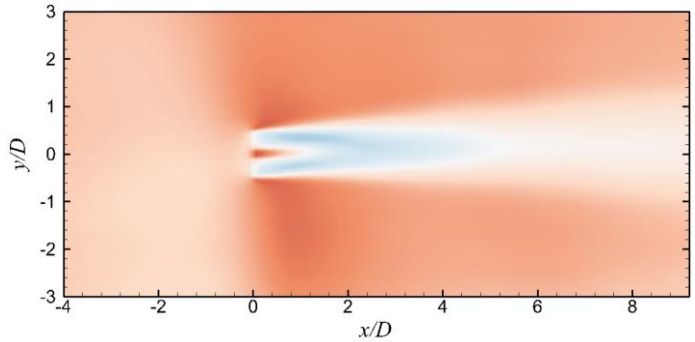

(c) horizontal for H_{hill}/H_{hub}=0.9

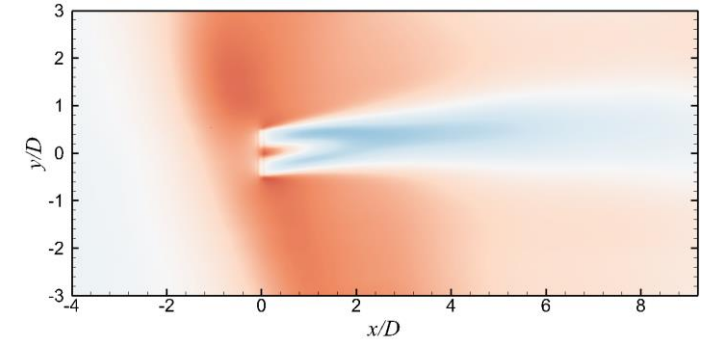

(d) horizontal for H_{hill}/H_{hub}=3.6

Figure 5-17 Wind turbine wake flow over the escarpment: (a), (c) for x-z plane through the turbine rotor center; (b), (d) for x-y plane at the hub height;

The wakes over the escarpment are simulated also based on the operational condition of constant rotational speed of 21 RPM. Figure 5-17 displays the simulated wake flow over the two escarpments with different height, where the contours of the mean velocity are normalized by the wind speed of the wind flow without wind turbine at hub height (designated as U_h). In the vertical direction, the wakes shift up in the near wake region but not distinctly in the far wake region, this is due to the fact that the terrain induced inclination angles are quite small downwind the turbine, as shown in Figure 5-16 (a). In the horizontal direction, an obvious wake deflection is observed for the high escarpment case. By contrast, there is no significant wake deflection for the low escarpment case since the yaw misalignment angle is much smaller than that over the high escarpment, which is consistent with the result presented in Figure 5-16 (b). It can be concluded that, when a steep escarpment is lower than the turbine hub height, the terrain effects can be negligible and the wake behavior can be treated same as the that over the flat terrain. However, a steep escarpment with the elevation several times of the hub height would influence the wake behavior significantly.

5.5 Application of Analytical Wake Model

5.5.1 Hybrid Framework of Setup the Proposed Model

In a real wind farm, terrain mainly induces the variation of wind speed, turbulence intensity, wind direction (inclination angle and yaw angle). In order to reduce the computational cost of wake modelling while remaining comparable accuracy in wake prediction, a hybrid numerical/analytical framework is developed to consider terrain effects in real wind farm, in which the ambient wind flow over the terrain is obtained by full CFD simulation while the wake effects due to the presence of turbine are calculated by the analytical model. The detailed procedures to set up the proposed model are illustrated in Figure 5-19. Firstly, a full CFD simulation without turbines is performed to provide the wind field information including the wind speed ratio, turbulence intensity, and local wind direction. Subsequently, these informations are extracted and interpolated as the initial conditions for the proposed analytical model. Finally, by the superposition of analytical

model calculated wake effects and CFD resolved initial wind field, the wake flow are predicted in the real wind farm. Here are three tips should be noted for implementing the analytical model in the above framework. Firstly, the proposed wake model (section 4.4) included the effects of yaw angle in horizontal direction, while the inclination angle effects can be analogously applied to this model in the vertical direction. Secondly, the velocity deficit calculation in the wake model is always for the velocity component which is perpendicular to the rotor disc, and other velocity components are remained. Finally, in the wake deflection model presented in Figure 4-13, the deflection value is regards to the axis along the incoming wind direction. It is originally designed for active yaw control condition, in which the wind direction normally is fixed. However, for yaw or inclination misalignment cases, as shown in Figure 5-18 the wind turbine is fixed, thus normally the wake deflection by the change of wind direction is calculated in a fixed coordinate system (x', y'). As a result, the deflection value should be transformed by the following Equation.

$$y_d' = \frac{y_d}{cos\gamma} + x' tan\gamma \tag{5-2}$$

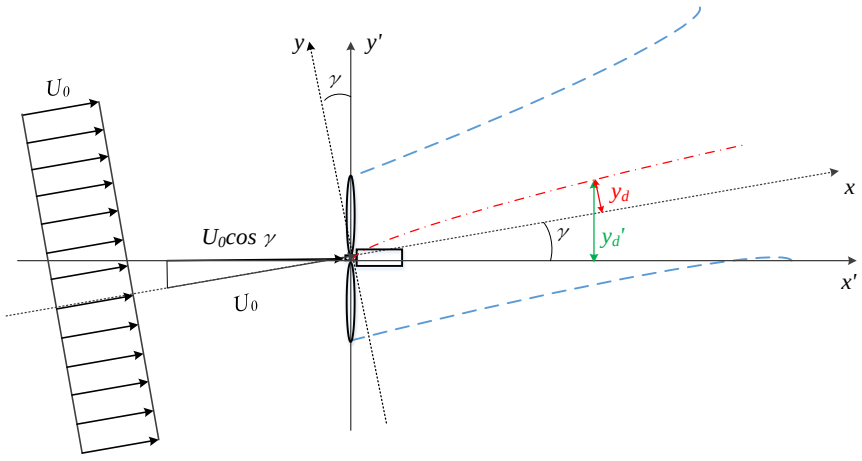

Figure 5-18 Schematic of wake deflection in the coordinate system with fixed wind turbine

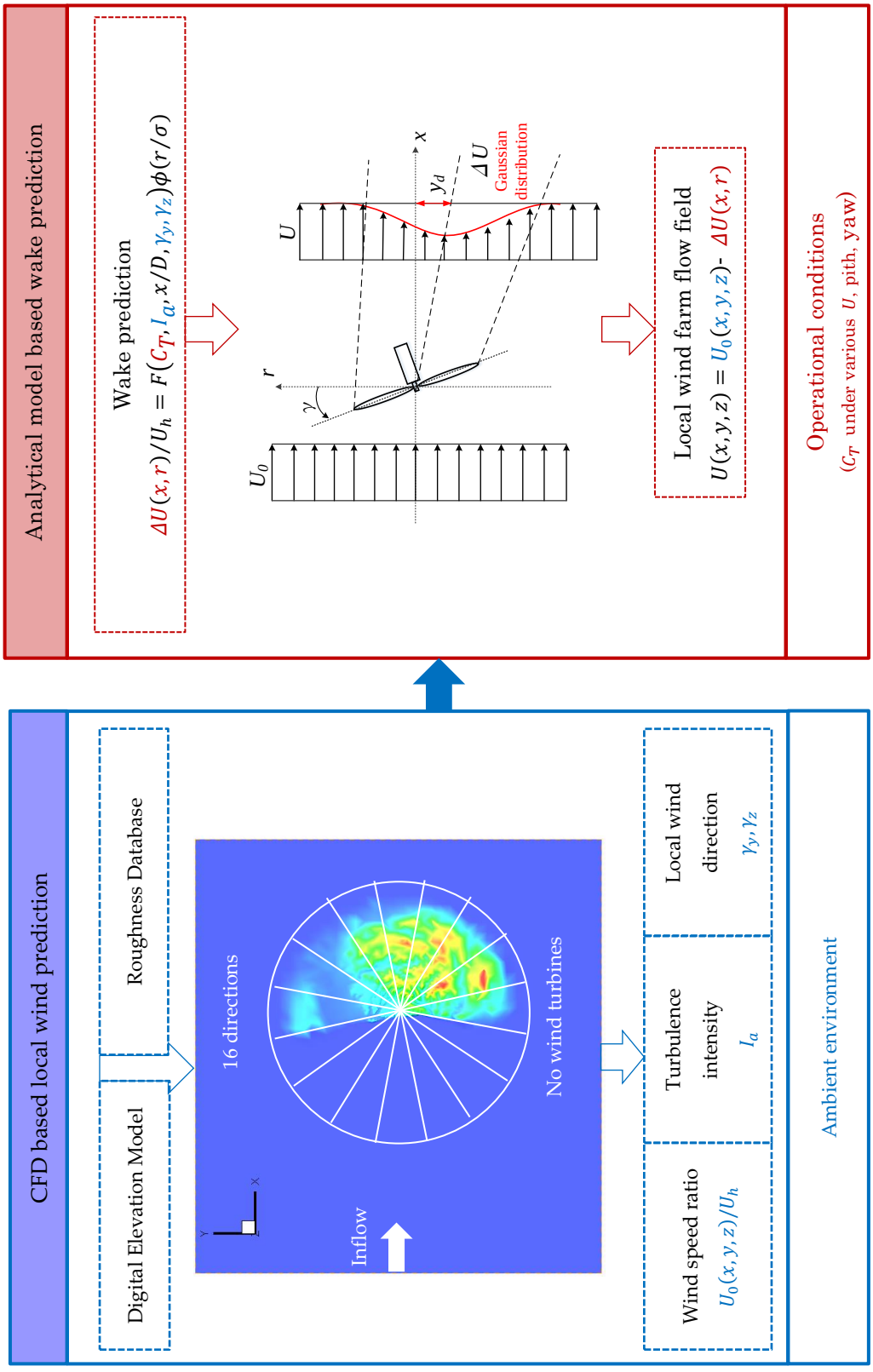

Figure 5-19 Schematic of procedure to apply analytical wake model in the real wind farm by incorporating the terrain effects

5.5.2 Verification

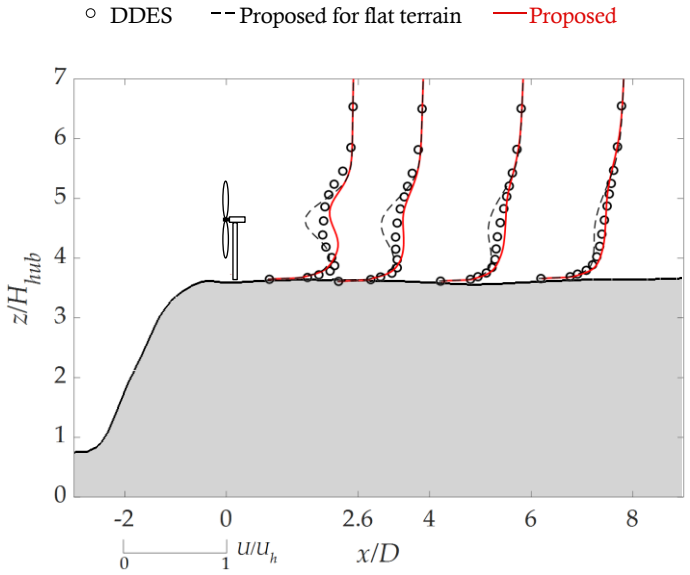

(a) vertical profiles of mean velocity over terrain

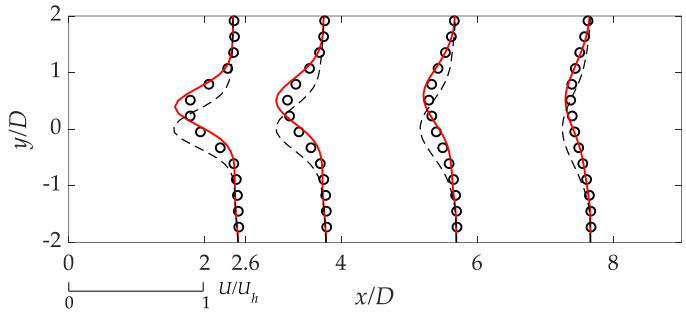

(b) horizontal profiles of mean velocity over terrain

Figure 5-20 Comparison of analytical models for normalized mean velocity: (a) for vertical profiles in the plane of y=0; (b) for horizontal profiles in the x-y plane at hub height

The vertical and horizontal profiles of the normalized mean velocity U/U_h and turbulence intensity at selected downwind locations of $x = 2.6D, 4D, 6D, 8D$ are plotted in Figure 5-20 and Figure 5-21, respectively, to illustrate the quantitative comparison between the numerical results and those predicted by the analytical models. Open circles denote the simulated results, red solid lines represent the values predicted by the proposed hybrid framework. The values predicted by the proposed analytical model without considering the yaw and inclination angle are also plotted by black solid lines for comparison. All the velocities are normalized by the hub height mean velocity U_h. The x-axis denotes the

distance from the wind turbine normalized by the rotor diameter D. The distance of $2D$ corresponds to a unit scale of normalized mean velocity U/U_h in Figure 5-20 and a scale of turbulence intensity with the value of 0.3 in Figure 5-21. It can be clearly found that the new proposed analytical model by considering the terrain effects gives more reasonable wake prediction both in horizontal and vertical directions. It can be inferred that an analytical wake model without considering the inclination and yaw angle effects cannot be directly applied for the turbine over the complex terrain.

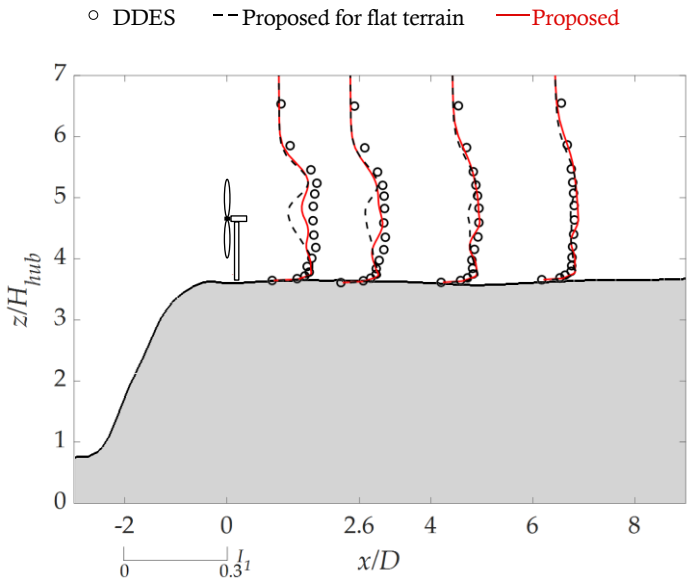

(a) vertical profiles of turbulence intensity over terrain

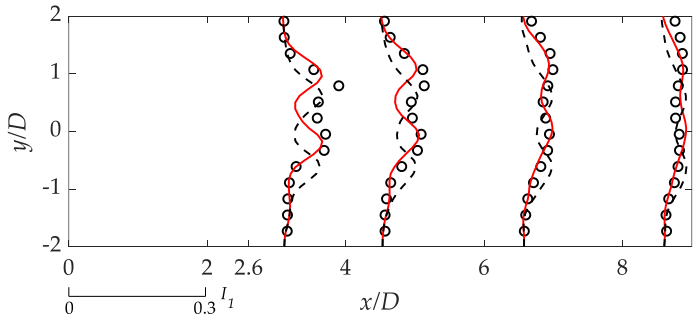

(b) horizontal profiles of turbulence intensity over terrain

Figure 5-21 Comparison of analytical models for turbulence intensity: (a) for vertical profiles in the plane of y=0; (b) for horizontal profiles in the x-y plane at hub height

5.6 Summary

In this chapter, a comprehensive field measurement focusing on the wind turbine wake over complex terrain was conducted. The terrain effects on the wind turbine wake flow are later investigated by the developed numerical model and a hybrid framework is proposed to apply the new proposed analytical model in real wind farm to consider the terrain effects. Following conclusions are obtained:

1. The numerical results of wind flow and wind turbine wake simulation over complex terrain show favourably good agreement with the measurements for each wind direction, which validated the developed numerical framework based on a modified DDES model.

2. For the wind flow over the escarpment with an irregular edge, the wind direction changes both in the vertical and horizontal direction with the inclination and yaw misalignment angle regard to the wind turbine. As a result, the wake over the escarpment deflected both in vertical and horizontal direction. When a steep escarpment is lower than the turbine hub height, the terrain effects can be negligible and the wake behavior can be treated same as the that over the flat terrain. However, a steep escarpment with the elevation several times of the hub height would influence the wake behavior significantly.

3. A hybrid numerical/analytical framework for wake prediction in real wind farm is developed, in which the ambient environment including the terrain and surface roughness are considered by a full CFD simulation while the wind turbine wake effects are presented by the new proposed analytical model. The new analytical wake model by considering the terrain effects is later verified by the numerical simulation and shows good performance for prediction of wind turbine wakes in the complex terrain.

Chapter6. CONCLUSIONS

This research focus on numerical study and analytical study of wind turbine wakes considering the ambient environment and turbine operational conditions. Wind turbine wakes characteristics under various condition are investigated at first by numerical simulation. Then a new analytical wake model is proposed based on the numerical study and analysis. Finally, application of the developed numerical framework and analytical model in real wind farm over the complex terrain are examined and validated. The main original contributions and conclusions corresponding to three objectives set in the beginning of this thesis are as follows.

1. A coupled BEM-CFD model is validated for wake prediction and the effects of ambient turbulence intensity, thrust coefficient and yaw angle are systematically investigated by using numerical simulation.

The LES simulation results of mean velocity and turbulence intensity in the wake flow show good agreement with the experimental data for the model wind turbine, which validated the BEM-CFD coupled model for wind turbine wake prediction. The mean velocity and turbulence intensity behind the model and utility-scale wind turbines show quite close profiles, which indicate that the thrust coefficient and ambient turbulence intensity are the dominant parameters for the wake flow in spite of the specific wind turbine type.

The effects of ambient turbulence intensity and wind turbine thrust coefficient on the mean velocity are summarized as follows. High ambient turbulence intensity leads to shorter wake region since the high turbulence accelerates the process of flow mixing in the wake

region. In addition, the large thrust coefficient induces stronger velocity deficit in the wake region. The horizontal profiles show axial symmetric and some asymmetry in near wake region is due to the effect of torque on the rotor.

The effects of ambient turbulence intensity and wind turbine thrust coefficient on the turbulence intensity in the wake are summarized as follows. An obvious enhancement of turbulence occurs in the upper half of the wake region, especially at the top tip height. This enhancement is related to the wind shear that is the sharp shape of mean velocity profile near the top tip. In the lower part of the wake flow, the added turbulence intensity is weakened. It is due to the strong turbulence mixing near the ground. Larger thrust coefficient cases exhibit larger turbulence intensity in the wake flow and the maximum turbulence intensity occurs in the near wake region. Meanwhile, it can be clearly observed that the nacelle and tower also generate considerable turbulence but it vanishes quickly in the near wake region. The turbulence intensities in the horizontal direction present a dual-peak and approximately axisymmetric distribution with the maximum value near the two side-tip positions.

Reynolds Stress Model shows good performance for wake prediction in atmospheric boundary layer, where both mean velocity and turbulence intensity show good agreement with those by LES model.

The effects of ambient turbulence intensity, thrust coefficient and yaw angle on the wake deflection are systematically investigated. The wake velocity deficit reduces when the yaw angle increases since larger yaw angle induces smaller thrust force on the rotor. In addition, the wake center trajectories show apparent wake deflections under yawed conditions. As expected, the wake deflection increases with the increase of yaw angle. It can also be seen that the large thrust coefficient induces stronger wake deflection than the cases with small thrust coefficient. The high ambient turbulence intensity leads to smaller wake deflection and shorter wake region than cases with the low ambient turbulence as the situation under the non-yawed condition. The high turbulence accelerates the process of flow mixing in the wake region, thus wake deflection recovers faster than those with the low ambient turbulence intensity.

2. A new analytical wake model is proposed and shows good performance for prediction of mean velocity and turbulence intensity under various ambient turbulence, thrust coefficient and yawed conditions.

A new Gaussian-based wake model is proposed to predict the mean velocity deficit and added turbulence intensity in the near and far wake region. The proposed model shows good performance for prediction of maximum values as well as distributions of mean velocity and turbulence intensity under various ambient turbulence and thrust coefficient conditions.

The applicability of the Frandsen's model used in IEC61400-1 and the proposed model for the local turbulence intensity prediction in the wake region are investigated. The proposed model provides more accurate predictions, while Frandsen's model shows conservative results in the near wake region.

A new analytical wake deflection model is proposed based on the Gaussian distribution for velocity deficit and the top-hat shape for skew angle and it is validated by comparison with the results obtained from the wind tunnel test and the numerical simulations. The model parameters are determined as the function of ambient turbulence intensity and thrust coefficient, which enables the model to have good applicability under various conditions.

The proposed Gaussian-based wake model is later updated for yaw wind turbines by incorporating the proposed wake deflection model to consider the yaw angle effects, which shows good performance for predicting distributions of mean velocity and turbulence intensity by comparison with the numerical results.

3. The developed numerical framework based on a modified DDES model is validated for wind flow and wind turbine wake flow prediction over complex terrain. The terrain effects on the wind turbine wake flow are systematically investigated and the applicability of the new proposed analytical model in complex terrain is verified.

The numerical results of wind flow and wind turbine wake simulation over complex terrain show favourably good agreement with the measurements for each wind direction, which validated the developed numerical framework based on a modified DDES model.

For the wind flow over the escarpment with an irregular edge, the wind direction changes both in the vertical and horizontal direction with the inclination and yaw misalignment angle regard to the wind turbine. As a result, the wake over the escarpment deflected both in vertical and horizontal direction. When a steep escarpment is lower than the turbine hub height, the terrain effects can be negligible and the wake behavior can be treated same as the that over the flat terrain. However, a steep escarpment with the elevation several times of the hub height would influence the wake behavior significantly.

A hybrid numerical/analytical framework for wake prediction in real wind farm is developed, in which the ambient environment including the terrain and surface roughness are considered by a full CFD simulation while the wind turbine wake effects are presented by the new proposed analytical model. The new analytical wake model by considering the terrain effects is later verified by the numerical simulation and shows good performance for prediction of wind turbine wakes in the complex terrain.

APPENDIX A. INDIVIDUAL WIND TURBINE CONTROL SYSTEM

Figure A-1 shows the schematic of a greedy control system of the modern three-bladed horizontal-axis wind turbine. The aerodynamic forces acting on blades generate a torque on the rotor T_r which is dependent on the effective wind speed U, the rotor speed ω and the pitch angle of the blades β. The internal controller of the pitch actuator tracks a desired pitch angle β_d. The power generating unit has an internal controller tracking a desired generator speed ω_d. To regulate the amount of power conversion and the rotor speed, these control inputs are used by a power and speed controller.

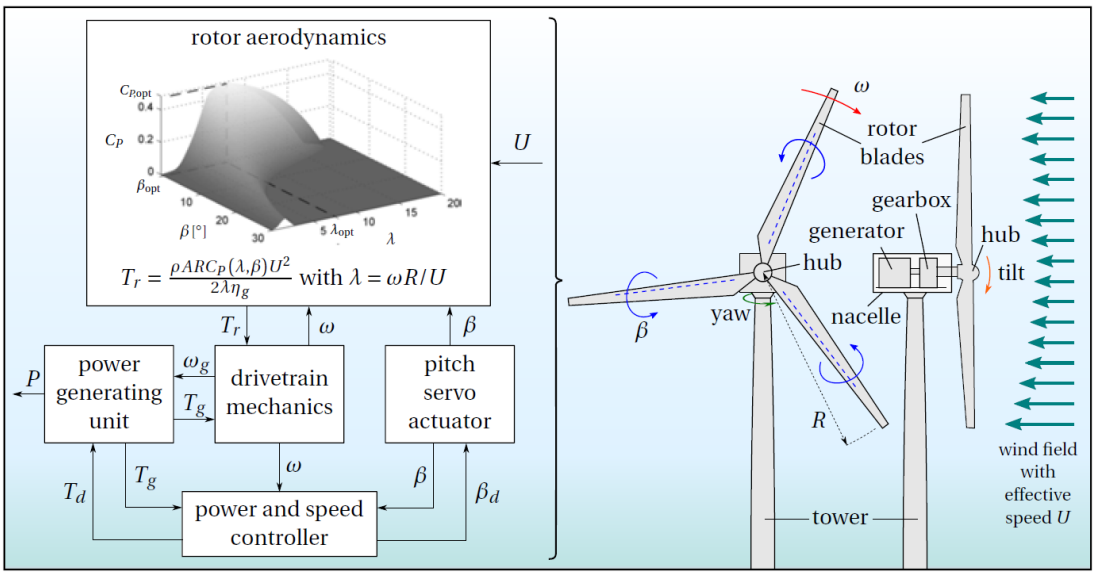

Figure A-1 Subsystems-level model scheme for the greedy control system of wind turbine (Gebraad et al., 2014)

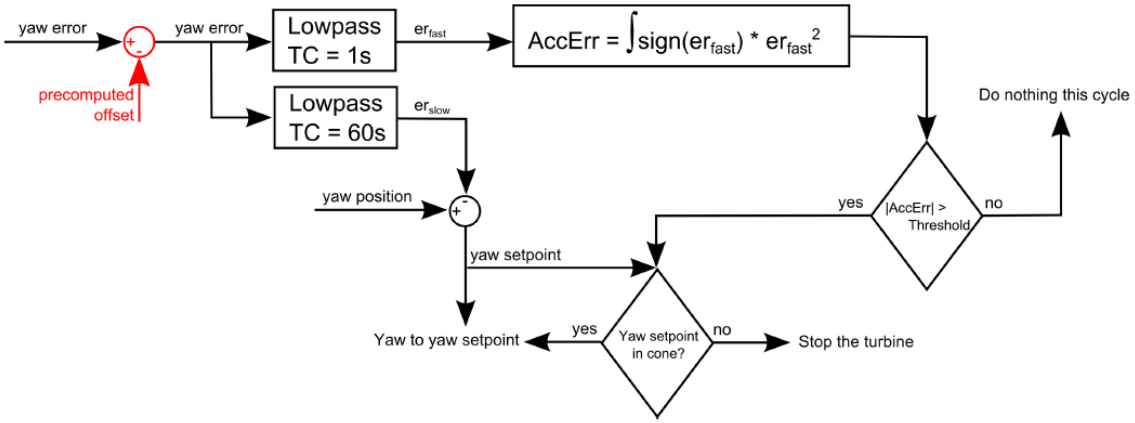

Figure A-2 Conventional greedy yaw control and correction system (Fleming et al., 2014)

In addition to the wind speed, the wind turbine should also normally response to the wind direction to regulate the wind turbine aligned with the incoming wind speed by a yaw control system. Figure A-2 shows the schematic of the conventional greedy yaw control system. When the accumulated yaw error exceeds a certain threshold, the turbine will then yaw to a new setpoint, which is determined by a slow filtering of the yaw error, unless the setpoint is in an unallowed location.

APPENDIX B. GAUSSIAN DISTRIBUTION FUNCTION OF VELOCITY DEFICIT

An axisymmetric wake allows a two-dimensional formulation in cylindrical coordinates. Here the distance from the center of rotor along axial and radial directions are denoted by x and r respectively, and the velocity in the wake region is described by:

$$U = U_0 - \Delta U \tag{B - 1}$$

where U_0 is the wind speed of the incoming flow and ΔU denotes the velocity deficit.

When the wake flow is simplified without external forces and pressure gradients, the Equation of momentum for steady axisymmetric wake flow can be expressed in cylindrical coordinates as follows:

$$U\frac{\partial U}{\partial x} + W\frac{\partial U}{\partial r} = \nu_t\left(\frac{\partial^2 U}{\partial x^2} + \frac{1}{r}\frac{\partial U}{\partial r} + \frac{\partial^2 U}{\partial r^2}\right) \tag{B - 2}$$

where ν_t is the turbulence viscosity and is assumed to be constant. Since ΔU is small compared with U_0, $W\frac{\partial U}{\partial r}$ and $\frac{\partial^2 \Delta U}{\partial x^2}$ is subsEquationuently negligible. Equation. (B-2) can be simplified as Equation. (B-3) by inserting Equation. (B-1):

$$U_0\frac{\partial \Delta U}{\partial x} = \frac{\nu_t}{r}\frac{\partial}{\partial r}\left(r\frac{\partial \Delta U}{\partial r}\right) \tag{B - 3}$$

The following Equation can be obtained by applying the momentum conservation for the wake flow.

$$2\pi\rho U_0 \int (U_0 - U)\, r dr = \frac{1}{2}\rho U_0^2 C_T \pi \frac{D^2}{4} \tag{A - 4}$$

where C_T is the thrust coefficient of the turbine rotor and D is the diameter of rotor. Here, ΔU is neglected since it is smaller than U_0.

In view of the similarity of the velocity profiles and the assumption of power law for the velocity deficit and wake width, the following expressions can be obtained as shown by Schlichting (Schlichting, 1979):

$$\frac{\Delta U}{U_0} = C x^p f(\eta),\ \eta = \frac{r}{b} \tag{B - 5}$$

$$b = 2\left(\frac{\nu_t}{U_0}\right)^{1+m} x^{-m} \tag{B - 6}$$

where C is a constant and η is the distance from the wake center r normalized by the representative wake width b which Equationuals to $b_{1/2}/0.833$, C and ν_t are the function of the thrust coefficient as shown in the reference.

Substitution of Equation. (B-5) and (B-6) into Equation. (B-3) yields

$$C U_0^2 (pf + m\eta f')x^{p-1} = \frac{1}{4} C U_0 \nu_t \left(\frac{U_0}{\nu_t}\right)^{2+2m} \left(\frac{1}{\eta} f' + f''\right) x^{p+2m} \tag{B - 7}$$

in which the exponent of x at each side of the above Equation should be Equationual, which leads to $m = -1/2$. Then by submitting it back to Equation. (B-7), the differential Equation of η can be obtained as follows:

$$(\eta f')' + 2\eta^2 f' - 4p\eta f = 0 \tag{B - 8}$$

The boundary condition of the above Equation are

$$\left.\begin{array}{ll} f' = 0,\ f = 1 & (\eta = 0) \\ f = 0 & (\eta = \infty) \end{array}\right\} \tag{B - 9}$$

If p is set to -1, the solution of the above differential Equation is

$$f(\eta) = exp(-\eta^2) \tag{B -10}$$

Equation. (B-10) is an approximate solution of Equation. (B-8) and is used in this study.

APPENDIX C. STREAMWISE FUNCTION IN BASTANHAH AND PORTÉ-AGEL'S WAKE MODEL

If the viscous and pressure terms in the momentum Equation are neglected, the following Equation can be obtained for the wake by applying mass and momentum conservation:

$$2\pi\rho \int U(U_0 - U)\, r dr = \frac{1}{2}\rho U_0^2 C_T \pi \frac{D^2}{4} \qquad \text{(C - 1)}$$

where U_0 is the wind speed of incoming flow, U is the wind speed in the wake region and C_T is the thrust coefficient of the turbine rotor. Equation. (C-1) is the same as Equation. (B-4) if ΔU^2 is neglected. The self-similarity in the wake describes the normalized velocity deficit as:

$$\frac{\Delta U}{U_0} = C(x) f(r/\delta) \qquad \text{(C - 2)}$$

where $C(x)$, namely the streamwise function, represents the maximum normalized velocity deficit at each downwind location which occurs at the center of the wake, r is the radial distance from the wake center and δ is the characteristic wake width at each x. By taking the assumption of Gaussian distribution for the velocity deficit, Equation. (C-2) can be written as:

$$\frac{\Delta U}{U_0} = C(x) exp\left(-\frac{r^2}{2\sigma^2}\right) \qquad \text{(C - 3)}$$

Therefore, the wake velocity is given by:

$$U = U_0\left(1 - C(x)exp\left(-\frac{r^2}{2\sigma^2}\right)\right) \tag{C - 4}$$

Substituting for U from Equation. (C-4) into Equation. (C-1) and integrating from 0 to ∞ yields:

$$8\left(\frac{\sigma}{D}\right)^2 C(x)^2 - 16\left(\frac{\sigma}{D}\right)^2 C(x) + C_T = 0 \tag{C - 5}$$

By assuming σ/D as a constant, the above Equation can be solved as follows:

$$C(x) = 1 - \sqrt{1 - \frac{C_T}{8(\sigma/D)^2}} \tag{C - 6}$$

In fact, σ/D slightly increases in the wake region and is written as:

$$\sigma/D = k^* x/D + \varepsilon^* \tag{C - 7}$$

Substituting it into Equation. (C-6),

$$C(x) = 1 - \sqrt{1 - \frac{C_T}{8(k^* x/D + \varepsilon^*)^2}} \tag{C - 8}$$

where k^* denotes the wake expansion rate and ε^* are expressed as follows,

$$\varepsilon^* = 0.2\sqrt{\beta} \quad \text{with} \quad \beta = \frac{1}{2}\frac{1 + \sqrt{1 - C_T}}{\sqrt{1 - C_T}} \tag{C - 9}$$

A specific expression for k^* was not proposed by Bastankhah and Porté-Agel (Bastankhah and Porté-Agel, 2014), which consequently limits its applicability to other cases. In addition, it should be noted that $1 - C_T/[8(k^* x/D + \varepsilon^*)^2]$ in the Equation. (C-8) can be negative in the near wake region because Equation. (C-8) is an approximate solution of Equation. (C-5).

APPENDIX D. WAKE DEFECTION MODEL OF JIMÉNEZ ET AL.

Based on the momentum conservation and top-hat assumption for velocity deficit, the wake skew angle is proposed by Jimenez et al. (2009) as follows:

$$\theta = \frac{C_T cos^2\gamma sin\gamma}{2(1 + 2k_w\, x/D)} \tag{D - 1}$$

which is assumed to be constant in the spanwise direction within the wake boundary. k_w is the wake expansion factor and the recommend values is $k_w = 0.4I_a$ for the flat terrain under neutral conditions (Peña et al., 2016).

As shown by Gebraad et al. (2014) and Howland et al. (2016), the wake deflection was determined by integrating the skew angle θ in x and using $y_{d(x=0)} = 0$:

$$\frac{y_d}{D} = cos^2\gamma sin\gamma \frac{C_T}{4k_w}\left(1 - \frac{1}{1 + 2k_w\, x/D}\right) \tag{D - 2}$$

The top-hat velocity deficit model can be combined with this deflection model to predict the velocity field in yawed conditions. However, this model overestimates the wake deflection since the assumption of top-hat for the wake deficit is not accurate as pointed out by Ishihara et al. (2004).

APPENDIX E. WAKE DEFLECTION MODEL BY BASTANKHAH AND PORTÉ-AGEL

In the near-wake region, the initial skew angle at the rotor is derived based on the approach of Coleman et al. (1945) and is given by:

$$\theta_0 = \frac{0.3\gamma}{\cos\gamma}\left(1 - \sqrt{1 - C_T cos\gamma}\right) \quad \text{(E - 1)}$$

The length of the hypothetical potential core is expressed by

$$\frac{x_0}{D} = \frac{cos\gamma\left(1 + \sqrt{1 - C_T cos\gamma}\right)}{\sqrt{2}\left(\alpha I_a + \beta\left(1 - \sqrt{1 - C_T cos\gamma}\right)\right)} \quad \text{(E - 2)}$$

where $\alpha = 2.32,\ \beta = 0.154$.

The wake width at x_0 has the following expression,

$$\frac{\sigma_{y0}}{D} = \sqrt{\frac{1}{8}} cos\gamma, \quad \frac{\sigma_{z0}}{D} \approx \sqrt{\frac{1}{8}} \quad \text{(E - 3)}$$

As the wake skew angle is assumed to be constant in the potential core region, the value of deflection at x_0 is written as:

$$\frac{y_{d0}}{D} = \theta_0 \frac{x_0}{D} \quad \text{(E - 4)}$$

In the far-wake region, the wake deflection was determined as follows:

$$\frac{y_d}{D} = \theta_0 \frac{x_0}{D} + \frac{\theta_0}{14.7}\sqrt{\frac{cos\gamma}{k_y k_z C_T}}\left(2.9 + 1.3\sqrt{1 - C_T} - C_T\right) \times ln\left(\frac{\left(1.6 + \sqrt{C_T}\right)\left(1.6\sqrt{\frac{8\sigma_y\sigma_z}{D^2 cos\gamma}} - \sqrt{C_T}\right)}{\left(1.6 - \sqrt{C_T}\right)\left(1.6\sqrt{\frac{8\sigma_y\sigma_z}{D^2 cos\gamma}} + \sqrt{C_T}\right)}\right) \quad \text{(E - 5)}$$

where σ_y and σ_z are the wake width in horizontal and vertical direction and expressed as:

$$\frac{\sigma_y}{D} = k_y \frac{x - x_0}{D} + \frac{\sigma_{y0}}{D} \quad \text{(E - 6)}$$

$$\frac{\sigma_z}{D} = k_z \frac{x - x_0}{D} + \frac{\sigma_{z0}}{D} \quad \text{(E - 7)}$$

It should be noted that the parameters k_y and k_z have no specific formulas, which implies that the model by Bastankhah and Porté-Agel (2016) could not be generally applied in wake prediction under various conditions.

REFERENCE

Adaramola M.S., Krogstad P.-Å., 2011. Experimental investigation of wake effects on wind turbine performance. Renew. Energy 36, 2078–2086. doi:10.1016/J.RENENE.2011.01.024

Ainslie, J.F., 1988. Calculating the flowfield in the wake of wind turbines. J. Wind Eng. Ind. Aerodyn. 27, 213–224. doi:10.1016/0167-6105(88)90037-2

Ansys Inc., 2011. ANSYS Fluent Theory Guide. Canonsburg, PA.

Barthelmie, R.J., Cabezón, D., Hansen, K.S., Chaviaropoulos, R.K., 2012. Modeling wake effects in large wind farms in complex terrain :the problem,the methods and the issues. Wind Energy 161–182.

Barthelmie, R.J., Hansen, K., Frandsen, S.T., Rathmann, O., Schepers, J.G., Schlez, W., Phillips, J., Rados, K., Zervos, A., Politis, E.S., Chaviaropoulos, P.K., 2009. Modelling and measuring flow and wind turbine wakes in large wind farms offshore. Wind Energy 12, 431–444. doi:10.1002/we.348

Bastankhah, M., Porté-Agel, F., 2016. Experimental and theoretical study of wind turbine wakes in yawed conditions. J. Fluid Mech. 806, 506–541. doi:10.1017/jfm.2016.595

Bastankhah, M., Porté-Agel, F., 2014. A new analytical model for wind-turbine wakes. Renew. Energy 70, 116–123. doi:10.1016/j.renene.2014.01.002

Bechmann, A., Sørensen, N.N., 2010a. Hybrid RANS/LES method for wind flow over complex terrain. Wind Energy 13, 36–50. doi:10.1002/we.346

Bechmann, A., Sørensen, N.N., 2010b. Hybrid RANS/LES method for wind flow over complex terrain. Wind Energy 13, 36–50. doi:10.1002/we.346

Berg, J., Troldborg, N., Sorensen, N.N., Patton, E.G., Sullivan, P.P., 2017. Large-Eddy Simulation of turbine wake in complex terrain. J. Phys. Conf. Ser. 854. doi:10.1088/1742-6596/854/1/012003

Blocken, B., Stathopoulos, T., Carmeliet, J., 2007. CFD simulation of the atmospheric boundary layer: wall function problems. Atmos. Environ. 41, 238–252. doi:10.1016/J.ATMOSENV.2006.08.019

Bossanyi, E.A., 2003. GH Bladed Version 3.51 User Manual, Garrad Hassan and Partners Limited. doi:10.1017/CBO9781107415324.004

Boussinesq, J., 1877. Essai sur la théorie des eaux courantes.

Burton, T., Sharpe, D., Jenkins, N., Bossanyi, E., 2011. Wind Energy Handbook, 2nd ed. Wiley.

Cabezón, D., Migoya, E., Crespo, A., 2011. Comparison of turbulence models for the computational fluid dynamics simulation of wind turbine wakes in the atmospheric boundary layer. Wind Energy 14, 909–921. doi:10.1002/we.516

Calaf, M., Meneveau, C., Meyers, J., 2010. Large eddy simulation study of fully developed wind-turbine array boundary layers. Phys. Fluids 22, 015110. doi:10.1063/1.3291077

Chamorro, L.P., Porte-Agel, F., 2009. A wind-tunnel investigation of wind-turbine wakes: Boundary-Layer turbulence effects. Boundary-Layer Meteorol. 132, 129–149. doi:10.1007/s10546-009-9380-8

Chatelain, P., Backaert, S., Winckelmans, G., Bricteux, L., Backaert, S., Winckelmans, G., Kern, S., Koumoutsakos, P., 2014. Vortex particle-mesh methods with immersed lifting lines applied to the Large Eddy Simulation of wind turbine wakes.

Coleman, R.P., Feingold, A.M., 1945. Evaluation of the Induced-Velocity Field of an Idealized Helicoptor Rotor. Wartime Rep. 28.

Crespo, A., Hernández, J., 1996. Turbulence characteristics in wind-turbine wakes. J. Wind Eng. Ind. Aerodyn. 61, 71–85. doi:10.1016/0167-6105(95)00033-X

Crespo, A., Hernández, J., Frandsen, S., 1999. Survey of modelling methods for wind turbine wakes and wind farms. Wind Energy 2, 1–24. doi:10.1002/(SICI)1099-1824(199901/03)2:1<1::AID-WE16>3.0.CO;2-7

Crespo, A., Manuel, F., Grau, J.C., Hernández., J., 1993. Modelization of wind farms in complex terrain. Application to the Monteahumada wind farm, in: European Community Wind Energy Conference. Travemünde, pp. 440–443.

Daaou Nedjari, H., Guerri, O., Saighi, M., 2017. CFD wind turbines wake assessment in complex topography. Energy Convers. Manag. 138, 224–236. doi:10.1016/j.enconman.2017.01.070

Dörenkämper, M., Witha, B., Steinfeld, G., Heinemann, D., Kühn, M., 2015. The impact of stable atmospheric boundary layers on wind-turbine wakes within offshore wind farms. J. Wind Eng. Ind. Aerodyn. 144, 146–153. doi:10.1016/J.JWEIA.2014.12.011

Enoki, K., Ishihara, T., 2012. A generalized canopy model and its application to the prediction of urban wind climate. J. Japan Soc. Civ. Eng. 68, 28–47.

Feng, J., Shen, W.Z., 2014. Wind farm layout optimization in complex terrain: A preliminary study on a Gaussian hill. J. Phys. Conf. Ser. 524, 012146. doi:10.1088/1742-6596/524/1/012146

Ferziger, J.H., Perić, M. (Milovan), 2002. Computational methods for fluid dynamics. Springer.

Fleming, P.A., Gebraad, P.M.O., Lee, S., van Wingerden, J.W., Johnson, K., Churchfield, M., Michalakes, J., Spalart, P., Moriarty, P., 2014. Evaluating techniques for redirecting turbine wakes using SOWFA. Renew. Energy 70, 211–218. doi:10.1016/j.renene.2014.02.015

Fleming, P.A., Scholbrock, A.K., Jehu, A., Davoust, S., Osler, E., Wright, A.D., Clifton, A., 2014. Field-test results using a nacelle-mounted lidar for improving wind turbine power capture by reducing yaw misalignment. J. Phys. Conf. Ser. 524, 012002. doi:10.1088/1742-6596/524/1/012002

Frandsen, S., Barthelmie, R., Pryor, S., Rathmann, O., Larsen, S., Hojstrup, J., 2006. Analytical modelling of wind speed deficit in large offshore wind farms. Wind Energy 9, 39–53. doi:10.1002/we

Frandsen, S.T., 2007. Turbulence and turbulence-generated structural loading in wind turbine clusters. Technical University of DenmarkDanmarks Tekniske Universitet, Risø National Laboratory for Sustainable EnergyRisø Nationallaboratoriet for Bæredygtig Energi.

Fröhlich, J., von Terzi, D., 2008. Hybrid LES/RANS methods for the simulation of turbulent flows. Prog. Aerosp. Sci. 44, 349–377. doi:10.1016/J.PAEROSCI.2008.05.001

Fu, S., Launder, B.E., Leschziner, M.A., 1987. Modelling strongly swirling recirculating jet flow with Reynolds-stress transport closures. Symp. Turbul. Shear Flows, 6th, Toulouse, Fr. Sept. 7-9, 1987, Proc. (A88-38951 15-34). Univ. Park. PA, Pennsylvania State Univ. 1987, p. 17-6-1 to 17-6-6. Res. Support. by Roll. PLC. 17–6.

Gao, X., Yang, H., Lu, L., 2016. Optimization of wind turbine layout position in a wind farm using a newly-developed two-dimensional wake model. Appl. Energy 174, 192–200. doi:10.1016/j.apenergy.2016.04.098

Gebraad, P.M.O., Teeuwisse, F.W., van Wingerden, J.W., Fleming, P.A., Ruben, S.D., Marden, J.R., Pao, L.Y., 2014. Wind plant power optimization through yaw control using a parametric model for wake effects-a CFD simulation study. Wind Energy 19, 95–114. doi:10.1002/we.1822

Gibson, M.M., Launder, B.E., 1978. Ground effects on pressure fluctuations in the atmospheric boundary layer. J. Fluid Mech. 86, 491. doi:10.1017/S0022112078001251

Glauert, H., 1926. The analysis of experimental results in the windmill brake and vortex ring states of an airscrew. HMSO, London.

Göçmen, T., Giebel, G., 2016. Estimation of turbulence intensity using rotor effective wind speed in Lillgrund and Horns Rev-I offshore wind farms. Renew. Energy 99, 524–532. doi:10.1016/j.renene.2016.07.038

Goit, J.P., Meyers, J., 2015. Optimal control of energy extraction in wind-farm boundary layers. J. Fluid Mech. 768, 5–50. doi:10.1017/jfm.2015.70

Grimmond, C.S.B., Oke, T.R., Grimmond, C.S.B., Oke, T.R., 1999. Aerodynamic Properties of Urban Areas Derived from Analysis of Surface Form. J. Appl. Meteorol. 38, 1262–1292. doi:10.1175/1520-0450(1999)038<1262:APOUAD>2.0.CO;2

Gritskevich, M.S., Garbaruk, A. V., Schütze, J., Menter, F.R., 2012. Development of DDES and IDDES Formulations for the k-ω Shear Stress Transport Model. Flow, Turbul. Combust. 88, 431–449. doi:10.1007/s10494-011-9378-4

GWEC, 2018. Growth of the wind power industry around the world [WWW Document]. URL http://gwec.net/global-figures/graphs/

Haans, W., 2011. Wind turbine aerodynamics in yaw: unravelling the measured rotor wake. Delft University of Technology.

Han, X., Guo, J., Wang, P., 2012. Adequacy study of a wind farm considering terrain and wake effect. IET Gener. Transm. & Distrib. 6, 1001–1008.

Hasager, C.B., Rasmussen, L., Peña, A., Jensen, L.E., Réthoré, P.E., 2013. Wind farm wake: The Horns Rev photo case. Energies 6, 696–716. doi:10.3390/en6020696

Hassan, U., Glendinning, A.G., Morgan, C.A., 1990. A wind tunnel investigation of the

wake structure and machine loads within small wind turbine farms, in: Davies, T., Halliday, J., Palutikov, J. (Eds.), Proceedings of the 12th BWEA Wind Energy Conference. pp. 47–52.

Howland, M.F., Bossuyt, J., Martinez-Tossas, L.A., Meyers, J., Meneveau, C., 2016. Wake Structure of Wind Turbines in Yaw under Uniform Inflow Conditions.

Howland, M.F., Bossuyt, J., Martínez-Tossas, L.A., Meyers, J., Meneveau, C., Mart Inez-Tossas, L.A., 2016. Wake structure in actuator disk models of wind turbines in yaw under uniform inflow conditions. J. Renew. Sustain. Energy 8. doi:10.1063/1.4913695

IEC 61400-1:2005+AMD1:2010, Wind turbines - Part 1: Design requirements, 2014.

Iizuka, S., Kondo, H., 2006. Large-eddy simulations of turbulent flow over complex terrain using modified static eddy viscosity models. Atmos. Environ. 40, 925–935. doi:10.1016/J.ATMOSENV.2005.10.014

Iizuka, S., Kondo, H., 2004. Performance of various sub-grid scale models in large-eddy simulations of turbulent flow over complex terrain. Atmos. Environ. 38, 7083–7091. doi:10.1016/J.ATMOSENV.2003.12.050

Ishihara, T., Hibi, K., 2002. Numerical study of turbulent wake flow behind a three-dimensional steep hill. Wind Struct. 5, 317–328. doi:10.12989/was.2002.5.2_3_4.317

Ishihara, T., Qi, Y., 2018. Numerical study of turbulent flow fields over steep terrains by using a modified delayed detached eddy simulations. Boundary-Layer Meteorol. (Accepted).

Ishihara, T., Qi, Y.H., 2018. Numerical study of turbulent flow fields over steep terrains by using the delayed detached eddy simulations. Boundary-Layer Meteorol (under review).

Ishihara, T., Yamaguchi, A., Fujino, Y., 2004. Development of a new wake model based on a wind tunnel experiment. Glob. Wind Power.

Jensen, N.O., 1983. A note on wind generator interaction, Risø-M-2411 Risø National Laboratory Roskilde. doi:Riso-M-2411

Jiménez, Á., Crespo, A., Migoya, E., 2009. Application of a LES technique to characterize the wake deflection of a wind turbine in yaw. Wind Energy 13, 559–572. doi:10.1002/we.380

Jiménez, Á., Crespo, A., Migoya, E., Garcia, J., 2007. Advances in large-eddy simulation of a wind turbine wake. J. Phys. Conf. Ser. 75, 012041. doi:10.1088/1742-6596/75/1/012041

Johansson, P.B. V, George, W.K., Gourlay, M.J., 2003. Equilibrium similarity, effects of initial conditions and local Reynolds number on the axisymmetric wake. Phys. Fluids 15, 603–617. doi:10.1063/1.1536976

JWPA, 2017. Offshore Wind Power Development in Japan [WWW Document]. URL http://jwpa.jp/pdf/20170228_OffshoreWindPower_inJapan_r1.pdf

Katic, I., Hojstrup, J., Jensen, N.O., 1986. A simple model for cluster efficiency i.katic. j.højstrup. n.o.jensen. Eur. Wind energy Assoc. Conf. Exhib. 1986 407–410.

Komatsubara, K., 2012. WIND ENERGY JAPAN. Tokyo.

Kuo, J., Rehman, D., Romero, D.A., Amon, C.H., 2018. A novel wake model for wind farm design on complex terrains. J. Wind Eng. Ind. Aerodyn. 174, 94–102. doi:10.1016/j.jweia.2017.12.016

Launder, B.E., 1989. Second-moment closure and its use in modelling turbulent industrial flows. Int. J. Numer. Methods Fluids 9, 963–985. doi:10.1002/fld.1650090806

Launder, B.E., 1989. Second-moment closure: present… and future? Int. J. Heat Fluid Flow 10, 282–300. doi:10.1016/0142-727X(89)90017-9

Lien, F.., Leschziner, M.., 1994. Assessment of turbulence-transport models including non-linear rng eddy-viscosity formulation and second-moment closure for flow over a backward-facing step. Comput. Fluids 23, 983–1004. doi:10.1016/0045-7930(94)90001-9

Liu, Z., Ishihara, T., Tanaka, T., He, X., 2016. LES study of turbulent flow fields over a smooth 3-D hill and a smooth 2-D ridge. J. Wind Eng. Ind. Aerodyn. 153, 1–12. doi:10.1016/j.jweia.2016.03.001

Luo, L., Srivastava, N., Ramaprabhu, P., 2014. A Study of Intensified Wake Deflection by Multiple Yawed Turbines based on Large Eddy Simulations 1–19. doi:10.2514/6.2015-0220

Makridis, A., Chick, J., 2013. Validation of a CFD model of wind turbine wakes with terrain effects. J. Wind Eng. Ind. Aerodyn. 123, 12–29. doi:10.1016/J.JWEIA.2013.08.009

Manwell, J.F., McGowan, J.G., Rogers, A.L., 2010. Wind energy explained : theory, design and application. Wiley.

Medici, D., & Dahlberg, J.Å., 2003. Potential improvement of wind turbine array efficiency by active wake control (AWC), in: EWEA. Dept. of mechanics, the Royal Institute of Technology, pp. 65–84.

Medici, D., Alfredsson, P.H., 2006. Measurements on a wind turbine wake: 3D effects and bluff body vortex shedding. Wind Energy 9, 219–236. doi:10.1002/we.156

Migoya, E., Crespo, A., García, J., Moreno, F., Manuel, F., Jiménez, Á., Costa, A., 2007. Comparative study of the behavior of wind-turbines in a wind farm. Energy 32, 1871–1885. doi:10.1016/J.ENERGY.2007.03.012

Mikkelsen, T., Angelou, N., Hansen, K., Sjöholm, M., Harris, M., Slinger, C., Hadley, P., Scullion, R., Ellis, G., Vives, G., 2013. A spinner-integrated wind lidar for enhanced wind turbine control. Wind Energy 16, 625–643. doi:10.1002/we.1564

MLIT, n.d. Land-use Database [WWW Document]. URL http://www.mlit.go.jp.

Murali, A., Rajagopalan, R.G., 2017. Numerical simulation of multiple interacting wind turbines on a complex terrain. doi:10.1016/j.jweia.2017.01.005

Neustadter, H.E., Spera, D.A., 1985. Method for Evaluating Wind Turbine Wake Effects on Wind Farm Performance. J. Sol. Energy Eng. 107, 240. doi:10.1115/1.3267685

Niayifar, A., Porté-agel, F., 2016. Analytical Modeling of Wind Farms : A New Approach for Power Prediction. Energies 9, 741. doi:10.3390/en9090741

Oka, S., Ishihara, T., 2009. Numerical study of aerodynamic characteristics of a square prism in a uniform flow. J. Wind Eng. Ind. Aerodyn. 97, 548–559. doi:10.1016/j.jweia.2009.08.006

Parkin, P., Holm, R., Medici, D., 2001. The application of PIV to the wake of a wind turbine in yaw, in: Particle Image Velocimetry. Dept. of mechanics, the Royal Institute of Technology, Gottingen.

Peña, A., Réthoré, P.-E., van der Laan, M.P., 2016. On the application of the Jensen wake

model using a turbulence-dependent wake decay coefficient: the Sexbierum case. Wind Energy 19, 763–776. doi:10.1002/we.1863

Quarton, D., 1989. Wake turbulence characterization, Final Report from Gaarad Hassan and Partners to the Energy Technology Support Unit of the Department of Energy of the UK.

S. Lissaman, P.B., 1979. Energy Effectiveness of Arbitrary Arrays of Wind Turbines. J. Energy 3, 323–328. doi:10.2514/3.62441

Sanderse, B., 2009. Aerodynamics of wind turbine wakes: Literature review. Energy Res. Cent. Netherlands 1–46. doi:10.1002/we

Sanderse, B., DerPijl, S.P. va., Koren, B., 2011. Review of computational fluid dynamics for wind turbine wake aerodynamics. Wind Energy 14, 799–819. doi:10.1002/we

Schatzmann, M., Olesen, H., Franke, J., 2010. COST 732 model evaluation case studies: approach and results.

Schlichting, H., 1979. Boundary-layer theory, 7th ed. McGraw-Hill, New York.

Schulz, C., Klein, L., Weihing, P., Lutz, T., 2016. Investigations into the Interaction of a Wind Turbine with Atmospheric Turbulence in Complex Terrain. J. Phys. Conf. Ser. 753, 032016. doi:10.1088/1742-6596/753/3/032016

Shamsoddin, S., Porté-Agel, F., 2017. Large-Eddy Simulation of Atmospheric Boundary-Layer Flow Through a Wind Farm Sited on Topography. Boundary-Layer Meteorol. 163, 1–17. doi:10.1007/s10546-016-0216-z

Shur, M., Spalart, P.R., Strelets, M., Travin, A., 1999. Detached-eddy simulation of an airfoil at high angle of attack. Eng. Turbul. Model. Exp. 4 669–678. doi:10.1016/B978-008043328-8/50064-3

Smagorinsky, J., 1963. General Circulation Experiments with The Primitive Equations. Mon. Weather Rev. 91, 99–164. doi:10.1175/1520-0493(1963)091<0099:GCEWTP>2.3.CO;2

Sørensen, J.N., Shen, W.Z., Munduate, X., 1998. Analysis of wake states by a full-field actuator disc model. Wind Energy 1, 73–88. doi:10.1002/(SICI)1099-1824(199812)1:2<73::AID-WE12>3.0.CO;2-L

Spalart, P.R., Deck, S., Shur, M.L., Squires, K.D., Strelets, M.K., Travin, A., 2006. A New Version of Detached-eddy Simulation, Resistant to Ambiguous Grid Densities. Theor. Comput. Fluid Dyn. 20, 181–195. doi:10.1007/s00162-006-0015-0

Stevens, R.J.A.M., Gayme, D.F., Meneveau, C., 2015. Coupled wake boundary layer model of wind-farms. J. Renew. Sustain. Energy 7. doi:10.1063/1.4915287

Stevens, R.J.A.M., Meneveau, C., 2017. Flow Structure and Turbulence in Wind Farms. Annu. Rev. Fluid Mech. 49, 311–339. doi:10.1146/annurev-fluid-010816-060206

Tamura, T., Cao, S., Okuno, A., 2007. LES Study of Turbulent Boundary Layer Over a Smooth and a Rough 2D Hill Model. Flow, Turbul. Combust. 79, 405–432. doi:10.1007/s10494-007-9106-2

Taylor, P.A., Teunissen, H.W., 1987. The Askervein Hill project: Overview and background data. Boundary-Layer Meteorol. 39, 15–39. doi:10.1007/BF00121863

Tsukimori, O., 2017. Japan accelerates wind power development as govt support pays off: study [WWW Document]. URL https://www.reuters.com/article/us-japan-renewables-wind/japan-accelerates-wind-power-development-as-govt-support-

pays-off-study-idUSKBN1670VP

Vermeer, L.J., Sørensen, J.N., Crespo, A., 2003. Wind turbine wake aerodynamics. Prog. Aerosp. Sci. 39, 467–510. doi:10.1016/S0376-0421(03)00078-2

Vermeulen, P.E.J., 1980. An experimental analysis of wind turbine wakes, in: Third International Symposium on Wind Energy Systems. Lyngby,Denmark, pp. 431–450.

Vollmer, L., Steinfeld, G., Heinemann, D., Kühn, M., 2016. Estimating the wake deflection downstream of a wind turbine in different atmospheric stabilities: an LES study. Wind Energ. Sci 1, 129–141. doi:10.5194/wes-1-129-2016

Wagenaar, J.W., Machielse, L.A.H., Schepers, J.G., 2012. Controlling Wind in ECN's Scaled Wind Farm.

Whalea, J., Andersonb, C.G., Bareissc, R., Wagnerc, S., 2000. An experimental and numerical study of the vortex structure in the wake of a wind turbine. J. Wind Eng. Ind. Aerodyn. 84, 1–21. doi:10.1016/S0167-6105(98)00201-3

Wikipedia, n.d. https://en.wikipedia.org/wiki/Root-mean-square_deviation [WWW Document].

Witha, B., Steinfeld, G., Heinemann, D., 2014. Advanced turbine parameterizations in offshore LES wake simulations. Researchgate.Net.

Wu, Y.-T., Porté-Agel, F., 2015. Modeling turbine wakes and power losses within a wind farm using LES: An application to the Horns Rev offshore wind farm. Renew. Energy 75, 945–955. doi:10.1016/J.RENENE.2014.06.019

Wu, Y.T., Porté-Agel, F., 2012. Atmospheric turbulence effects on wind-turbine wakes: An LES study. Energies 5, 5340–5362. doi:10.3390/en5125340

Wu, Y.T., Porté-Agel, F., 2011. Large-Eddy Simulation of Wind-Turbine Wakes: Evaluation of Turbine Parametrisations. Boundary-Layer Meteorol. 138, 345–366. doi:10.1007/s10546-010-9569-x

WWEA, 2018. WIND POWER CAPACITY REACHES 539 GW, 52,6 GW ADDED IN 2017 [WWW Document]. URL https://wwindea.org/blog/2018/02/12/2017-statistics/6/

Xian, X., Tao, W., Qingwei, S., Weimin, Z., 2002. Field And Wind-Tunnel Studies Of Aerodynamic Roughness Length. Boundary-Layer Meteorol. 104, 151–163. doi:10.1023/A:1015527725443

Xie, S.B., Archer, C., 2014. Self-similarity and turbulence characteristics of wind turbine wakes via large-eddy simulation. Wind Energy 17, 657–669. doi:10.1002/we

Yamaguchi, A., Ishihara, T., Fujino, Y., 2003. Experimental study of the wind flow in a coastal region of Japan. J. Wind Eng. Ind. Aerodyn. 91, 247–264. doi:10.1016/S0167-6105(02)00349-5

Yang, X., Howard, K.B., Guala, M., Sotiropoulos, F., 2015. Effects of a three-dimensional hill on the wake characteristics of a model wind turbine. Phys. Fluids 27. doi:10.1063/1.4907685

Yang, X., Sotiropoulos, F., 2016. Analytical model for predicting the performance of arbitrary size and layout wind farms. Wind Energy 19, 1239–1248. doi:10.1002/we.1894

Yang, X., Sotiropoulos, F., Conzemius, R.J., Wachtler, J.N., Strong, M.B., 2014. Large-eddy simulation of turbulent flow past wind turbines/farms: the Virtual Wind Simulator

(VWiS). Wind Energy 18, 2025–2045. doi:10.1002/we.1802

Yoshizawa, Y., Ishihara, T., 2015. Numerical study of wind turbine wakes, in: Proc of the 70th National Symposium on Civil Engineering, 2015.(in Japanese). pp. 1–2.